



UNIVERSITY OF NAIROBI

**SYNTHESIS OF *MESO*-TETRA (5-BROMOTHIOPHEN-2-YL)
PORPHYRINS FOR PHOTODYNAMIC WATER
DISINFECTION**

PATRICK DOMINIC KINUTHIA

Department of Chemistry


I56/11471/2018

**A Thesis Submitted in Partial Fulfilment of the Requirements for
the Award of the Degree of Master of Science in Chemistry of the
University of Nairobi.**

2023

DECLARATION

I declare that this thesis is my original work and has not been submitted elsewhere for examination. Where other people's work other than my own has been used, this has been properly acknowledged and referenced in accordance with the University of Nairobi's requirements.

Signature  Date: 16/08/2023

Patrick Dominic Kinuthia

I54/11471/2018

Department of Chemistry

Faculty of Science and Technology

University of Nairobi.

This thesis is submitted for examination with our approval as research supervisors.

Supervisor:

Signature:

Date:

Dr Solomon Derese

Department of Chemistry-UON

P.O. Box 30197-00100 Nairobi

sderese@uonbi.ac.ke



16/08/23

Dr Albert Ndakala

Department of Chemistry-UON

P.O. Box 30197-00100 Nairobi

andakala@uonbi.ac.ke



16/08/23

Dr Edith K. Amuhaya

Department of Chemistry- USIU
Africa

P.O. Box 14634-00800 Nairobi

eamuhaya@usiu.ac.ke



16/08/23

DEDICATION

I dedicate this thesis to my mother Elizabeth Kinuthia, for her firm words, whose consequence was encouragement and inspired action. My grandparents (Dominic and Lucy Kinuthia), aunts and uncles for they have been a source of strength and balanced guidance throughout this period. I further dedicate this work to my Uncle, Martin Kinuthia who encouraged me to take up this adventure in pursuit of a master's certification.

ACKNOWLEDGEMENTS

The spirit of *harambee* are the words that come to mind as a consequence of this study. It has been made possible through the work of many hands and I would like to thank them all. From the class to the lab to the home. The support I have received has been immense.

I begin by thanking my supervisors: Dr. Edith Amuhaya, Dr. Solomon Derese and Dr. Albert J Ndakala for not only giving me this opportunity but also having the faith that I could carry it out. It is through their guidance and trust that this ship has been steered to its port.

I extend a hand of gratitude to my fellow lab-mates James Oyim, Margaret Murage, Kelvin Wangai, Carolyne Bakasa and Eugene Otoo for being a bounce board for ideas and strategies for tackling new and exciting challenges as they appeared during the course of this study.

I would like to thank the Gandhi Smarak Nidhi Foundation for the sponsorship of my study at the University of Nairobi and the International Development Research Centre for funding the study.

This study was conducted at the United States International University-Africa (USIU) and the University of Nairobi, they provided a conducive learning environment, one adorned with nature that made introspection and retrospection especially easy. It was in these light moments that new dots were connected and for this I am grateful to them.

ABSTRACT

Pathogens in water continue to pose a danger to those who consume water. This is exacerbated by issues of water scarcity, antimicrobial resistance, toxic-by-products in water disinfection techniques and the cost of implementing water disinfection techniques. A remedy to these issues could be photodynamic water disinfection, a technique that utilises light to generate singlet oxygen, a cytotoxic species with no toxic by-products. In this study *meso*-tetra(5-bromothiophen-2-yl)porphyrin and its metallated analogues (zinc, indium, tin, iron, cobalt and nickel) were synthesised as its photosensitisers, characterised empirically and computationally via density functional theory. Four of the eight compounds synthesised were tested against carbapenem resistant *Escherichia coli* (*CRE.coli*) and methicillin resistant *Staphylococcus aureus* (MRSA) to determine their antimicrobial activity. The antimicrobial efficacy was conducted using broth-dilution method, which involved exposing the bacteria to varying concentrations of BTP and its metal analogues. Iron-BTP had the highest potency of the compounds tested against both bacteria. This was based on its 50% minimum inhibitory concentration (IC_{50}), where for MRSA it was $33\mu\text{M}$ and for *CRE.coli* it was $87\mu\text{M}$.

Table of Contents

| | |
|--|------|
| DECLARATION | ii |
| DEDICATION | iii |
| ACKNOWLEDGEMENTS | iv |
| ABSTRACT | v |
| List of Tables..... | x |
| List of Figures | xi |
| List of Schemes | xiii |
| List of Appendices | xiv |
| List of Acronyms and Abbreviations | xvii |
| CHAPTER 1: INTRODUCTION | 1 |
| 1.1. Background of the Study | 1 |
| 1.2. Statement of the Problem..... | 3 |
| 1.3. Objectives | 3 |
| 1.3.1. General objective | 3 |
| 1.3.2. Specific objectives..... | 3 |
| 1.4. Justification and Significance of the Study..... | 4 |
| CHAPTER 2: LITERATURE REVIEW | 5 |
| 2.1. Water and Life | 5 |
| 2.2. Water Contamination..... | 5 |
| 2.2.1. Inorganic Contaminants..... | 6 |
| 2.2.2. Radiological Contaminants..... | 6 |
| 2.2.3. Organic Contaminants | 7 |
| 2.2.4. Biological Contaminants | 8 |
| 2.3. Waterborne Diseases | 9 |
| 2.4. Water Disinfection Techniques | 9 |
| 2.5. Microbial Resistance to Disinfectants | 15 |
| 2.6. Photodynamic Approach to Water Disinfection..... | 16 |
| 2.6.1. Strong Absorbance in the Photo-aquatic Zone | 18 |
| 2.6.2. Photo-stability..... | 19 |

| | | |
|---|--|----|
| 2.6.3. | Low Fluorescence Quantum Yield | 19 |
| 2.6.4. | High Singlet Oxygen Quantum Yield | 19 |
| 2.6.5. | Solubility in Water..... | 20 |
| 2.7. | Photodynamic Inactivation of Pathogens | 20 |
| 2.8. | Porphyrins..... | 21 |
| 2.8.1. | Synthesis of Porphyrins | 22 |
| 2.8.2. | Photo-physical Properties of Porphyrins | 25 |
| 2.8.3. | Computational Chemistry in Selection of Porphyrins for Various Applications..... | 26 |
| 2.8.4. | Photodynamic Applications of Porphyrins..... | 27 |
| CHAPTER 3: MATERIALS AND METHODS | | 31 |
| 3.1. | Materials | 31 |
| 3.1.1. | General instrumentation | 31 |
| 3.1.2. | Reagents | 31 |
| 3.2. | Methods | 31 |
| 3.2.1. | Synthesis Procedures..... | 32 |
| 3.2.1.1. | Synthesis of <i>Meso</i> -tetra(5-bromothiophen-2-yl)porphyrin..... | 32 |
| 3.2.1.2. | Synthesis of <i>Meso</i> -tetra(5-bromothiophen-2-yl)porphyrinato Zinc(II) | 32 |
| 3.2.1.3. | Synthesis of <i>Meso</i> -tetra(5-bromothiophen-2-yl)porphyrinato Indium(III)chloride..... | 33 |
| 3.2.1.4. | Synthesis of <i>Meso</i> -tetra(5-bromothiophen-2-yl) porphyrinato Tin(IV)hydroxide | 33 |
| 3.2.1.5. | Synthesis of <i>Meso</i> -tetra(5-bromothiophen-2-yl)porphyrinato Tin(IV)dioxypyridine | 34 |
| 3.2.1.6. | Synthesis of <i>Meso</i> -tetra(5-bromothiophen-2-yl)porphyrinato Iron(III)chloride | 34 |
| 3.2.1.7. | Synthesis of <i>Meso</i> -tetra(5-bromothiophen-2-yl))porphyrinato Cobalt (II).... | 34 |
| 3.2.1.8. | Synthesis of <i>Meso</i> -tetra(5-bromothiophen-2-yl))porphyrinato Nickel (II).... | 35 |
| 3.2.2. | Photo-physical Studies | 36 |
| 3.2.2.1. | UV-Vis spectroscopy | 36 |
| 3.2.2.2. | Fluorescence and fluorescence quantum yield | 36 |
| 3.2.3. | Theoretical Studies | 37 |
| 3.2.4. | Antimicrobial Studies..... | 37 |
| CHAPTER 4: RESULTS AND DISCUSSION | | 39 |

| | |
|--|----|
| 4.1. Outline of the Study..... | 39 |
| 4.2. Synthesis and Characterisation of the Porphyrins | 39 |
| 4.2.1. Synthesis of <i>Meso</i> -tetra(5-bromothiophen-2-yl)porphyrin | 39 |
| 4.2.2. Synthesis of <i>Meso</i> -tetra(5-bromothiophen-2-yl) porphyrinato Zinc (II)..... | 41 |
| 4.2.3. Synthesis of <i>Meso</i> -tetra(5-bromothiophen-2-yl)porphyrinato Indium (III) chloride | 42 |
| 4.2.4. Synthesis of <i>Meso</i> -tetra(5-bromothiophen-2-yl)porphyrinato Tin(IV)hydroxide | 42 |
| 4.2.5. Synthesis of <i>Meso</i> -tetra(5-bromothiophen-2-yl)porphyrinato Tin(IV)dioxypyridine | 46 |
| 4.2.6. Synthesis of <i>Meso</i> -tetra(5-bromothiophen-2-yl)porphyrinato Iron(III)chloride... | 47 |
| 4.2.7. Synthesis of <i>Meso</i> -tetra(5-bromothiophen-2-yl)porphyrinato Cobalt(II) | 48 |
| 4.2.8. Synthesis of <i>Meso</i> -tetra(5-bromothiophen-2-yl)porphyrinato Nickel (II) | 49 |
| 4.3. Photo-physical Studies | 50 |
| 4.3.1. UV-Vis Studies | 50 |
| 4.3.1.1. Soret bands..... | 51 |
| 4.3.1.2. Q bands | 56 |
| 4.3.1.3. Molar Absorption Coefficient..... | 58 |
| 4.3.2. Fluorescence Spectroscopy | 61 |
| 4.3.2.1. Fluorescence quantum yield | 62 |
| 4.3.2.2. Stoke's shift | 64 |
| 4.4. Theoretical Studies | 66 |
| 4.4.1. Optimised Geometry | 67 |
| 4.4.1.1. Distortion of Geometry | 68 |
| 4.4.1.2. Frontier Orbitals..... | 71 |
| 4.4.2. Time Dependent –Density Functional Theory Studies | 74 |
| 4.5. Antimicrobial Studies | 77 |
| 4.5.1. Methicillin Resistant <i>Staphylococcus aureus</i> | 78 |
| 4.5.2. Carbapenem Resistant <i>Escherichia coli</i> | 81 |
| CHAPTER 5: CONCLUSION AND RECOMMENDATIONS | 86 |
| 5.1. Conclusion | 86 |

| | |
|---------------------------|----|
| 5.2. Recommendations..... | 86 |
| REFERENCES..... | 88 |
| APPENDICES..... | 98 |

LIST OF TABLES

| | |
|---|----|
| Table 1: Disinfection techniques, advantages and disadvantages | 13 |
| Table 2: Dihedral angles showing distortion in synthesised porphyrins..... | 69 |
| Table 3: Mulliken charges of transition elements | 74 |
| Table 4: Computed photo-physical properties of <i>meso</i> -tetra(5-bromothiophen-2-yl)porphyrin | 76 |
| Table 5: Significance tests for light against dark conditions- Methicillin resistant <i>Staphylococcus aureus</i> | 79 |
| Table 6: Methicillin resistant <i>Staphylococcus aureus</i> 's 50% Minimum inhibitory concentration | 80 |
| Table 7: Significance tests for light against dark conditions- Carbapenem resistant <i>Escherichia coli</i> | 82 |
| Table 8: Carbapenem resistant <i>Escherichia coli</i> 's 50% Minimum inhibitory concentration | 84 |

LIST OF FIGURES

| | |
|---|----|
| Figure 1: Predicted and current mortalities from various causes | 3 |
| Figure 2:Ozone molecule | 11 |
| Figure 3:Jablonski diagram | 17 |
| Figure 4: Water's UV-Vis spectra | 18 |
| Figure 5: General aromatic porphyrin structure with positions' labels | 21 |
| Figure 6: Generalised UV-Vis spectra of a porphyrin molecule..... | 25 |
| Figure 7:Tetra(<i>N</i> -methylpyridyl)porphine | 28 |
| Figure 8: Schematic of a metal organic framework | 29 |
| Figure 9: 2D 4,4',4'',4'''-(porphyrin-5,10,15,20-tetrayl)tetrabenzoic acid Metal Organic Framework | 29 |
| Figure 10: Over-laid UV-Vis spectra of <i>meso</i> -tetra(5-bromothiophen-2-yl)porphyrin and its metallated analogues | 51 |
| Figure 11: Overlaid Soret bands of <i>meso</i> -tetra(5-bromothiophen-2-yl)porphyrin and its metallated analogues | 52 |
| Figure 12: BTP Soret band shifts amongst <i>meso</i> -tetra(5-bromothiophen-2-yl)porphyrin and its metallated analogues | 53 |
| Figure 13: Gouterman's 4 orbital model | 54 |
| Figure 14: Q-Bands of <i>meso</i> -tetra(5-bromothiophen-2-yl)porphyrin and its metallated analogues | 57 |
| Figure 15: Overlaid UV-Vis spectra (Q bands) of <i>meso</i> -tetra(5-bromothiophen-2-yl)porphyrin and its metallated analogues..... | 58 |
| Figure 16: Molar absorption coefficient..... | 59 |
| Figure 17: Computed oscillator strength and empirical ϵ | 60 |
| Figure 18: Normalised fluorescence spectra of <i>meso</i> -tetra(5-bromothiophen-2-yl)porphyrin and its metallated analogues | 62 |
| Figure 19: Fluorescence quantum yield of <i>meso</i> -tetra(5-bromothiophen-2-yl)porphyrin and its metallated analogues | 63 |
| Figure 20: Illustration of El-Sayeed's selection rule | 64 |
| Figure 21: Stoke's shift..... | 65 |
| Figure 22: Comparison of computed and empirical UV-Vis spectra..... | 66 |
| Figure 23: <i>Meso</i> -tetra(5-bromothiophen-2-yl)porphyrinato Zinc (II) showing atom labels referenced in dihedral angle table | 67 |
| Figure 24: Gouterman's four molecular orbitals (CAM_Vacuum) for <i>meso</i> -tetra(5-bromothiophen-2-yl)porphyrin and its metal analogues | 72 |

| | |
|--|----|
| Figure 25: Computed oscillator strength and empirical ϵ | 75 |
| Figure 26: Antimicrobial activity of <i>meso-tetra(5-bromothiophen-2-yl)porphyrin (BTP)</i> and metal analogues against Methicillin Resistant <i>Staphylococcus aureus</i> | 78 |
| Figure 27:Antimicrobial activity against Methicillin Resistant <i>Staphylococcus aureus</i> | 80 |
| Figure 28: Antimicrobial activity of <i>meso-tetra(5-bromothiophen-2-yl)porphyrin</i> and metallated analogues against Carbapenem Resistant <i>Escherichia coli</i> | 81 |
| Figure 29:Antimicrobial activity against Carbapenem Resistant <i>Escherichia coli</i> | 84 |

LIST OF SCHEMES

| | |
|---|----|
| Scheme 1: Rothmund synthetic pathway | 22 |
| Scheme 2: Adler-Longo synthetic pathway | 23 |
| Scheme 3: Lindsey synthetic pathway | 23 |
| Scheme 4: Mixed-solvent system (Adler Longo) pathway | 24 |
| Scheme 5: Synthesis of <i>meso</i> -tetra(5-bromothiophen-2-yl)porphyrin..... | 39 |
| Scheme 6: Fragmentation pattern of <i>meso</i> -tetra(5-bromothiophen-2-yl)porphyrin in a mass spectrometer | 40 |
| Scheme 7: Synthesis of <i>meso</i> -tetra(5-bromothiophen-2-yl)porphyrinato Zinc (II) | 41 |
| Scheme 8: Synthesis of <i>meso</i> -tetra(5-bromothiophen-2-yl)porphyrinato Indium (III) chloride..... | 42 |
| Scheme 9: Synthesis of <i>meso</i> -tetra(5-bromothiophen-2-yl)porphyrinato Tin(IV)hydroxide | 43 |
| Scheme 10: Synthesis of <i>meso</i> -tetra(5-bromothiophen-2-yl)porphyrinato Tin(IV)dioxypyridine | 46 |
| Scheme 11: Synthesis of <i>meso</i> -tetra(5-bromothiophen-2-yl)porphyrinato Iron(III)chloride | 47 |
| Scheme 12: Synthesis of <i>meso</i> -tetra(5-bromothiophen-2-yl)porphyrinato Cobalt(II) | 48 |
| Scheme 13: Synthesis of <i>meso</i> -tetra(5-bromothiophen-2-yl)porphyrinato Nickel (II) | 49 |

LIST OF APPENDICES

| | |
|---|-----|
| Appendix 1: Mass Spectra..... | 98 |
| Appendix 1. 1 Mass Spectra of <i>Meso</i> -tetra(5-bromothiophen-2-yl)porphyrin | 98 |
| Appendix 1. 2: Mass Spectra of <i>Meso</i> -tetra(5-bromothiophen-2-yl)porphyrinato Zinc (II) | 99 |
| Appendix 1. 3: Mass Spectra of <i>Meso</i> -tetra(5-bromothiophen-2-yl)porphyrinato Indium (III) chloride | 100 |
| Appendix 1.4: Mass Spectra of <i>Meso</i> -tetra(5-bromothiophen-2-yl)porphyrinato Tin(IV)hydroxide | 101 |
| Appendix 1. 5: Mass Spectra of <i>Meso</i> -tetra(5-bromothiophen-2-yl)porphyrinato Tin(IV)dioxypyridine | 101 |
| Appendix 1. 6: Mass Spectra of <i>Meso</i> -tetra(5-bromothiophen-2-yl)porphyrinato Iron(III)chloride | 102 |
| Appendix 1. 7: Mass Spectra of <i>Meso</i> -tetra(5-bromothiophen-2-yl)porphyrinato Cobalt(II)..... | 103 |
| Appendix 1. 8: Mass Spectra of <i>Meso</i> -tetra(5-bromothiophen-2-yl)porphyrinato Nickel (II)..... | 104 |
| Appendix 2: ¹ H NMR..... | 105 |
| Appendix 2. 1: ¹ H NMR of <i>Meso</i> -tetra(5-bromothiophen-2-yl)porphyrin | 105 |
| Appendix 2. 2: ¹ H NMR of <i>Meso</i> -tetra(5-bromothiophen-2-yl)porphyrinato Zinc (II) | 106 |
| Appendix 2. 3: ¹ H NMR of <i>Meso</i> -tetra(5-bromothiophen-2-yl)porphyrinato Indium (III) chloride..... | 107 |
| Appendix 2. 4: ¹ H NMR of <i>Meso</i> -tetra(5-bromothiophen-2-yl)porphyrinato Tin(IV)hydroxide | 107 |
| Appendix 3: Empirical Photo-physical Properties (UV-Vis, Molar Absorption Coefficient and Fluorescence) | 109 |
| Appendix 3. 1: Empirical Photophysical Properties of <i>Meso</i> -tetra(5-bromothiophen-2- yl)porphyrin..... | 109 |
| Appendix 3. 2: Empirical Photophysical Properties of <i>Meso</i> -tetra(5-bromothiophen-2- yl)porphyrinato Zinc (II) | 110 |
| Appendix 3. 3Empirical Photophysical Properties of <i>Meso</i> -tetra(5-bromothiophen-2- yl)porphyrinato Indium (III) chloride | 111 |

| | |
|--|-----|
| Appendix 3. 4: Empirical Photophysical Properties of <i>Meso</i> -tetra(5-bromothiophen-2-yl)porphyrinato Tin(IV)hydroxide | 112 |
| Appendix 3. 5: Empirical Photophysical Properties of <i>Meso</i> -tetra(5-bromothiophen-2-yl)porphyrinato Tin(IV)dioxypyridine | 113 |
| Appendix 3. 6: Empirical Photophysical Properties of <i>Meso</i> -tetra(5-bromothiophen-2-yl)porphyrinato Iron(III)chloride | 114 |
| Appendix 3. 7: Empirical Photophysical Properties of <i>Meso</i> -tetra(5-bromothiophen-2-yl)porphyrinato Cobalt(II)..... | 115 |
| Appendix 3. 8: Empirical Photophysical Properties of <i>Meso</i> -tetra(5-bromothiophen-2-yl)porphyrinato Nickel (II)..... | 116 |
| | |
| Appendix 4: Infrared Spectra | 117 |
| Appendix 4. 1: FTIR of <i>Meso</i> -tetra(5-bromothiophen-2-yl)porphyrin and its Metal Derivatives | 117 |
| Appendix 4. 2: FTIR Spectra of <i>Meso</i> -tetra(5-bromothiophen-2-yl)porphyrin and its Metal Derivatives (3000 to 4000 cm ⁻¹) | 118 |
| | |
| Appendix 5: Optimised Structures | 119 |
| Appendix 5. 1: Optimised Structure of <i>Meso</i> -tetra(5-bromothiophen-2-yl)porphyrin . | 119 |
| Appendix 5. 2: Optimised Structure of <i>Meso</i> -tetra(5-bromothiophen-2-yl)porphyrinato Zinc (II) | 119 |
| Appendix 5. 3: Optimised Structure of <i>Meso</i> -tetra(5-bromothiophen-2-yl)porphyrinato Indium (III) chloride..... | 120 |
| Appendix 5. 4: Optimised Structure of <i>Meso</i> -tetra(5-bromothiophen-2-yl)porphyrinato Tin(IV)hydroxide | 120 |
| Appendix 5. 5: Optimised Structure of <i>Meso</i> -tetra(5-bromothiophen-2-yl)porphyrinato Tin(IV)dioxypyridine | 121 |
| Appendix 5. 6: Optimised Structure of <i>Meso</i> -tetra(5-bromothiophen-2-yl)porphyrinato Iron(III)chloride | 122 |
| Appendix 5. 7: Optimised Structure of <i>Meso</i> -tetra(5-bromothiophen-2-yl)porphyrinato Cobalt(II)..... | 122 |
| Appendix 5. 8: Optimised Structure of <i>Meso</i> -tetra(5-bromothiophen-2-yl)porphyrinato Nickel (II)..... | 123 |

| | |
|---|-----|
| Appendix 6: Computed HOMO_LUMO Gap..... | 124 |
| Appendix 6. 1: Gouterman's Four Orbitals' Energies | 124 |
| Appendix 6. 2: Variations in Orbitals' Averaged Energies | 124 |
| | |
| Appendix 7: Computed Photophysical Properties of <i>Meso</i> -tetra(5-bromothiophen-2-yl)porphyrin and Its Metal Analogues..... | 125 |
| Appendix 7. 1: Computed photo-physical properties of <i>meso</i> -tetra(5-bromothiophen-2-yl)porphyrin..... | 125 |
| Appendix 7. 2: Computed photo-physical properties of <i>meso</i> -tetra(5-bromothiophen-2-yl)porphyrinato Zinc(II) | 126 |
| Appendix 7. 3: Computed photo-physical properties of <i>meso</i> -tetra(5-bromothiophen-2-yl)porphyrinato Indium (III) chloride | 127 |
| Appendix 7. 4: Computed photo-physical properties of <i>meso</i> -tetra(5-bromothiophen-2-yl)porphyrinato Tin(IV)hydroxide | 128 |
| Appendix 7. 5: Computed photo-physical properties of <i>meso</i> -tetra(5-bromothiophen-2-yl)porphyrinato Tin(IV)dioxypyridine | 129 |
| Appendix 7. 6: Computed photo-physical properties of <i>meso</i> -tetra(5-bromothiophen-2-yl)porphyrinato Iron(III)chloride | 130 |
| Appendix 7. 7: Computed photo-physical properties of <i>meso</i> -tetra(5-bromothiophen-2-yl)porphyrinato Cobalt(II)..... | 131 |
| Appendix 7. 8: Computed photo-physical properties of <i>meso</i> -tetra(5-bromothiophen-2-yl)porphyrinato Nickel (II)..... | 132 |
| | |
| Appendix 8: Antimicrobial Activity | 133 |
| Appendix 8. 1: Methicillin Resistant <i>Staphylococcus aureus</i> survival rate | 133 |
| Appendix 8. 2: Carbapenem Resistant <i>Escherichia coli</i> survival rate..... | 133 |

LIST OF ACRONYMS AND ABBREVIATIONS

| Acronym | Full name |
|----------------------------------|--|
| •OH | Hydroxyl radical |
| ¹ O ₂ | Singlet oxygen |
| 2D | Two-dimensional |
| 2D-Tcpp | 4,4',4'',4'''-(Porphyrin-5,10,15,20-tetrayl)tetrabenzoic acid |
| 3D | Three-dimensional |
| ³ O ₂ | Triplet state oxygen |
| Abs | Absorbance |
| B3LYP | Beckes's 3 parameter Lee, Yand and Parr exchange correlation functional |
| BF ₃ OEt ₂ | Boron trifluoride dietherate |
| BTP | <i>Meso</i> -tetra(5-bromothiophen-2-yl)porphyrin |
| <i>CRE.coli</i> | Carbapenem resistant <i>Escherichia coli</i> |
| CAM-B3LYP | Coulomb attenuating method-B3LYP functional |
| CDCl ₃ | Deuterated chloroform |
| ClO ₂ | Chlorine dioxide |
| DCM | Dichloromethane |
| DDQ | 2,3-Dichloro-5,6-dicyanobenzoquinone |
| DFT | Density Functional Theory |
| DMSO | Dimethyl sulphoxide |
| <i>E.coli</i> | <i>Escherichia coli</i> |
| f | Oscillator strength |
| FTIR | Fourier Transform Infrared Radiation |
| HOCl | Hypochlorous acid |
| IBU | Inorganic building unit |
| IC ₅₀ | 50% Minimum Inhibitory Concentration |
| ISC | Intersystem crossing |
| MALDI-TOF | Matrix assisted laser desorption/ionization–time of flight mass spectrometer |
| MCL | Minimum containment limit |
| MeOH | Methanol |

| | |
|---------------------|--|
| MM | Molecular Mechanics |
| MOF | Metal Organic Framework |
| MRSA | Methicillin resistant <i>Staphylococcus aureus</i> |
| NMR | Nuclear Magnetic Resonance |
| O ₃ | Ozone |
| OBU | Organic building unit |
| PAZ | Photo-aquatic zone |
| PBS | Phosphate buffer solution |
| PCM | Polarizable continuum model |
| PDT | Photodynamic therapy |
| PFA _s | Per- or poly-fluoroalkyl substances |
| PNEC | Predicted no effect concentration |
| PS | Photosensitiser |
| r ² | Coefficient of determination |
| ROS | Reactive oxygen species |
| SDD | Stuttgart Dresden |
| SODIS | Solar water disinfection |
| TD-DFT | Time-dependent density functional theory |
| TMPyP | Tetra- <i>meso</i> (<i>N</i> -methylpyridyl) porphine |
| TPPH | Tetraphenylporphyrin |
| UFF | Universal Force Field |
| Ultraviolet-visible | UV-Vis |
| WHO | World Health Organisation |
| xs | Excess |
| ε | Molar absorptivity coefficient (L/Mol/cm) |

CHAPTER 1: INTRODUCTION

1.1. Background of the Study

The civilisation pillar that has contributed the most to humanity's progress hinges on agricultural and industrial development. This has resulted in the availability of food and the development of other innovations not directly involved in food production. The culmination of these developments has been the development of cities or urban centres. Such centres are associated with large populations that consume large quantities of clean water and food and produce significant volumes of waste. Consequently, cities need a source of water and a way to manage their waste to avoid the fate of London in the 1800s, where cholera ravaged through the population until Dr John Snow identified the root cause of the problem as cholera contaminated drinking water. The city of London managed to control the spread of cholera by treating its water by chlorination (Gray, 2013).

As industrialisation progresses globally, rural-urban migration is expected to increase. This coupled with increasing waste production from industries allied to processing metals, dyes and pharmaceuticals, will increase the need for purifying water in the 21st century. To put this in perspective, in the 1800s when cholera struck London, the population then was approximately 650,000 people. Nowadays, cities host millions of people, with Tokyo in Japan having the largest population of 37 million people. It is projected that cities will over the next 20 years play host to approximately 68% of the world's human population (United Nations, 2019). This renewed trend has led to a multitude of changes in cities including construction of sky-scraper like residential units with hundreds of units per building, extension of sewerage networks, rain-water harvesting in these buildings and remediation of water. While these solutions to increased populations have borne fruit with more housing available to many, they have not been without their challenges. The first of which has been water contaminated with bacteria such as *legionella* bacteria which causes pneumonia (Cullom *et al.*, 2020; Malinowski *et al.*, 2022).

In 2018, The United Nations reported that up to 47% of the global population lived in areas that were water stressed and projected that this will worsen by 2050. They also projected a global population growth of 9 to 10.2 billion people, 6 billion of whom will be living in conditions of water scarcity (Boretti and Rosa, 2019). This calls for effective water decontamination of existing water resources to make them available for this increasing population. The current strategies for water decontamination can have shortcomings such as odour problems in the case of chlorine disinfection, high costs as in the case of ozonation and

high energy and time requirements should boiling be the method of choice. There is therefore a compelling need to identify safer, less energy-intensive and cheaper water decontamination strategies.

This study focused on water disinfection through photodynamic effect by focusing on the photosensitiser (PS) element of photodynamic effect. Photodynamic effect is a tripartite system involving light, oxygen and a PS. The PS absorbs light and transfers the light energy to ground-state oxygen (also known as triplet-state oxygen ($^3\text{O}_2$)) and this in turn is transformed to cytotoxic singlet oxygen ($^1\text{O}_2$). Cationic photosensitisers have been shown to be effective against both gram-positive and gram-negative bacteria, this is on account of the negative charges on the membranes of both types of bacteria. This also explains why more cationic photosensitisers have been tested for their antimicrobial capacity in water compared to those of neutral photosensitisers (Thandu *et al.*, 2015).

However, a study on a neutral photosensitiser has shown that they too have the capacity to act on both types of bacteria (Xu *et al.*, 2016). Thus in order to increase the knowledge base of effective neutral photosensitisers in photodynamic water disinfection, this study investigated the potential of *meso*-tetra(5-bromothiophen-2-yl)porphyrin and its metal analogues (Fe, Co, Ni, Zn, In and Sn) as photosensitisers in photodynamic disinfection of water contaminated with gram-positive and gram-negative bacteria.

1.2. Statement of the Problem

Pathogens have continued to evolve resistance mechanisms against disinfectants and are also able to transfer this resistance to other pathogens via lateral gene transfer or through cooperation as in biofilms (Radhouani *et al.*, 2014). This thus necessitates the use of higher concentrations of disinfectants in order to kill them. However, this leads to the production of more toxic by-products (as in chlorine) or increase in instances of mutation in pathogens. This problem is not only prevalent in water disinfection but also in the treatment of bacterial infections. This means that once a pathogen by-passes water treatment and makes its way to a host, it is no longer a guarantee that it can be treated with available antibiotics. This danger is made clear by the 1.27million deaths from antimicrobial resistant bacterial infections in 2019, as shown in [Figure 1](#) (Murray *et al.*, 2022). Thus a technique that utilises non-toxic components, with no toxic by-products and does not confer resistance upon future generations of pathogens would be of great utility to the human race in water disinfection.

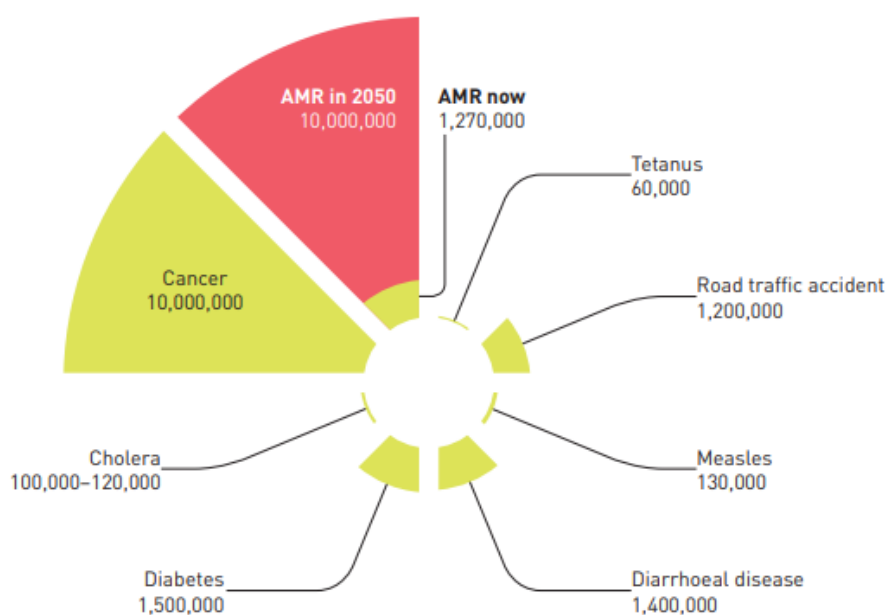


Figure 1: Predicted and current mortalities from various causes (United Nations Environment Programme, 2022)

1.3. Objectives

1.3.1. General objective

The general objective of the study was to develop a porphyrin with potential application in water disinfection.

1.3.2. Specific objectives

The specific objectives of this study were:

- i. To synthesize and characterize *meso*-tetra(5-bromothiophen-2-yl) porphyrins
- ii. To determine the photo-physical properties of the *meso*-tetra(5-bromothiophen-2-yl) porphyrins synthesised.
- iii. To simulate the photo-physical properties of *meso*-tetra(5-bromothiophen-2-yl) porphyrin and its metal analogues computationally.
- iv. To establish the antimicrobial activity of *meso*-tetra(5-bromothiophen-2-yl) porphyrins.

1.4. Justification and Significance of the Study

Although cationic photosensitizer (PS) molecules are considered to be more effective against pathogens, recent studies have shown that neutral molecules could also have the same potency (Khisa, 2020; Xu *et al.*, 2016). This means that neutral molecules could generate the same potency if not better than cationic ones under appropriate conditions. Determining these conditions could aid in improving not only the potency of these molecules but it could also increase the number of PS molecules that can be utilised. Furthermore, photodynamic effect utilises a common mechanism of action as the most potent water disinfectant, ozone (Magaraggia *et al.*, 2011). This can only add to its merit as an alternative water disinfectant.

CHAPTER 2: LITERATURE REVIEW

2.1. Water and Life

Water is ubiquitous (it covers 70% of the earth's land mass) and is fundamental to the survival of most, if not all, biotic species on the planet. It is a polar molecule commonly used as a solvent for polar substances. This is what makes it an essential component to the most diverse ecosystems in the world. In places such as the Atacama Desert in Chile (driest place on earth) (Collado *et al.*, 2013), relatively few species can be found. In the amazon and Congo basins, where water is plentiful, the number of different species ranging from flora to fauna is significantly greater. Although, this cannot be attributed to the quantity of water alone, it is undeniable that water plays a large part in it. This can be observed through the interaction with water and proteins, such as enzymes. It is partly due to their interaction that these essential proteins are able to fold in the right way and thus able to perform their functions, which include enabling metabolism.

Indeed, water is such an integral part of living beings that it constitutes majority of the body of these living beings. For instance, in humans, water constitutes 70% of the human body and without it after seven days a human will more often than not perish. Thus access to safe drinking water is considered a human right. One albeit that is becoming increasingly difficult to realise.

While nature utilised water to build a planet inhabited by numerous species, humanity has used it to build civilisations and to become one of the most successful species on the planet numbering approximately 8 billion individuals in 2022 (United Nations Department for Economic and Social Affairs, 2023). With this success, however, new challenges have arisen. In 2018, approximately 47% of the population of the world were faced with conditions of water scarcity at least once a month (Boretti and Rosa, 2019) This was further exacerbated by contaminants in water which make traditional sources of water such as lakes and rivers unsafe for direct consumption. There is a need for increased access to safe water to promote human health and development.

2.2. Water Contamination

Water contamination is due to the presence of elevated concentrations of harmful substances in the environment above the background level for the area or at unsafe levels for an organism's health in the environment (World Health Organization, 2018). These contaminants can be classified into inorganic contaminants, radiological contaminants, organic contaminants and biological contaminants (Sharma and Bhattacharya, 2017).

2.2.1. Inorganic Contaminants

Inorganic contaminants include heavy metals and metalloids such as chromium, lead and barium, whose atomic mass exceed 40.004 and have a specific gravity equal to or greater than 5g/cm^3 (Azeh Engwa *et al.*, 2019). The danger inorganic contaminants pose to living organisms is through: direct reaction, assimilation and reactive oxygen species (ROS) (Munzeiwa *et al.*, 2022).

Direct reaction occurs where inorganic contaminants can react with components or constituents in a living organism leading to detrimental consequences such as denatured enzymes. This is especially true in the case of proteins that have thiol groups. Assimilation takes place when an essential metal in the normal operation of an organism is replaced with a similar metal albeit without any capacity of the required metal. An example is given when a phosphate, which is necessary for energy production in cells through adenosine triphosphate, is replaced with arsenate salts. Arsenate is larger and its bonds to adenosine cannot be broken with same mechanism to release energy in the same way as phosphates. Reactive oxygen species include: hydroxyl radicals ($\bullet\text{OH}$) and superoxide anions (O_2^-), whose formation is through Fenton reaction mediated by heavy metals such as vanadium and iron. They are indiscriminate oxidative agents that react with cell components including phospholipids, proteins and DNA leading to damage and significant alterations to these components (Azeh Engwa *et al.*, 2019; Munzeiwa *et al.*, 2022).

Through the aforementioned interactions with living cells, inorganic contaminants can lead to cancers, neurotoxicity and death. The sources of inorganic contaminants are primarily from industrial activities such as mining and manufacturing where these metals are produced either as by-products of raw-materials or as industrial waste (Azeh Engwa *et al.*, 2019). In quantitative terms the safe limit for it is called the minimum containment limit (MCL). For lead the MCL is 0.015mg/L and for barium, it is 2mg/L (Sharma and Bhattacharya, 2017). Inorganic contaminants can be removed from water through filtration and biological remediation either by plants or by micro-organisms (Ceci *et al.*, 2019; Cevallos-Mendoza *et al.*, 2022; Munzeiwa *et al.*, 2022).

2.2.2. Radiological Contaminants

Radiological contaminants are those that release high energy particles or toxic radiation. They include compounds such as uranium 227, thorium and other radioactive elements (safe limits of radioactive elements are specified as MCL, where uranium has an MCL of $30\mu\text{g/L}$ (Sharma

and Bhattacharya, 2017). Contamination above the threshold level by radioactive elements leads to life altering diseases such as thyroid cancer and even death (Munzeiwa *et al.*, 2022; Steinhauser *et al.*, 2014). It is for this reason where significant contamination has occurred, drastic measures are usually taken to control further exposure. For example, in Chernobyl, where a nuclear meltdown occurred (in 1986), the surrounding cities (Pripyat and Chernobyl) were completely evacuated due to radioactive material that had been scattered by the explosion from the nuclear power plant (Kortov and Ustyantsev, 2013).

2.2.3. Organic Contaminants

Organic contaminants are carbon-based compounds that may contain nitrogen, sulphur, phosphorous, halogens and oxygen (Agardy and Nemerow, 2005; Sarma and Prasad, 2016). They include organic dyes, fertilizers, explosives, pharmaceuticals, pesticides, petroleum products and coatings. Organic contaminants pose a danger to life as ecological disruptors as well as by altering or interfering with normal operations of an organism. Ecological disruptors here mean that they alter the balance that exists in an eco-system. For example, nitrogen fertilisers end-up in rivers and lakes as run-off from farms. Consequently, this enhances the growth of algae, which in turn reduces the amount of oxygen available in lakes (Ruziwa *et al.*, 2022).

Another example of organic pollutants is pharmaceuticals, which are especially prevalent next to hospitals where a number of patients are being treated for a variety of infections. Pharmaceuticals are classified as emerging organic contaminants (EOC) because the recognition of the great risk they pose was recently discovered or has not been sufficiently documented to guide formulation of appropriate policies to contain them (Ruziwa *et al.*, 2022; Vázquez-Tapia *et al.*, 2022). The release of pharmaceuticals such as antibiotics through excessive use have led to an increase in instances of antimicrobial resistance (AMR). This means that infections that were once easily treated have now turned deadly. In 2019, AMR was responsible for the death of 1.27 million people and this is projected to reach 10 million by 2050 (Murray *et al.*, 2022).

Organic contaminants interfere with the normal operations of a living organism such as growth, respiration and reproduction since they can be carcinogenic, endocrine disruptors or simply by bio-accumulating in the body. Coatings made with per or poly-fluoroalkyl compounds (PFAs), also known as forever chemicals because they can stay in the environment for many years without being degraded. They were used in making anti-stick crockery and manufacturing fire-

resistant materials and are carcinogenic. This means that they interfere with the genes of individuals (Boyd *et al.*, 2022). Endocrine disruptors interfere with hormone production in the human body as well as animals. These contaminants include steroids, synthetic steroids and other compounds such as PFAs (Vázquez-Tapia *et al.*, 2022). Hormones are especially important to living organisms as they are the avenue through which they regulate other functions from digestion to mobility. Some organic pollutants interfere with the endocrine system by: possessing structures similar to hormones and thus take their place in the normal functions of the body or by damaging receptors through oxidative stress. This leads to disruptions in growth, reproduction and respiration (Boyd *et al.*, 2022; Ruziwa *et al.*, 2022).

Organic contaminants can be removed from water through filtration, such as in ultra-filtration and reverse osmosis, sorption, volatilisation, photolysis and biological remediation (Ruziwa *et al.*, 2022). Biological remediation can include rhizofiltration, where some plant species such as *Cyperus rotundus* have been shown to absorb these contaminants through their roots and transform them into less toxic metabolites that can be broken down once they are released back into the soil via their roots (Ruziwa *et al.*, 2022; Sarma and Prasad, 2016).

2.2.4. Biological Contaminants

Biological contaminants include pathogenic bacteria, protozoa, viruses and algae (Sharma and Bhattacharya, 2017). Pathogens become dangerous to humans and animals when they are in contact with a hosts' cells (Goncharuk *et al.*, 2019) or through the by-products they produce, for example blue-green algae. These algae produce hepatotoxins, which are toxic to the liver and neurotoxins, which are toxic to the brain (Sharma and Bhattacharya, 2017). Contact can be through ingestion of water, dermal contact or inhalation. The sources of pathogens in water can be classified as: environmental sources, when they occur in the natural environment, human sources, when they are found in humans and animal sources, when they are found in animals. These sources act as reservoirs for the various pathogens allowing them to thrive and multiply for example in: environmental sources, there is the bacterium *Legionella*, in humans there is the virus hepatitis A and in animals, there is the bacterium *Shigella* (World Health Organization, 2016).

In general, the greatest microbial risks come from ingesting water contaminated with animal or human faecal matter (this could be from wastewater discharges) (Cabral, 2010). Pathogens from animal and human systems eventually inactivate after they leave their host systems. However, factors such as presence of relatively high amounts of biodegradable carbon in water (provides substrates for the formation of biofilms, which act as a barrier from hostile external

conditions), turbidity (prevents penetration of UV rays that would inactivate bacteria) and low ambient temperatures (low temperatures inactive microbes and this allows them to stay alive without expending too much energy) may enable pathogens to persist (Sharma and Bhattacharya, 2017). 1.8 billion people (26% of the world's population) use a drinking water source that is contaminated with faecal matter (World Health Organization, 2020). As the population rises, the World Health Organisation (WHO) predicts that by 2025 50% of the world's population will be living in water-stressed areas which translates to potentially a larger population consuming biologically contaminated water (Wang *et al.*, 2021; World Health Organization, 2020).

2.3. Waterborne Diseases

Waterborne diseases refer to those infections and diseases that occur because of interaction between humans and waterborne pathogens. These include diseases such as cholera (bacterial: *Vibrio cholerae*), typhoid (bacterial: *Salmonella typhi*) and hepatitis A (virus: *Hepatovirus A*) (Cabral, 2010; Magana-Arachchi and Wanigatunge, 2020; Sharma and Bhattacharya, 2017). The symptoms of waterborne diseases are varied: from paralysis (polio) to high fevers (typhoid and cholera) but most are characterised by diarrhoea (Galal-Gorchev, 1996). Waterborne diarrhoeal diseases, which include: cholera, shigellosis and gastroenteritis were responsible for 896,000 deaths in 2016 with majority occurring in children under the age of 5 (Magana-Arachchi and Wanigatunge, 2020). It is estimated that there are between 1.3 to 4 million cases of cholera annually leading to an estimated 21,000 to 143,000 deaths. Cholera can lead to death within hours if left untreated (Ali *et al.*, 2015).

Waterborne diseases also have an economic impact on societies, either by resultant inactivity of working members of the society or reduction in trade in the society. An illustration is given by Peru, where in 1991 a cholera outbreak cost the country's economy 1 billion US dollars (Galal-Gorchev, 1996), this represented approximately 2.78% of its gross-domestic product (World Bank, 2022). These have largely been addressed through the introduction of centralised water disinfection treatment plants.

2.4. Water Disinfection Techniques

Water disinfection refers to the effective removal or reduction of pathogens' populations to levels that are unlikely to cause detrimental effects to the host consuming it. *Escherichia coli* (*E.coli*) is usually used as an indicator pathogen for pathogen population levels (Percival, 2014).

The goal of disinfection techniques for the scientists that design and develop them is therefore to reduce pathogen loads to attain these low levels. This has been possible with techniques such as chlorination, ozonation, solar water disinfection (SODIS) and thermal disinfection techniques, with chlorination as the most popular of these methods. Chlorination and ozonation are chemical methods of disinfection that were necessitated due to the inherent nature of pollution and crowding that accompanied the industrial age's urban centres (Gray, 2013). The compounds utilised in chemical disinfection techniques either generate oxidising compounds or are oxidants themselves. These include: hydroxyl radicals ($\bullet\text{OH}$), hypochlorous acid (HOCl), ozone (O_3) and superoxide anion ($\text{O}_2\bullet^-$). These species are collectively called Reactive Oxygen Species (ROS) (Castro-Alf3rez *et al.*, 2016; Nonell and Flors, 2016).

Thermal disinfection and SODIS are amongst the oldest forms of water disinfection techniques though they are not commonly utilised at scale (Castro-Alf3rez *et al.*, 2016). Solar disinfection utilises ROS to induce microbicide. The ROS in this case include: singlet oxygen ($^1\text{O}_2$), $\text{O}_2\bullet^-$, $\bullet\text{OH}$ and hydrogen peroxide and are generated due to interaction amongst ultraviolet rays, molecular oxygen and the constituent molecules found in cells (Castro-Alf3rez *et al.*, 2016). Thermal disinfection, popularly known as boiling, induces microbicide by denaturing enzymes that are crucial for the survival of the pathogen cell (Cohen, 2020; 3miech *et al.*, 2020).

Chlorination is the most popular of the disinfection methods when utilised on a large scale. Its popularity is mainly based on its ease of operation and relatively low operational costs (Gray, 2013). Chlorination disinfection involves the release of chlorine species into water to induce microbicide. This is done in two major forms: free chlorine and chlorine dioxide. Free chlorine utilizes either hypochlorous acid (HOCl) or hypochlorite ion (OCl^-) to induce microbicide. It involves penetration of the cell via diffusion by HOCl , where HOCl exhausts the cells ability to deal with reactive oxygen species (ROS) by binding and inhibiting enzymes and antioxidants, respectively. The presence of ROS within the constituents of the cell ultimately led to its inactivation and eventual demise (Fukuzaki, 2006).

Chlorine dioxide (ClO_2) is a highly soluble gas in water that diffuses through the membranes of pathogens to gain access to the constituents of the cell. ClO_2 's microbicidal mechanism utilises its oxidative property. It abstracts electrons from the constituent molecules in the membranes of the cell, which include peptidoglycan. Electron abstraction interferes with the interactions amongst bonds responsible for maintaining the integrity of the cytoplasmic membrane. As a result, intracellular components including nucleic acids are leaked into its

external environment and this leads to the eventual inactivation and death of the pathogen (Murray *et al.*, 2013).

Ozonation is a disinfection technique that gained utility due to the works of Siemens in 1867, when it developed a silent discharge apparatus. The silent discharge apparatus allowed the production of ozone in large enough quantities for its properties to be investigated. Among the properties discovered was its effective antimicrobial effects. This led to its use as a disinfectant in a water treatment plant in the Netherlands in 1893 (Gray, 2014). Ozone disinfects via two mechanisms, namely direct oxidation and indirect oxidation. In direct oxidation, as the name implies ozone interacts with molecules in its mesomeric form ([Figure 2](#)) resulting in oxidation of a target molecule.

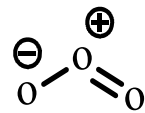


Figure 2:Ozone molecule

Direct oxidation is target specific, reacting with unsaturated compounds, amine and sulfhydryl groups. However, in ‘indirect oxidation’ ozone reacts via •OH. •OH is formed through a chain reaction that is initiated as a result of a reaction between ozone and hydroxyl ions (OH^-). •OH are an indiscriminate reactive species (Rosen *et al.*, 1995). It is by these two mechanisms that ozone induces microbicide (Gottschalk *et al.*, 2010). Ozone reacts with glycoproteins, glycolipids, unsaturated fatty acids and amine and sulfhydryl groups, which make up organelles or constitute the contents of the cells of the pathogen. This leads to lysing and or inactivation of the cell (Méndez-Vilas, 2011).

Among the aforementioned chemical techniques, ozone is the most effective, in that it is able to induce microbicide amongst all the major pathogens. These include: helminths, protozoa, viruses, bacteria and bacterial spores in equal measure (Gray, 2014). It is, therefore, reasonable to hypothesise that chemical disinfectants that produce ROS could also be just as effective. This is observed amongst leucocytes (white blood cells) that have been observed to generate $\text{O}_2^{\bullet-}$ that lead to the formation of •OH as a means to deal with pathogens in the body (Rosen *et al.*, 1995). Examples of other compounds that have been utilised in water disinfection due to their ability to produce ROS are photosensitisers and photocatalysts. They do this by taking advantage of photodynamic action (Thandu *et al.*, 2015).

The techniques above have saved many lives through the years. A summary of various water disinfection techniques is given in [Table 1](#). Some of the disadvantages associated with the techniques above include: toxic by-products for chlorination, cost of operation for ozonation and antimicrobial resistance.

Table 1: Disinfection techniques, advantages and disadvantages

| Method | Technique | Methodology | Advantages | Disadvantages |
|-------------------------|--|---|--|--|
| Physical Methods | UV Radiation ($\lambda=240-280\text{nm}$) | UV rays interact with nucleotides of the cell resulting in mutations and cell death | <ol style="list-style-type: none"> 1. It is a broad spectrum technique 2. No toxic additives | <ol style="list-style-type: none"> 1. Unreliable for water with high turbidity 2. Electricity dependant 3. Leads to mutations that can be dangerous 4. Low penetration depth($\leq 7.5\text{cm}$) |
| | Solar Radiation | 6 hour exposure to sun-light where water is placed in a transparent container | <ol style="list-style-type: none"> 1. Broad spectrum technique 2. It is inexpensive 3. No toxic additives | <ol style="list-style-type: none"> 1. Time consuming 2. Toxic if some plastics are used 3. Limited geographical application |
| | Ultra-sound | 8-20kHz sound pressure result in oscillatory disruptions that generate enough kinetic energy that leading to cell wall disintegration | <ol style="list-style-type: none"> 1. It is a broad spectrum technique 2. No toxic additives | <ol style="list-style-type: none"> 1. Microbes may be able to regenerate after exposure |
| Chemical Methods | Chlorine | Chlorine generates radicals that oxidize pathogens | <ol style="list-style-type: none"> 1. It is effective against bacteria and viruses 2. Inexpensive chemicals are used 3. Is effective at pH less than 8 and greater than 4 4. Produces residual concentration (0.2-0.3mg/L) | <ol style="list-style-type: none"> 1. It is phytotoxic 2. Forms harmful trihalomethanes and endoperoxides in the presence of organic compounds 3. Reduces water quality (taste and odour) 4. Contact time of 30 minutes is required 5. Ineffective against protozoa |
| | Iodine | Iodine forms <i>N</i> -iodo bonds with amino acids and nucleotides, | <ol style="list-style-type: none"> 1. It is a broad spectrum technique (bacteria and parasites) | <ol style="list-style-type: none"> 1. It is required in high concentrations 2. More expensive than chlorine 3. It reduces water quality (taste and colour) |

| Method | Technique | Methodology | Advantages | Disadvantages |
|--------|--|---|---|---|
| | | leading to formation of ineffective proteins | <ol style="list-style-type: none"> 2. It does not react with ammonia and other nitrogen compounds in water 3. Prevents iodine deficiency in the population | <ol style="list-style-type: none"> 4. Microbes have developed resistance |
| | Ozone | Works by releasing oxygen (hydroxyl radicals *OH, *OH ₂ Hydroperoxyl radicals, superoxide radicals, ozone radicals and free oxygen atom) that interferes with the permeability of the cell wall. | <ol style="list-style-type: none"> 1. It is a broad spectrum technique 2. Requires very short contact time (8 seconds in some cases) to induce 99% mortality in bacteria 3. Can be used to extract soluble metals Fe(II) and Mn(II) and soluble sulphur compounds 4. Generated and consumed <i>in situ</i>. | <ol style="list-style-type: none"> 1. It is explosive 2. Irritates skin, eyes and respiratory tracts 3. Can be carcinogenic in the presence of bromine 4. By-products include mutagenic aldehydes 5. Requires consistent supply of electrical power 6. Requires a disinfectant residual to be added after disinfection of water |
| | Hydrogen Peroxide (H ₂ O ₂) | Disinfection involves decomposition of peroxide to produce hydroxyl radicals that oxidize pathogens. | <ol style="list-style-type: none"> 1. It is a broad spectrum technique | <ol style="list-style-type: none"> 1. Irritates eyes and respiratory tracts 2. Exposure to skin results in blisters and burns. 3. High concentrations are needed to achieve disinfection in reasonable time 4. Expensive |

Generated from: (Drinking Water and Health, 1980) (Jyoti and Pandit, 2004) (Jori, 2011) (Sharma and Bhattacharya, 2017) (de Castro Medeiros *et al.*, 2019)

2.5. Microbial Resistance to Disinfectants

Disinfectants are chemical agents that are able to remove virtually all pathogens, except bacterial spores in an inanimate object in which they are engaged (Centers for Disease Control and Prevention, 2023). A microbe is said to be resistant if it is not inactivated or killed by a specific concentration of disinfectant within a period of time that kills or inactivates other microbes. Resistance in microbes may develop as a result of its phenotype or its physical environment or a combination of both (Bridier *et al.*, 2011). Phenotypes are physical manifestations of an organisms' genes.

Resistance conferred by a phenotypic response include: gene coding in multi-drug efflux pumps (organelles that eject toxic material from a cell) (Bridier *et al.*, 2011), reverse engineering a damaged nucleotide under UV radiation at slightly higher wavelengths of 300 nm or in the dark (Bohrerova and Linden, 2006; Wang *et al.*, 2021) and the development of persisters (where pathogens enter highly protective states displaying a lot of resistance) (Bridier *et al.*, 2011).

The physical environment provides resistance for the pathogen by preventing direct contact with the disinfectant. This can be through: particle association, where greater resistance is conferred on the pathogen if the particle simulates the pathogen's host properties (in the case of the *Salmonella typhi* and *E.coli*, it would be faecal matter) and eukaryotic cell encapsulation, where the pathogen is entrapped in the organelles of a eukaryotic cell such as an amoeba's food vacuole (Bridier *et al.*, 2011).

The combination of both a physical and phenotypic response to disinfectants is the formation of a biofilm. A biofilm is a cluster of pathogens about a substrate surrounded by a complex matrix of extrapolymeric substances. The complex matrix provides: a physical barrier from disinfectants, alternative reaction media for strong oxidative species of disinfectants (it is composed of carbohydrates, proteins and nucleotides) and electrostatic barriers where if the disinfectant is either anionic or cationic, the matrix holds it if it has an opposing charge. Phenotypic protection arising from the biofilm is as a result of the stressful conditions under which the pathogens in the biofilm exist (these cells at the periphery receive oxygen and are responsible for protein synthesis while those pathogens at the core of the biofilm have to deal with high concentrations of waste with very little access to oxygen).

These stressful conditions result in gene expressions that confer protection upon pathogens within the biofilm. These gene expressions can further be transferred to other pathogens in the biofilm through lateral gene transfer thus ensuring propagation of resistance to the population of the biofilm. For example, *Pseudomonas aeruginosa* (*P. aeruginosa*) conducts lateral gene transfer in colonies composed of the *P. aeruginosa* species only. Biofilms have resulted to 100-fold increases in concentrations of disinfectants so as to fully inactivate initially susceptible pathogens (Bridier *et al.*, 2011). For disinfectants such as chlorine, which upon interaction with organic compounds generate toxic by-products this would be a dangerous endeavour (Galal-Gorchev, 1996; Gray, 2013).

As of 1986, resistance in pathogens for disinfectants was still minor and thus disinfectants could still be a guaranteed mode of treating drinking water (Hoff and Akin, 1986). However, as time has gone by, pathogens have continued to adapt and adapt well. Thus, novel techniques that are insusceptible to their adaptations are increasingly necessary. One such technique that is yet to be resisted is photodynamic effect (Xu *et al.*, 2016) and its application in photodynamic water disinfection.

2.6. Photodynamic Approach to Water Disinfection

Photodynamic approach to water disinfection refers to the use of photodynamic effect to disinfect water. The photodynamic effect describes biological damage caused by the resultant effect of combining three actors: light, a photosensitizer molecule (PS) and molecular oxygen. Photosensitizer molecules are molecules that induce photoexcitation in other molecules as a consequence of their own photoexcitation (Wardle, 2009). They are also known as photocatalysts. Literature has tried to distinguish the two terms by stating that photocatalysts refer to inorganic compounds and photosensitisers refer to organic compounds (Thandu *et al.*, 2015). Photosensitisers were discovered first and photocatalysts developed thereafter. Photosensitisers were discovered by Oscar Raab and his assistant von Tappeiner in 1900 when they discovered the cidal effects of acridyne dye in cells. Von Tappeiner coined the term 'photodynamic effect' to describe the collective action of a photosensitiser, light and oxygen to induce cell death in 1907 (Craig *et al.*, 2015; Jori, 2011).

The exogenous application of photosensitisers to treat disease is called photodynamic therapy. A photon of sufficient energy (wavelength) excites a photosensitizer molecule's electron to an excited singlet state (1PS), where it can undergo intersystem crossing to its triplet state (3PS). If it decays to its lowest excited singlet state (through vibrational decay modes), it is then able to interact with molecular oxygen in one of two ways. This is either through electron transfer to a substrate resulting in an oxygen radical (3O_2) or other organic radicals (type I mechanism) or energy transfer, whose consequence is then formation of singlet oxygen (1O_2) (type II mechanism) as shown in [Figure 3](#).

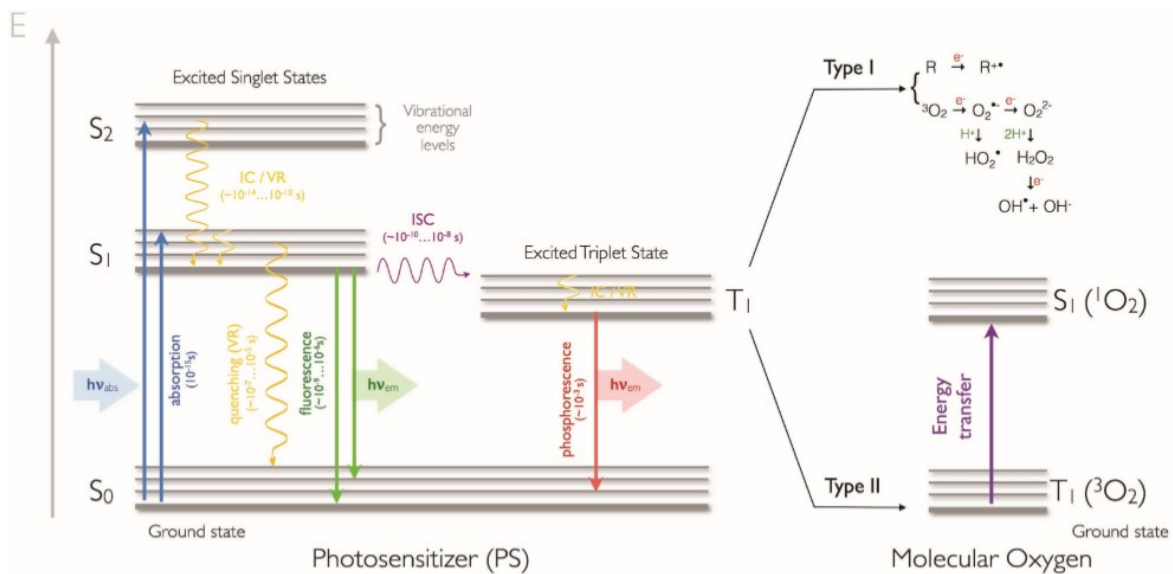


Figure 3: Jablonski diagram (Lismont *et al.*, 2017)

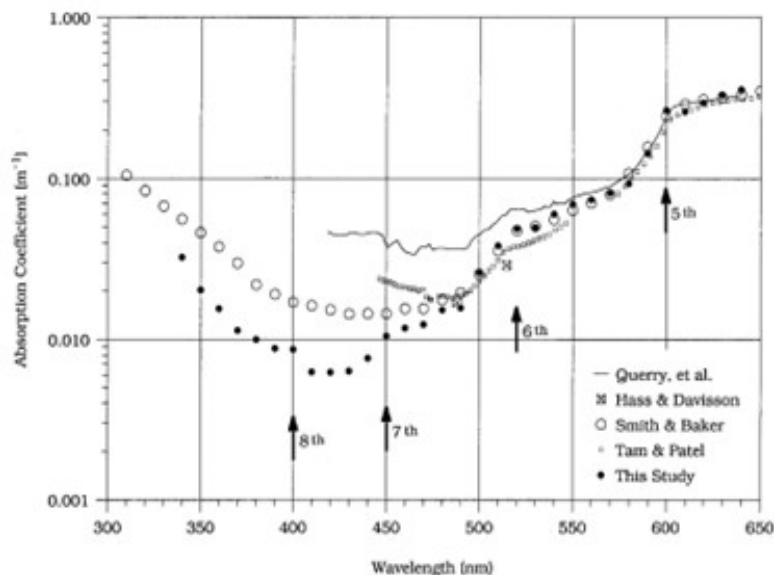
They do this to molecules that have lower lying energy levels through a myriad of mechanisms including coulombic mechanism, electron exchange mechanism or trivial mechanism (Wardle, 2009). In either case, the resultant oxygen species interacts with biological systems to their detriment (Cieplik *et al.*, 2018; Jori, 2011). Of the two reaction mechanisms, type II is more common (Cieplik *et al.*, 2018). 1O_2 is an energized form of molecular oxygen. It is the lowest excited state form of molecular oxygen. The energy difference between the two states is 95KJ/mol. 1O_2 is called singlet oxygen on account of its multiplicity. Ground state oxygen has a multiplicity of three and can thus be called triplet oxygen (3O_2), while singlet oxygen (1O_2)

has a multiplicity of 1 and is thus called singlet. This is best illustrated through a Jablonski diagram, as shown in [Figure 3](#).

There are important requirements for an effective photosensitiser in water disinfection (Jori, 2011; Thandu *et al.*, 2015): absorbance should be in the range of 400-450 nm (photo-aquatic zone (PAZ)), photo-stability, should have low fluorescence quantum yield, high singlet oxygen quantum yield and solubility in water.

2.6.1. Strong Absorbance in the Photo-aquatic Zone

The need for this criteria is guided by the interaction between water and light. Water absorbs least light in the photo-aquatic zone (PAZ) (400-450 nm), as shown in [Figure 4](#) (Pegau *et al.*, 1997).



Selected pure-water absorption spectra representative of variability in published data. Shoulders corresponding to harmonics of the O-H stretch are indicated by arrows.

Figure 4: Water's UV-Vis spectra (Pegau *et al.*, 1997)

It follows therefore with less impediment of photons in this zone, they would be able to reach the PS and it in turn will be able to absorb the required light. That said, a large molar absorption coefficient (ϵ) for the PS would also be a good feature as it would mean a lower dose of PS would be utilised. One of the impediments to enhancing the molar absorbance coefficient of

porphyrins is their tendency to agglomerate, due to π - π stacking (Zhu *et al.*, 2022). This makes it difficult for porphyrins to remain in their monomeric form.

2.6.2. Photo-stability

Photo-stability refers to the ability of a molecule to maintain its structural integrity upon its interaction with light. In essence, the photosensitiser is to act like a catalyst enabling a transformation but able to return to its original state. Porphyrins are favoured in this case as only one in 10,000 molecules undergo photo-oxidation in the presence of light (Jori, 2011). An example of molecules that do not maintain structural integrity in the presence of light are those that take part in [4+2] cycloaddition reaction. The reaction is triggered by an interaction between light and two molecules, the consequence of which is the formation of a cyclohexene. In this case both molecules lose their structural nor molecular integrity.

2.6.3. Low Fluorescence Quantum Yield

Fluorescence quantum yield (Φ_f) refers to the ratio of photons emitted during fluorescence relative to those absorbed by a molecule. A low Φ_f is favoured in photosensitisers as it is an indicator that more electrons have undergone intersystem crossing (ISC). This means more electrons can be used to transfer energy to $^3\text{O}_2$. Φ_f is measured by comparing the area under the graph of a fluorescence spectra for a molecule with a known Φ_f . This comparison is made possible because Φ_f is independent of wavelength (Wardle, 2009). Factors affecting Φ_f include, one, rigidity of the molecule, where there is direct proportionality in this relationship, a molecule that maintains its geometry in the excited state has a higher Φ_f . Two, congruence between excited state and ground state, where increased congruence is directly proportional to Φ_f , where excited state orbitals are dissimilar, the rate of relaxation is reduced and this gives an opportunity for a slower process to occur, this includes ISC. Three, substituent effect, electron donating groups increase Φ_f while electron withdrawing groups decrease Φ_f . (Wardle, 2009).

2.6.4. High Singlet Oxygen Quantum Yield

Singlet oxygen quantum yield refers to the ratio of singlet oxygen ($^1\text{O}_2$) molecules generated relative to the photons absorbed by a molecule. Singlet oxygen is relevant to the potency of the PS as it is the primary antimicrobial agent.

2.6.5. Solubility in Water

Since photodynamic water disinfection is carried out in water, the photosensitiser should be soluble in water in order to permeate and freely gain access to microbes. Porphyrins are illustrative of this property due to their affinity to accumulate in tumours. This makes them an excellent choice for use in treating cancers (Managa *et al.*, 2015).

2.7. Photodynamic Inactivation of Pathogens

Photodynamic inactivation of pathogens can rely on the charge of the PS molecule and the surface charge of the microbial cell as an important determinant of whether a PS molecule will induce death in a pathogen. Generally, anionic and neutral PS molecules kill gram-positive pathogens, while cationic PS molecules will induce death in gram-negative bacteria such as *E. coli* and gram-positive bacteria such as *Staphylococcus aureus* (Jori, 2011). The PS molecules act by attaching to microbes by electrostatic forces within an incubation period of 1-10 minutes before their activation is most potent (Cieplik *et al.*, 2018).

Within the cell, the singlet oxygen will then interact with nucleophilic constituents of the cell resulting in oxidized products that are unable to perform their intended functions. These nucleophilic constituents contain electron rich nitrogen and sulphur atoms. They include macromolecules such as proteins, lipids and nucleic acids. The consequence of oxidation of these constituents include: protein denaturation, impairment of DNA replication, degradation of transport mechanisms across membranes (cell and organelles) and the loss of efficacy in several organelles (Jori, 2011). The common occurrence of these constituents in all pathogens helps to make photodynamic approach a broad spectrum disinfection technique (Wainwright, 1998).

Majority of the studies on photodynamic inactivation of pathogens have demonstrated the enhanced potency of cationic PS molecules over anionic ones. However, in a recent study it has been observed that neutral porphyrins possess similar potency against both gram-negative and gram-positive bacteria. This potency was attributed to the substitution pattern on the porphyrin (Xu *et al.*, 2016).

2.8. Porphyrins

The term porphyrin is derived from ‘porphyra’, the Greek word for purple, this was on account of their characteristic purple and red colour (Senge *et al.*, 2021). Porphyrins are macromolecules composed of four pyrrole rings joined together via *meso*-carbons along the α -position of the pyrrole rings. The result is a hetero-atomic structure composed of 22π electrons, however its aromaticity is derived from the 18π electrons in its inner core (bonds coloured red, as shown in [Figure 5](#)) (Mack, 2017).

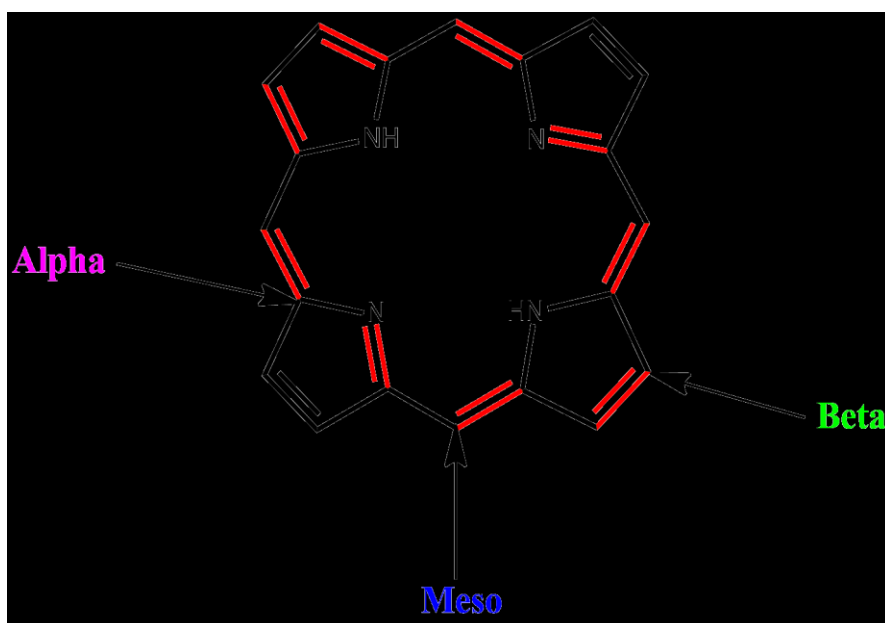
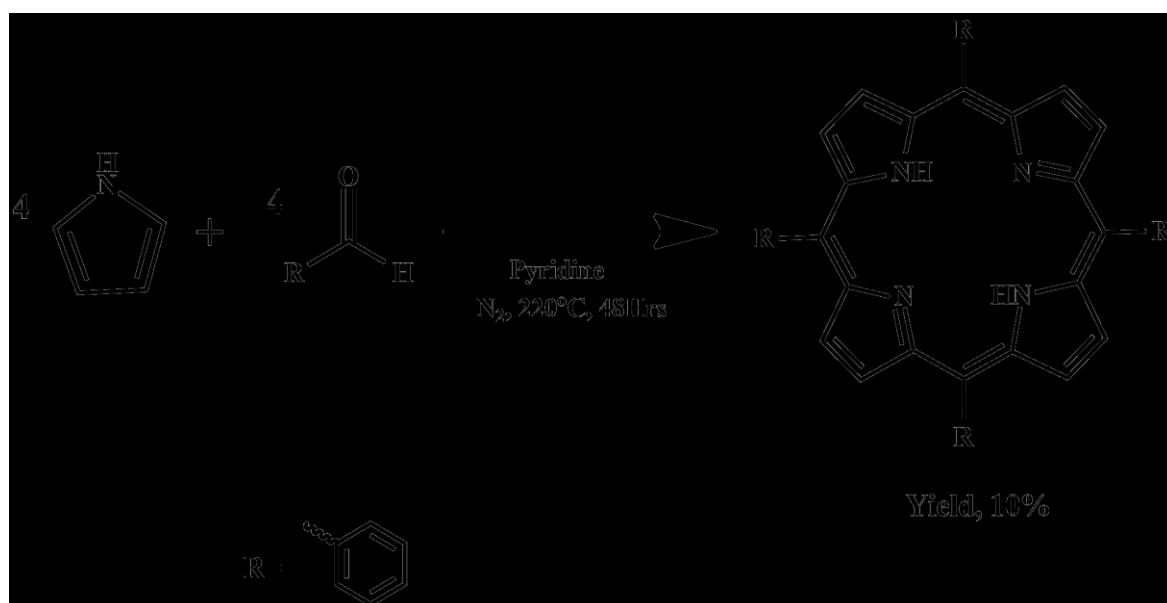


Figure 5: General aromatic porphyrin structure with positions' labels

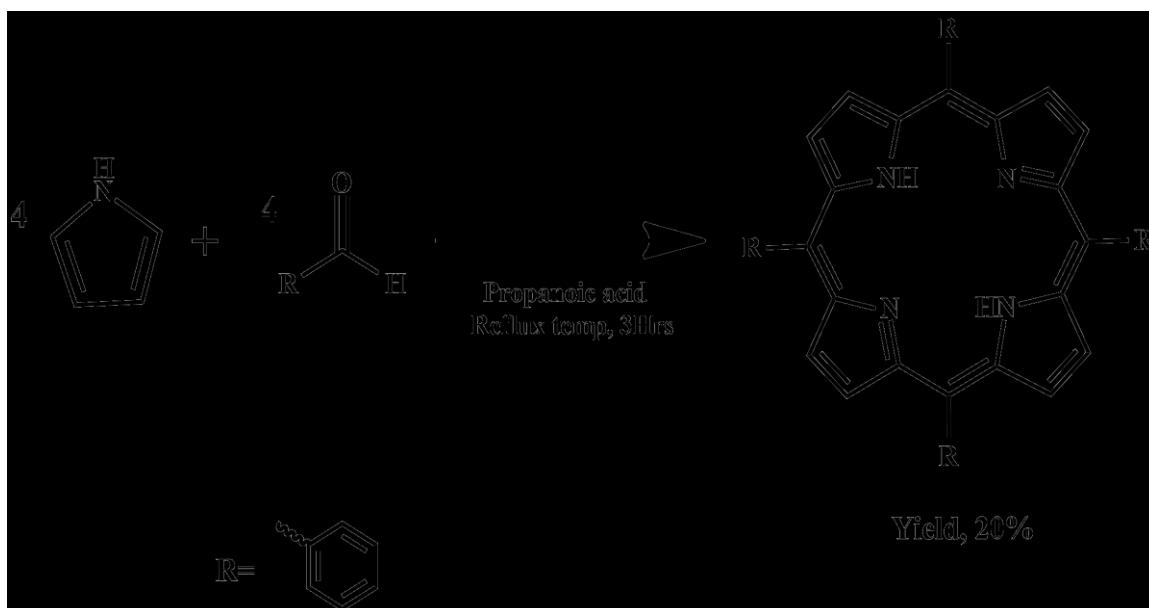
The diversity of applications of porphyrins encompass their natural roles as well as their synthetic applications. They feature as: enzyme cofactors, electron and exciton shuttles (Wardle, 2009), signalling molecules, cancer therapy agents, photodynamic therapy (PDT) (Hally *et al.*, 2018), solar energy converters (Chu *et al.*, 2019), catalysts and theranostic agents (Hally *et al.*, 2018; Senge *et al.*, 2021). These features are possible because porphyrins undergo redox reactions as in photosynthesis and photochemical reactions based on photodynamic therapy (PDT) (Babu *et al.*, 2019; Senge *et al.*, 2021). The basis for the versatility of porphyrins resides in the molecular properties of porphyrin.

2.8.1. Synthesis of Porphyrins

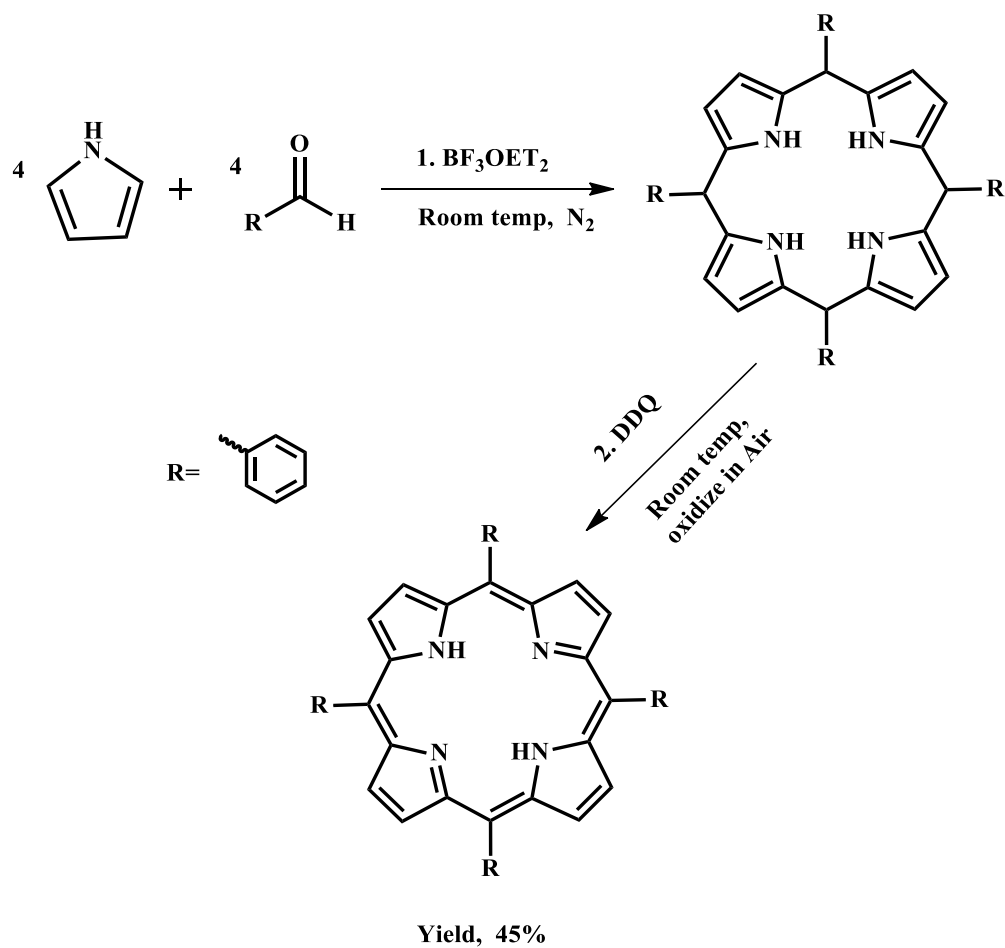
The synthetic pathways of porphyrins are generally condensation reactions between four equivalents of pyrrole and four equivalents of an aldehyde under varying reaction conditions. In order to have a *meso*-tetra-substituted porphyrin one of the hydrogen atoms in the formyl group is simply substituted with a desired substituent. The three common synthetic pathways are: Rothmund synthetic pathway ([Scheme 1](#)), Adler – Longo synthetic pathway ([Scheme 2](#)) and Lindsey synthetic pathway ([Scheme 3](#)).



Scheme 1: Rothmund synthetic pathway

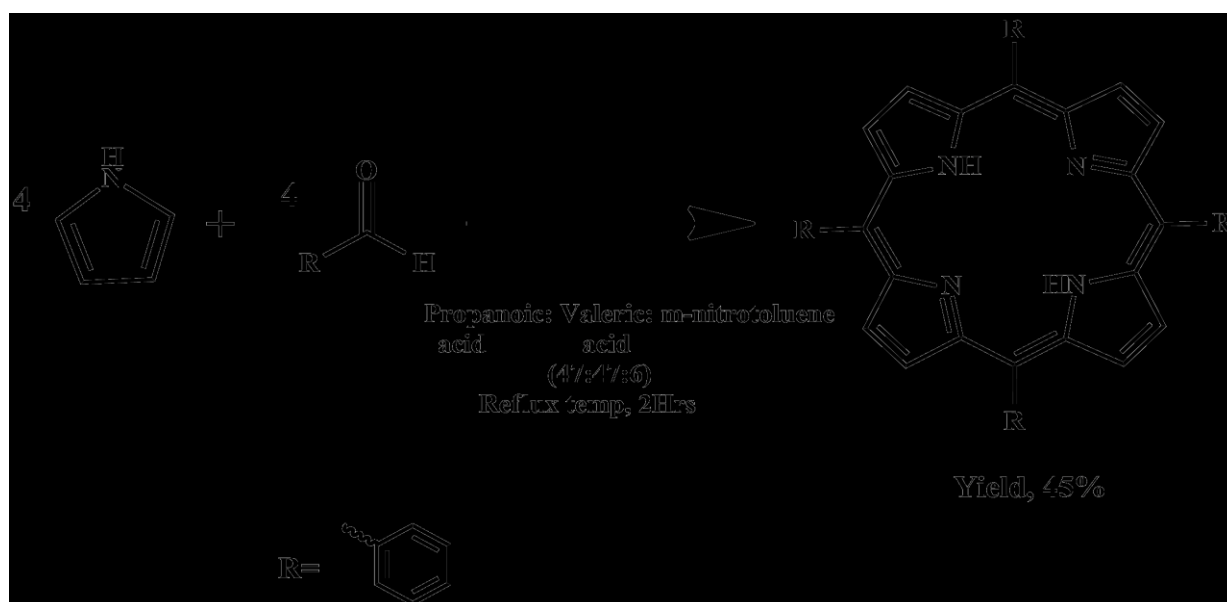


Scheme 2: Adler-Longo synthetic pathway



Scheme 3: Lindsey synthetic pathway

They are all one-pot synthetic pathways (Li *et al.*, 1997; Senge *et al.*, 2021; Sun *et al.*, 2013, 2019). Rothmund synthesis was developed by Rothmund and others in 1940 and involves heating a mixture of pyrrole and an aldehyde with pyridine as a solvent under an inert atmosphere (nitrogen). The yield for Rothmund synthesis is about 10%. Adler-Longo synthetic pathway involves refluxing in propanoic acid; a mixture of pyrrole and aldehyde at temperatures of 141°C. (Gonsalves *et al.*, 1991). Adler-Longo pathway was developed in 1945 and was an improvement of Rothmund's method both in terms of yield and ease of execution because it no longer needed an inert atmosphere. It involves Studies by Sun *et al.*, (2013) showed that refluxing in a mixture of propanoic, valeric and *m*-nitrotoluene in a ratio of 47:47:6, could improve the porphyrin's yield as shown in [Scheme 4](#).



Scheme 4: Mixed-solvent system (Adler Longo) pathway

The Lindsey synthesis is a one-pot two step synthetic pathway involving a Lewis acid (boron trifluoridedietherate, BF_3OEt_2) as a catalyst to form a porphyrinogen that gets oxidized by 2,3-dichloro-5,6-dicyanobenzoquinone (DDQ) to form a porphyrin. The first step is done under an inert atmosphere while the second is in air. The reaction conditions for Lindsey synthesis are mild (room temperature) (Lindsey, 2010; Sun *et al.*, 2013). Lindsey's method was especially useful for aldehydes that are not stable at temperatures above room temperature. The synthetic

methods highlighted enabled variation in the photo-physical properties of porphyrins, providing opportunities for their application in many fields.

2.8.2. Photo-physical Properties of Porphyrins

The photo-physical properties of porphyrins are mainly viewed through the lens of the ultra-violet and visible (UV-Vis) light portion of the electromagnetic spectrum. Within this range, porphyrins have a distinct pattern of spectral bands. There is a characteristic strong band known as the Soret band or B band between 400 and 480nm and subsequently four weak consecutively diminishing bands known as Q bands between 500 and 700nm (Zhang *et al.*, 2017) (Figure 6).

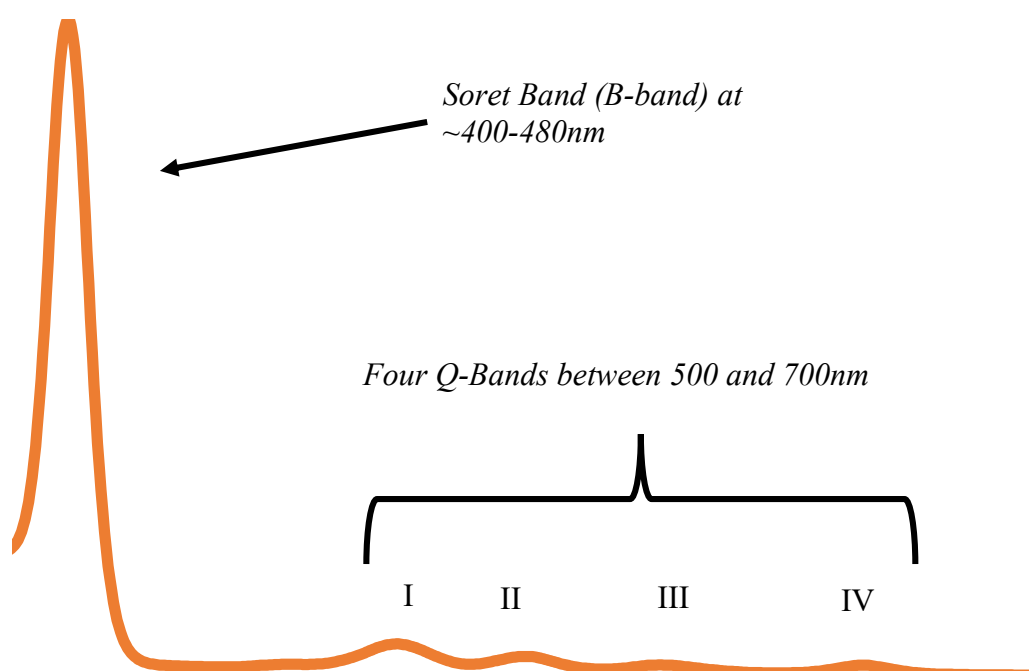


Figure 6: Generalised UV-Vis spectra of a porphyrin molecule

The UV-Vis properties of a porphyrin molecule can be tuned by adding or removing moieties at different points on the porphyrin scaffold (Zheng *et al.*, 2008). These include: addition of metals at the core of the porphyrin and removing, adding or modifying substituents on the *beta* (β) or *meso* positions of the porphyrin, as shown in Figure 5. Porphyrins have a central diameter of between 1.929 and 2.098 Angstrom. This large cavity allows porphyrins to act as ligands and allow even metals that are far larger than the space they provide to occupy it. The existence of such a large cavity is significant in photodynamic effect due to the heavy atom effect that encourages ISC. Porphyrins can also be structurally modified to accompany heavy atoms

through covalent bonds with heavy halides at their *meso*-positions (Mack, 2017). Each of these modifications can alter the positions of the spectral bands or alter their intensity or in the case of metallation with respect to Q-bands, change their number from 4 to 3, 2 or 1.

The use of magnetic circular dichroism has facilitated the testing and confirmation of theories on the molecular properties of porphyrins postulated by Michl and Gouterman (Mack, 2017). The theories account for the distinct UV-Vis spectra of metallated and free base porphyrins based on molecular orbital theory. They confirmed that the UV-Vis peaks observed in porphyrins were due to π - π transitions amongst the frontier orbitals rather than n- π transitions.

Q-bands were observed to come from spin forbidden transitions, $\Delta M_l=9$ (M_l is magnetic quantum number), the name is derived from the Japanese name for nine, 'kyu'. While the Soret band were derived from spin allowed transitions, $\Delta M_l=1$, this also explains why their peaks are so much stronger. The Q-band peaks are observable despite being forbidden due to vibrational borrowing from the spin allowed B-bands (Mack *et al.*, 2007). Through these theories, it is possible to utilize computational chemistry to model porphyrin molecules with an aim of predicting their photo-physical properties including UV-Vis spectroscopy via density functional theory (DFT) (Mack *et al.*, 2005).

2.8.3. Computational Chemistry in Selection of Porphyrins for Various Applications

Computational chemistry is the field of chemistry that uses theoretical models to predict the properties of a molecule. A theoretical model is a way to describe a specific set of approximations. The approximations are then combined with a calculation algorithm and are applied to atomic orbitals. Atomic orbitals are in turn defined by basis sets, which are a set of wave functions that describe the shape of atomic orbitals. Theoretical models are thus used to compute molecular orbitals and their energies.

There are four main types of theoretical models: semi-empirical, ab-initio, density functional theory (DFT) and molecular mechanics (MM) (Jensen, 2017; Tomberg, 2019). Ab-initio, means from the beginning and its methods include those that are derived from theoretical principles only. Examples include Hartree-Fock method. As its name implies the semi-empirical theoretical model are those that use experimental data to determine the results of their calculations. Examples include ZINDO. MM are those models that model atoms as spheres and

bonds as springs and an algebraic equation is used for energy calculations, an example of an MM model is universal force field (UFF). It is used for both organic and inorganic molecules (Jensen, 2017; Tomberg, 2019). DFT is an exact theory, this means that given the right functional, it would be able to describe a system perfectly, however, this has not happened yet (Goerigk and Mehta, 2019).

In DFT, electron density is used to compute minimum energy, this produces results comparable to ab-initio methods but with the added advantage of less processing time and costs, examples of DFT functionals include: Becke's-3 Lee, Yand and Parr (B3LYP) and coulomb attenuating method B3LYP(CAM-B3LYP) (Cramer, 2004; 2019; Oyim *et al.*, 2022; Yanai *et al.*, 2004).

One of the most fundamental properties in selecting a porphyrin for water disinfection is where the wavelength of its Soret band lies. This can be modelled using DFT through its time dependent variant, known as time-dependent density functional theory (TD-DFT). TD-DFT is a DFT calculation that obtains wave functions for molecular orbitals oscillating between its excited states and ground state. This provides the added advantage of not only saving time and resources but enables an in-depth analysis of the behaviour of a particular molecule. A chemist, therefore, has the opportunity to improve on the molecule they are working on and also test his/her modifications to observe whether they will have the desired result.

DFT models have shown to provide relatively good approximations especially in the case of porphyrins (Babu *et al.*, 2019; Hanna *et al.*, 2022). The procedure involves, optimizing the geometry of the molecule, this establishes the ground state of all the orbitals and their energies, then the molecule is run through TD-DFT to establish the oscillator strengths (f) and wavelengths of the transitions the molecule goes through. DFT is a relatively cheap method with regard to processing costs. Computation also allows chemists to vary the environment of the molecule, this is whether the computations are performed in a vacuum or in a solvent such as water or dichloromethane (DCM) (Xue *et al.*, 2016). The ease with which porphyrins can be modified have allowed them to be utilised in many different applications.

2.8.4. Photodynamic Applications of Porphyrins

The photosensitizer properties of porphyrins have found uses in photodynamic chemotherapy (PDT), as a treatment for exogenous infections and in water disinfection. Cationic tetra-

meso(*N*-methylpyridyl) porphine (TMPyP ([Figure 7](#))) has been used in treating *Saprolegnia* infected rainbow trout in aquaculture.

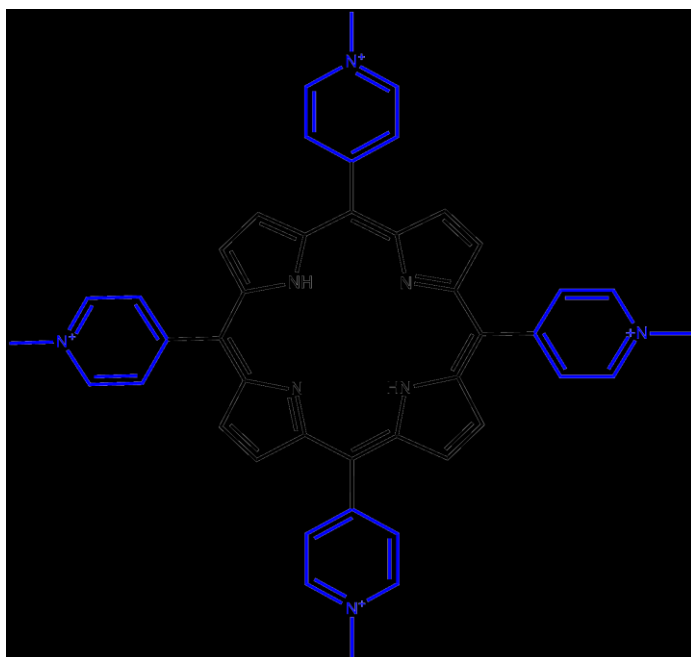


Figure 7: Tetra(*N*-methylpyridyl)porphine (TMPyP)

Saprolegnia infections were reported as cotton-like patches on the scales of the trout. After application of TMPyP for 10 consecutive days for 1 hour daily, the infection cleared. Furthermore, because such treatment was conducted under a wattage of 50mW/cm², the study concluded that it could serve aquaculture farms that had infected fish even on a cloudy day (Jori, 2011).

Porphyrins have also been used as metal organic frameworks (MOFs) for the purpose of water disinfection. MOFs are crystalline porous scaffolds that are periodically assembled and sustained by strong dative bonds between positively charged metal or metal clusters (also known as an inorganic building unit (IBU) (or a secondary building unit and a negatively charged organic ligand (also known as an organic building unit (OBU)) ([Figure 8](#)).

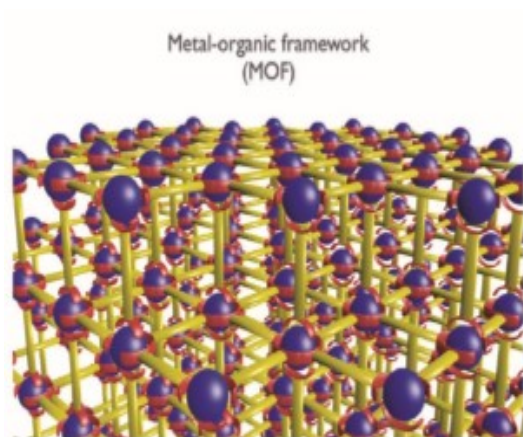


Figure 8: Schematic of a metal organic framework, (Lismont *et al.*, 2017)

IBUs act as ‘linkers’ while OBU act as ‘struts’. The porphyrins form the three-dimensional (3D) porous structure and also act as the microbicide (Lismont *et al.*, 2017). MOFs can also occur as two-dimensional (2D) frameworks. Porphyrins used in this way are more effective because factors such as π - π stacking are eliminated (π - π stacking leads to agglomeration (clumping) of the porphyrins), thus the porphyrins exist in their monomeric forms in MOFs. This means that more porphyrins are able to interact with light. Furthermore, there is increased contact with microbes, because the resultant 3D structure has a large volume to surface area ratio (Zhu *et al.*, 2022). Zhu *et al.*, 2022 were able to synthesise 2D 4,4',4'',4'''-(porphyrin-5,10,15,20-tetrayl)tetrabenzoic acid (2DTcpp) (Figure 9), which achieved a log 6 reduction of bacteria within 30 minutes.

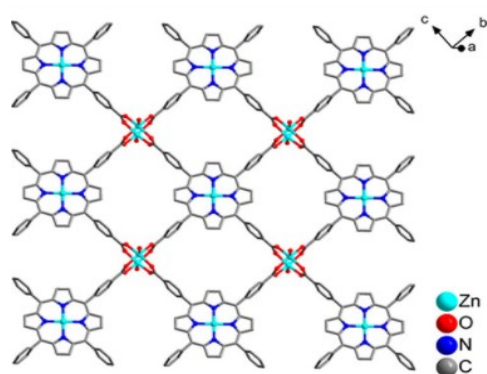


Figure 9: 2D 4,4',4'',4'''-(porphyrin-5,10,15,20-tetrayl)tetrabenzoic acid Metal Organic Framework, (Zhu *et al.*, 2022)

In this study, porphyrins were synthesised and investigated for their antimicrobial activity and their potential application in water disinfection.

CHAPTER 3: MATERIALS AND METHODS

3.1. Materials

3.1.1. *General instrumentation*

The instruments that facilitated this project included a 430 nm light emitting diode (LED) from ThorLabs, Infrared spectroscopy was conducted using a Jasco FT/IR-4700 Fourier Transform Infrared spectrometer. UV-Vis spectroscopy was performed using a Shimadzu 1800 spectrophotometer UV-1800 and fluorescence spectroscopy and fluorescence quantum yield were determined via a Shimadzu RF-6000 spectro-fluorophotometer. NMR spectra were obtained from a Bruker 80 MHz NMR spectrometer with residual protons of deuterated chloroform (CDCl_3) as the reference standard and CDCl_3 as the solvent. Mass spectrometry data were recorded from a Bruker Auto FLEX III Smartbeam MALDI-TOF mass spectrometer, and dithranol was used in positive ion mode as the matrix.

3.1.2. *Reagents*

The reagents used in realising the objectives of this project included hexaaquanickel(II)chloride ($[\text{NiCl}_2 \cdot 6\text{H}_2\text{O}]$) from Merck. Pyrrole (98% pure) was further purified by distillation at 140°C before use, (5-bromo-thiophen-2-yl)aldehyde, hexaaquacobalt(II)chloride ($[\text{CoCl}_2 \cdot 6\text{H}_2\text{O}]$), zinc(II)acetate ($\text{Zn}(\text{OAc})_2$), indium(III)chloride (InCl_3), hexaaquatin(IV)chloride ($\text{SnCl}_2 \cdot 2\text{H}_2\text{O}$), hydroxypyridine, iron(III)chloride (FeCl_3), sodium hydroxide (NaOH), anhydrous sodium sulphate (Na_2SO_4) and hydrated sodium acetate ($\text{NaOAc} \cdot 3\text{H}_2\text{O}$) were procured from Sigma-Aldrich, while all solvents were procured from either Loba Chemie, India or Sigma Aldrich, USA. The solvents were dried using molecular sieves 3\AA procured from Loba Chemie, India. Aluminium oxide powder (alumina) was purchased from Machery-Nagel, Germany. The powder was baked for 24 hours at 100°C before use. Unless otherwise stated, all reagents were used without further purification.

3.2. Methods

The methods used for: synthesis, photo-physical studies, theoretical studies and antimicrobial studies are highlighted below.

3.2.1. Synthesis Procedures

The synthetic procedures used for BTP and its metal analogues are summarised below.

3.2.1.1. Synthesis of *Meso*-tetra(5-bromothiophen-2-yl)porphyrin (BTP)

The synthesis of BTP was conducted using a slightly modified procedure from Sun *et al*, (2013). It involved adding 5-bromothiophen-2-ylaldehyde (1.911 g, 0.01 moles) and pyrrole (0.6709 g, 0.01 moles) in a 250 mL two-necked round-bottom flask and refluxing in a mixture of 100 mL propanoic acid, valeric acid and *m*-nitrotoluene (ratio, 47:47:6) for 2 hours. The resultant product was filtered under vacuum to yield a black cake. The black cake was then dissolved in dry dichloromethane (DCM). The resultant solution was then run through an alumina column eluting with dry DCM to afford a purple powder (0.345 g, 13% yield). UV-Vis (dimethylsulphoxide(DMSO)): 430.50, 524, 563, 596.5 and 660.5 nm. ¹H NMR (80 MHz, CDCl₃): δ 8.72 (d, *J*=4Hz, 8H, β-Pyrrole), δ 7.42 (d, *J*=4Hz, 4H thiophenyl) δ 7.26 (d, *J*=4 Hz, 4H, thiophenyl) and δ -3.27 (2H, core H). MALDI-TOF MS (*m/z*) calc: 953.71, found 955.47 [M+2H]²⁺, 877.484[M-Br]⁺¹. FTIR: ~3300 cm⁻¹ (N-H vibration)

3.2.1.2. Synthesis of *Meso*-tetra(5-bromothiophen-2-yl)porphyrinato Zinc(II) (Zn-BTP)

The synthesis of Zn-BTP was achieved using a procedure that was slightly modified from literature (Khisra, 2020; Oloo, 2020). It began with BTP (52.6 mg, 55.11 μmoles) and zinc(II)acetate (38.09 mg, 173.5 μmoles) being added to 45 mL of a mixture of DCM and methanol (3:1) and stirred at room temperature in a round bottom flask for 24 hrs. The progress of reaction was followed via UV spectroscopy. The reaction mixture was placed in a 500 mL separatory funnel, diluted with 100 mL of distilled water and extracted with DCM (100 mL x 3). The combined DCM extracts were dried over anhydrous sodium sulphate for 2 hours, filtered and concentrated *in vacuo*. The crude extract was purified on a column of alumina using dry DCM as the eluent to obtain Zn-BTP as a purple powder (37.01 mg, 66%). UV-Vis (DMSO): 437, 567 and 611 nm. ¹H NMR (80 MHz, CDCl₃) peaks: δ 9.10 (s, 8H, β-Pyrrole), δ 7.53 (s, 4H, thiophenyl) and δ 7.38 (s, 4H, thiophenyl). MALDI-TOF MS (*m/z*) calc: 1017.62, found 1017.390 [M], 938.397 [M-Br]⁺¹.

3.2.1.3. Synthesis of *Meso*-tetra(5-bromothiophen-2-yl)porphyrinato Indium(III)chloride (In-BTP)

The synthesis of In-BTP employed a modified literature method (Khisra, 2020; Oloo, 2020). Indium(III)chloride (41.57 mg, 188 μ moles) and sodium acetate (42.63 mg, 313.3 μ moles) were dissolved with stirring in hot acetic acid (60 °C) in a 100 mL two-necked round bottom flask. BTP (59.8 mg, 62.66 μ moles) was added and the temperature raised to reflux for 24 hours. The progress of the reaction was followed via UV spectroscopy. The reaction mixture was allowed to cool to room temperature and then neutralised with a solution of sodium hydroxide (35 g of NaOH dissolved in 100 mL of distilled water) in a 500 mL separatory funnel. The mixture was extracted with DCM (100 mL x 3). The combined DCM extracts were dried with anhydrous sodium sulphate for 2 hours and concentrated *in vacuo*. The crude extract was purified over a column of alumina with dry DCM as the eluent to provide In-BTP as a purple powder (37.27 mg, 54%). UV-Vis (DMSO): 441.5, 570.5, 616 nm. ¹H NMR (80 MHz, CDCl₃) peaks: δ 9.17 (s, 8H, β -Pyrrole), δ 7.54 (d, $J=4$ Hz, 4H, thiophenyl) and δ 7.36 (s, 4H, thiophenyl). MALDI-TOF MS (m/z) calc: 1101.57, found 1068.357 [M-Cl+2H]⁺³.

3.2.1.4. Synthesis of *Meso*-tetra (5-bromothiophen-2-yl) porphyrinato Tin(IV)hydroxide (Sn-BTP)

The synthesis of Sn-BTP was achieved using a slightly modified procedure from literature (Arnold, 1988; Babu *et al.*, 2019). Diaquatin(IV)chloride (79.34 mg, 351.6 μ moles) was dissolved with stirring in hot pyridine (45 mL at 60°C) in a 100 mL two-necked round bottom flask. Afterwards, BTP (167.8 mg, 175.8 μ moles) was added and the temperature raised to reflux for 24 hours. The progress of the reaction was followed via UV spectroscopy. The reaction mixture was allowed to cool to room temperature and was then concentrated *in vacuo* via co-rotavaping with toluene (45 mL x 3). The crude extract was purified over an alumina column with dry chloroform as the eluent to give Sn-BTP, a dark-green powder (64.14 mg, 33%). UV-Vis (DMSO) 446, 572.5 and 620 nm. ¹H NMR (80MHz, CDCl₃) peaks: δ 9.29 (s, 8H, β -Pyrrole), δ 7.63 (d, $J= 3.2$ Hz, 4H, thiophenyl) and δ 7.42 (4H, thiophenyl). MALDI-TOF MS (m/z) calc: 1105.60, found 1107.329 [M+2H]⁺².

3.2.1.5. Synthesis of *Meso*-tetra(5-bromothiophen-2-yl)porphyrinato Tin(IV)dioxypyridine (Pyr-BTP)

The synthesis of Pyr-BTP was achieved through slightly modified methods from literature (Arnold, 1988; Babu *et al.*, 2019). Firstly, Sn-BTP (38.5 mg, 34.83 μ moles) and hydroxypyridine (6.8 mg, 71.5 μ moles) were dissolved in hot pyridine (45 mL at 60 °C) in a 100 mL two-necked round bottom flask. The temperature was then increased to reflux for four hours. The progress of the reaction was marked via UV-Vis spectroscopy. The reaction mixture was concentrated *in vacuo* via co-rotavaping with toluene (45 mL x 3). The crude extract was purified over an alumina column with dry chloroform as the eluent to give Pyr-BTP, a green powder (12.70 mg, 29%). UV-Vis (DMSO) 442.5, 569 and 616nm. MALDI-TOF MS (m/z) calc:1257.66, found 1260.308 [M+3H]⁺³.

3.2.1.6. Synthesis of *Meso*-tetra(5-bromothiophen-2-yl)porphyrinato Iron(III)chloride (Fe-BTP)

The synthesis of Fe-BTP involved dissolving iron(III)chloride (28.04 mg, 172.9 μ moles) and sodium acetate (39.21 mg, 288.1 μ moles) in hot acetic acid (45 mL at 60 °C) with stirring in a two-necked 100 mL round bottom flask. Afterwards, BTP (58 mg, 60.77 μ moles) was added and the temperature raised to a reflux for 24 hours. The progress of the reaction was followed via UV-Vis spectroscopy. The reaction mixture was allowed to cool to room temperature and neutralised with sodium hydroxide (35 g of NaOH dissolved in 100 mL of distilled water) in a 500 mL separatory funnel. The reaction mixture was extracted with dry DCM. (100 mL x 3). The combined DCM extracts were then dried over anhydrous sodium sulphate for 2 hours and concentrated *in vacuo*. The crude extract was purified over two alumina columns. The first with DCM as the eluent and the second with ethyl acetate and acetone (1:1) as the eluent to afford Fe-BTP as a brown-green powder (25.34 mg, 40%). UV-Vis (DMSO): 417.5, 576, and 619.5 nm. MALDI-TOF MS (m/z) calc: 1042.60, found 1008.032 [M-Cl + H]⁺².

3.2.1.7. Synthesis of *Meso*-tetra(5-bromothiophen-2-yl)porphyrinato Cobalt (II) (Co-BTP)

Synthesis of Co-BTP involved dissolving [CoCl₂•6H₂O] (38.4 mg,161.4 μ moles) and sodium acetate (35.65 mg, 262.2 μ moles) in hot acetic acid (45 mL at 60 °C) with stirring in a two-necked 100 mL round bottom flask. Afterwards, BTP (52.4 mg, 54.90 μ moles) was added and

the temperature raised to reflux for 24 hours. The progress of the reaction was monitored via UV-Vis spectroscopy. The reaction mixture was allowed to cool to room temperature and neutralised with sodium hydroxide solution (35 g of NaOH dissolved in 100 mL of distilled water) in a 500 mL separatory funnel. The reaction mixture was then extracted with dry DCM. (100 mL x 3). The combined DCM extracts were dried with anhydrous sodium sulphate for 2 hours and concentrated *in vacuo*. The crude extract was purified over an alumina column with dry DCM as the eluent to afford Co-BTP as a brown powder (23.30 mg, 42%). UV-Vis (DMSO): 447, 560 and 605.5 nm. MALDI-TOF MS (m/z) calc: 1010.63, found 1011.83 [M+H]⁺¹.

3.2.1.8. Synthesis of *Meso*-tetra(5-bromothiophen-2-yl)porphyrinato Nickel (II) (Ni-BTP)

The synthesis of Ni-BTP involved dissolving [NiCl₂•6H₂O] (36.98 mg, 155.6 μmoles) and sodium acetate (35.29mg, 259.3 μmoles) in hot acetic acid (45 mL at 60 °C) with stirring in a two-necked 100 mL round bottom flask. Afterwards, BTP (49.5mg, 51.86 μmoles) was added and the temperature raised to reflux for 24 hours. The progress of the reaction was followed via UV-Vis spectroscopy. The reaction mixture was allowed to cool to room temperature and neutralised with sodium hydroxide solution (35 g of sodium hydroxide dissolved in 100 mL of distilled water) in a 500 mL separatory funnel. The mixture was extracted with dry DCM. (100 mL x 3). The DCM fractions were combined and dried over anhydrous sodium sulphate for 2 hours and concentrated *in vacuo*. The crude extract was purified over an alumina column with dry DCM as the eluent to afford Ni-BTP as a red powder (13.61 mg, 26%). UV-Vis (DMSO): 428 and 539 nm. MALDI-TOF MS (m/z) calc: 1009.63, found 1012.179 [M+3H]⁺³.

3.2.2. Photo-physical Studies

The photo-physical studies performed on BTP and its metal analogues included UV-Vis spectroscopy and Infrared spectroscopy.

3.2.2.1. UV-Vis spectroscopy

UV-Vis spectroscopy was used to determine the molar absorptivity coefficient (ϵ) of each molecule that was synthesised. This involved preparing initial stock solutions of concentrations that provided sharp peaks on the Soret band and then diluting these concentrations thrice more. Once an absorbance of 1 was attained for the Soret band, this was chosen as the first absorbance, the concentration was then serially diluted so that this concentration was halved twice more. The resultant absorbance measurements were then plotted against concentration to find molar absorption coefficient (ϵ). This was calculated using the Beer Lamberts Law [Equation \(1\)](#), which equates absorbance to the product of concentration, c and length of the cuvette, l (the glass cuvette had a width of 1cm) and ϵ .

$$A = \epsilon c l \dots\dots\dots \text{Equation (1)}$$

3.2.2.2. Fluorescence and Fluorescence Quantum Yield

Fluorescence and fluorescence quantum yield (Φ_f) were obtained on a fluorophotometer using a standard (std) of tetraphenylporphyrinato zinc(II) (ZnTPP) with a fluorescence quantum yield of 0.033 (Φ_{std}). The measurement was done in toluene, which has a refractive index of 1.4968 (n_{std}) (Khisa, 2020; Oloo, 2020). The solvent used to measure the Φ_f of the samples was DMSO, and it has a refractive index of 1.4772 (n). It was possible to compute the fluorescence quantum yield of the metallated and free-base porphyrins from this standard because fluorescence quantum yield is independent of wavelength, this is based on Kasha's rule (Wardle, 2009). The UV-Vis absorbance of the sample was read first and the samples of the porphyrins used had an absorbance of 1, and were excited at 400nm. Φ_f was read directly from the fluorophotometer, the fluorescence spectra were generated simultaneously with Φ_f . The values for Φ_f were calculated manually using [Equation \(2\)](#).

$$\Phi_f = \Phi_{fstd} \frac{F A_{std} (n)^2}{F_{std} A (n_{std})^2} \dots \dots \dots \text{Equation (2)}$$

Φ_f = Fluorescence quantum yield
 F = Area under a peak
 n = refractive index
 A = optical absorbance
 std = standard

3.2.3. Theoretical Studies

Theoretical modelling was done through Gaussian09 software (Trucks *et al.*, 2013). The theoretical model used was density functional theory (DFT) though the functionals B3LYP and CAM- B3LYP. Generally, the basis set used was 6-311g(d) except for the larger metals like indium and tin, where the basis set used was Stuttgart-Dresden (SDD). The molecules' geometries were optimised and then their UV-Vis properties were simulated using time-dependent density functional theory (TD-DFT). These properties were simulated in vacuum and solvent conditions. To simulate solvent conditions, polarizable continuum model (PCM) was used (Oloo, 2020; Oyim *et al.*, 2022).

3.2.4. Antimicrobial Studies

Gram-positive methicillin resistant *Staphylococcus aureus* (MRSA) and gram-negative carbapenem resistant *Escherichia coli* (CRE. coli) were thawed from a freezer at 37 °C and transferred to nutrient agar plates to facilitate growth for 24 hours. The bacteria were then collected with a sterile swab and inoculated onto a nutrient broth for three days. Their absorbance was tested at 600 nm and then utilised in bacterial studies when their absorbance ranged between 0.6 and 0.8 for both bacteria for 100 µL of bacteria.

100 µL of bacteria was tested against 100 µL of porphyrins of varying concentrations in triplicate in a 96-well plate. The concentrations were generated from a stock solution of 500 µM of the porphyrin, the stock solution was composed of 5% DMSO and 95% phosphate buffer solution (PBS). The concentrations used in the 96 well plate were 20, 40, 60, 80 and 100 µM.

One positive and one negative control were used. The negative control contained 200 μL PBS only, whereas the positive control contained 200 μL of the bacteria only.

The plates were then divided into two, one for dark conditions and the other for light conditions. For the dark conditions: the plate's absorbance was tested before incubation and tested again after 24 hours of incubation. While for the light conditions: the plate was exposed to light conditions and then its absorbance measured, after which it was incubated for 24 hours and its absorbance measured again. The light condition was: 10-minutes exposure to 430 nm light. Percentage cell viability (antimicrobial activity) was then calculated as the ratio between the average change of the absorbance over 24 hours relative to the average change for the positive control, as shown in [Equation\(3\)](#).

$$\text{Antimicrobial activity} = \frac{\Delta \text{ Average Abs(sample)}}{\Delta \text{ Average Abs(Control)}} \times 100 \dots\dots\dots \text{Equation(3)}$$

Key:

Abs= Absorbance

Δ = Change

CHAPTER 4: RESULTS AND DISCUSSION

4.1. Outline of the Study

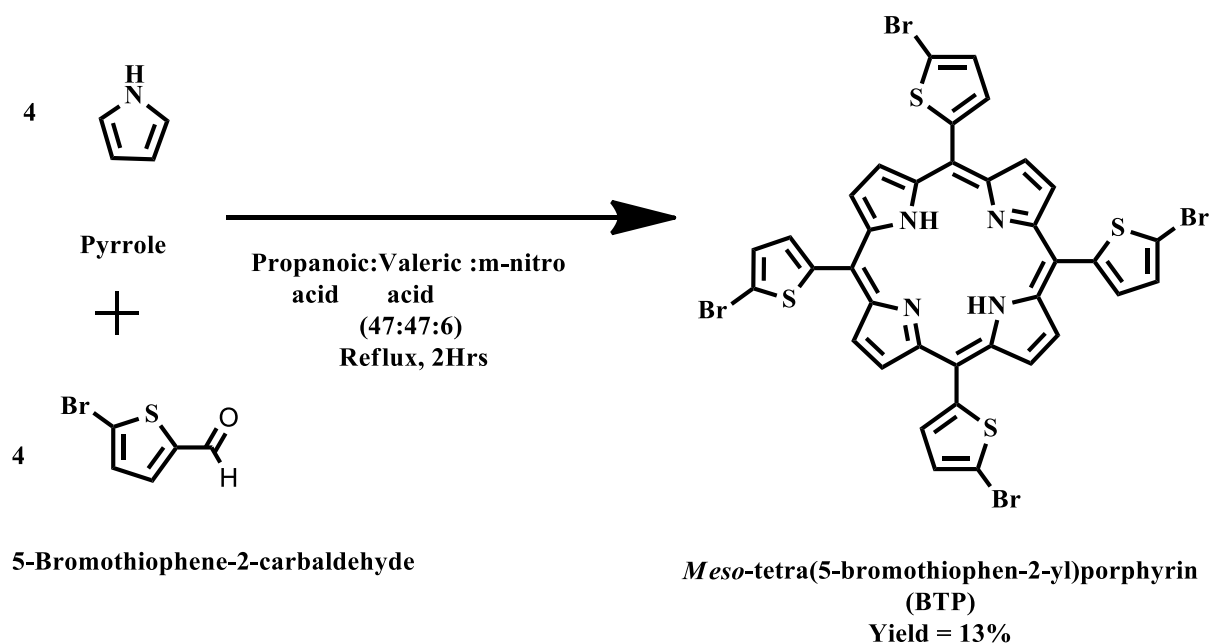
This study involved synthesis of: 5,10,15,20-tetra(5-bromothiophen-2-yl) porphyrin (BTP) and its metal analogues, determination of their photo-physical properties, performing theoretical studies on the synthesised compounds and finally four of the compounds including the free-base had their antimicrobial activity established. In total 8 molecules were synthesised comprising of BTP, 6 metallated derivatives (Zn, In, Fe, Co, Ni and Sn) analogues of BTP. The 8 molecules were synthesised with the aim of optimising BTP for water disinfection.

4.2. Synthesis and Characterisation of the Porphyrins

The synthesis and structure elucidation of the 8 porphyrins are illustrated below.

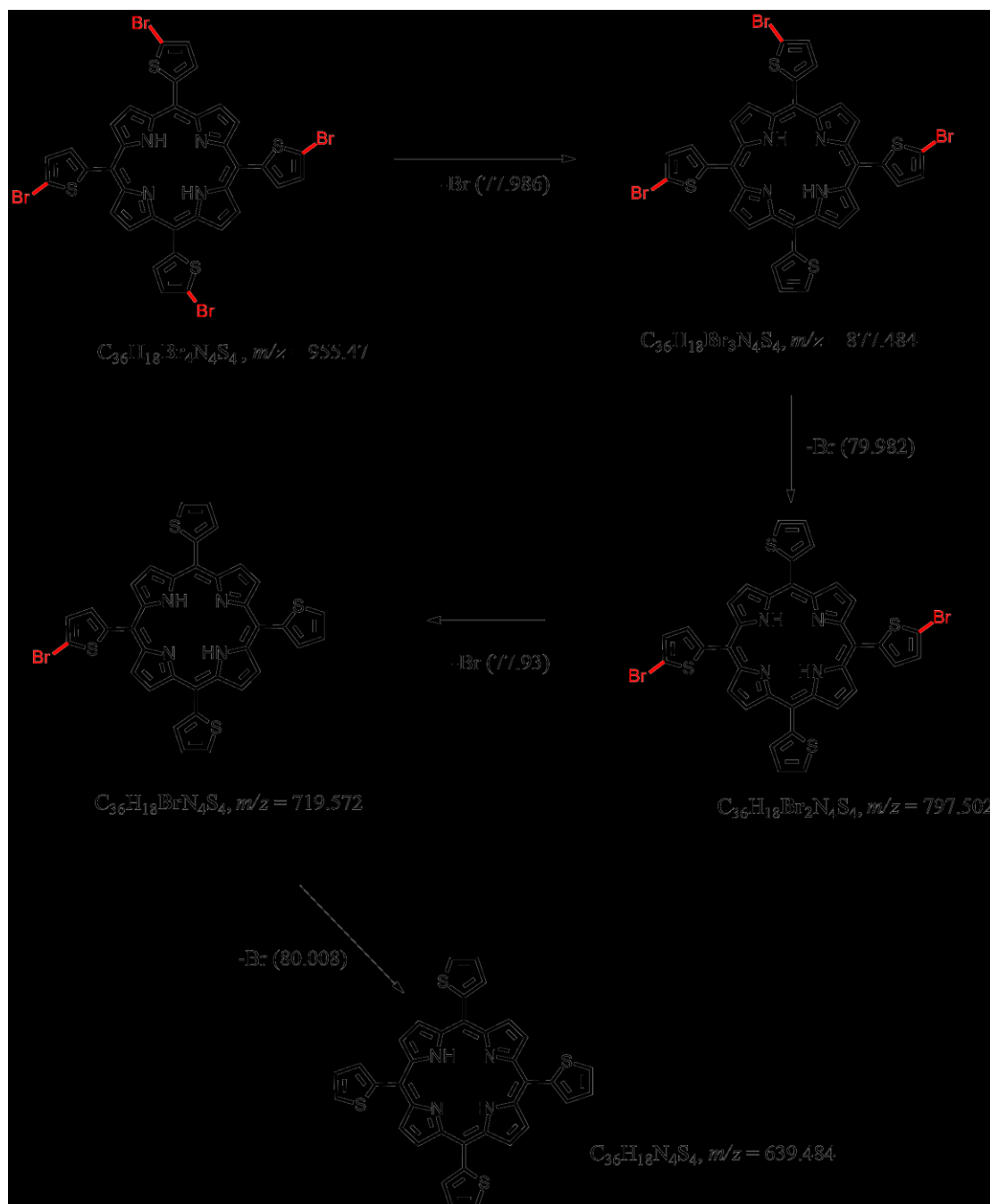
4.2.1. Synthesis of *Meso*-tetra(5-bromothiophen-2-yl)porphyrin (BTP)

BTP was synthesised according to protocol from literature as shown in [Scheme 5](#) (Sun *et al.*, 2013).



Scheme 5: Synthesis of *meso*-tetra(5-bromothiophen-2-yl)porphyrin [*m*-nitro = *m*-nitrotoluene]

The product was isolated as a purple powder. The mass spectrum of BTP showed a molecular ion peak (m/z) of 955.477, corresponding to an empirical formula of $C_{36}H_{18}Br_4N_4S_4$. Subsequent fragment peaks showed m/z of 877.484, 797.502, 719.527 and 639.484 as shown in [Scheme 6](#).

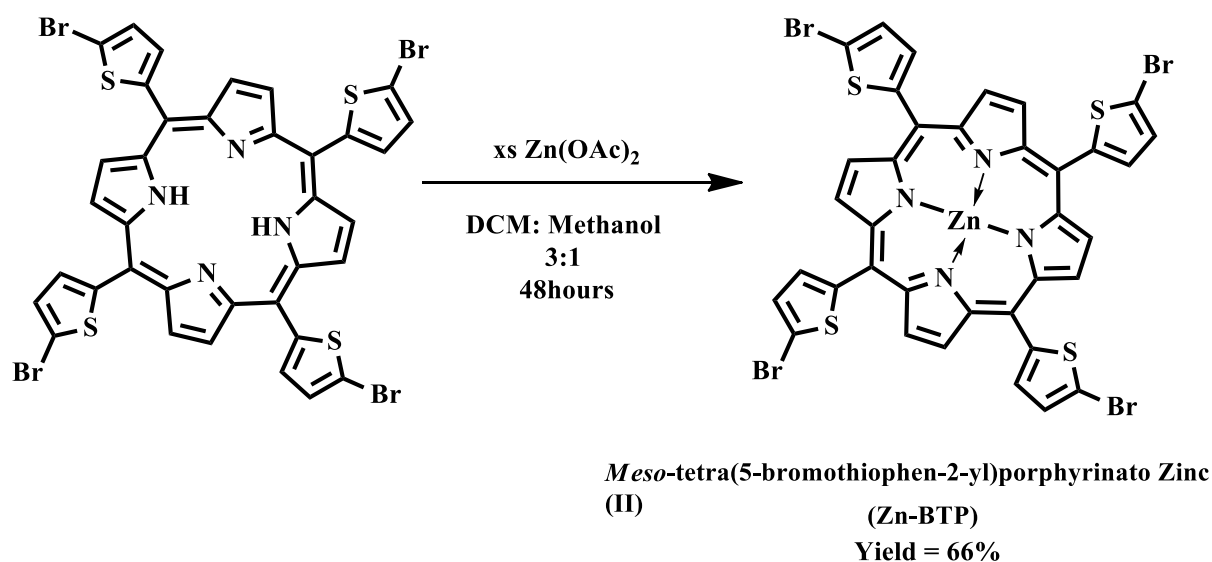


Scheme 6: Fragmentation pattern of *meso*-tetra(5-bromothiophen-2-yl)porphyrin in a mass spectrometer

The difference between the peaks corresponds to the fragment peaks arising from loss of bromine which would be either 79 or 81 (these represent the two isotopes of bromine) give or take some hydrogen ions. The UV-Vis spectrum of BTP had its Soret band at 430.5 nm, and four Q bands at 524, 563, 596.5 and 660 nm. The four Q bands and a strong soret band are characteristic of a free-base porphyrin (Mack, 2017). ¹H NMR spectra showed a peak at δ -3.27 (2H, core H)), which is characteristic of core hydrogens in porphyrins. The core is highly shielded due to the anisotropic effect of the porphyrin ring (Arnold, 1988; Wang and Wamser, 2015) FTIR provided further evidence of the core hydrogen with a peak at 3310 cm^{-1} which is characteristic of an N-H stretch (Oloo, 2020).

4.2.2. Synthesis of *Meso-tetra(5-bromothiophen-2-yl)porphyrinato Zinc (II) (Zn-BTP)*

The synthesis of Zn-BTP followed a protocol from literature, where BTP was metallated with zinc as shown in [Scheme 7](#) (Khisa, 2020; Oloo, 2020).



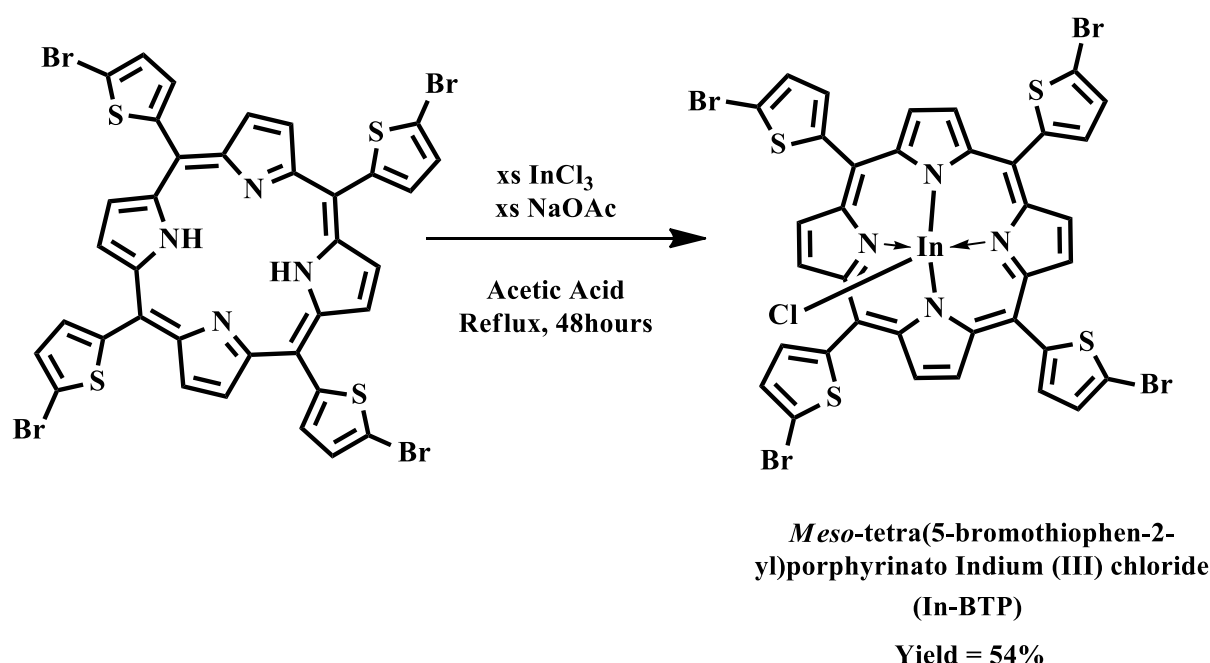
Scheme 7: Synthesis of *meso-tetra(5-bromothiophen-2-yl)porphyrinato Zinc (II)*

Upon metallation, the porphyrin molecules de-protonates and forms a di-anionic ligand, the metal thus acts as a Lewis acid that accepts electrons from the ligand (Marsh and Mink, 1996). Consequently, Zn-BTP was isolated as a purple powder, whose m/z was 1017.390, which corresponded to an empirical formula of $\text{C}_{36}\text{H}_{16}\text{Br}_4\text{S}_4\text{Zn}$. Subsequent fragment peaks observed were progressively reduced by the approximate m/z of a bromine atom, 79 or 81. This is also similar to the pattern observed in BTP's mass spectra ([Scheme 6](#)). Its UV-Vis bands were: 437

nm for its Soret band and 567 and 611 nm for its Q bands, which confirmed successful metallation (Oloo, 2020). Metallation was further confirmed by the absence of a shielded hydrogen peak at δ - 3.27, as shown in [Appendix 2. 2](#).

4.2.3. Synthesis of *Meso-tetra(5-bromothiophen-2-yl)porphyrinato Indium (III) chloride (In-BTP)*

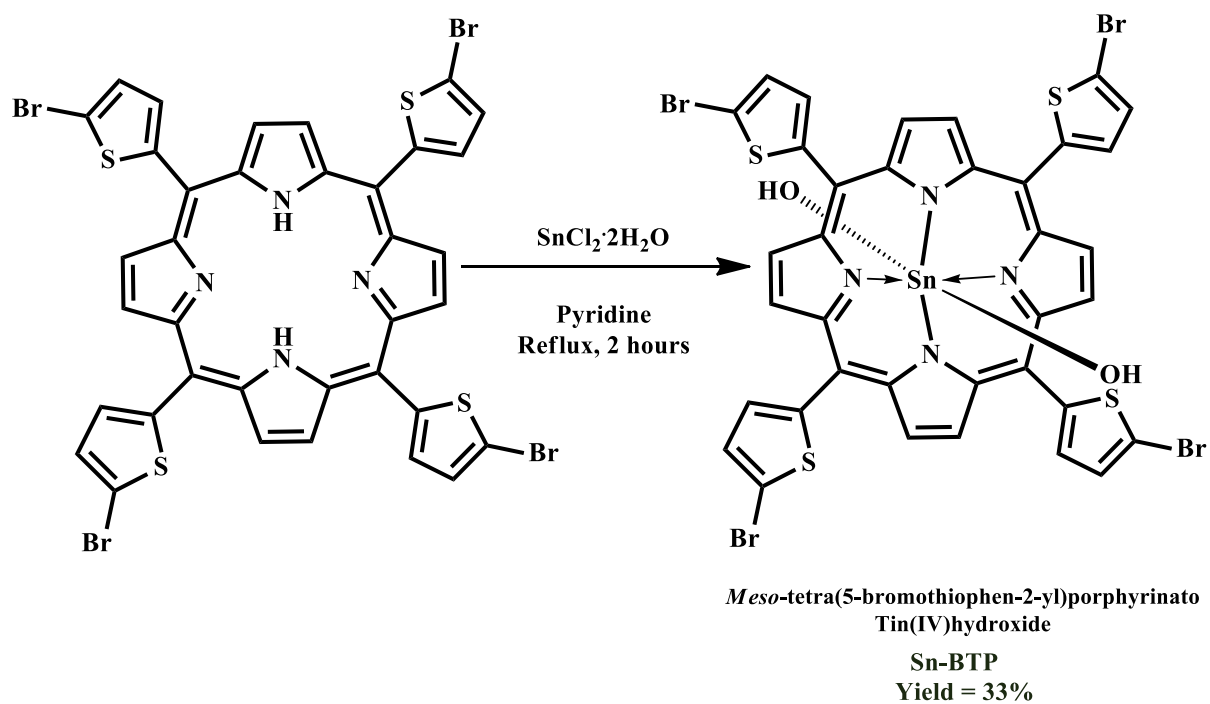
The synthesis of In-BTP was done according to a protocol described by Oloo (2020) in literature by metallating BTP with Indium as shown in [Scheme 8](#).



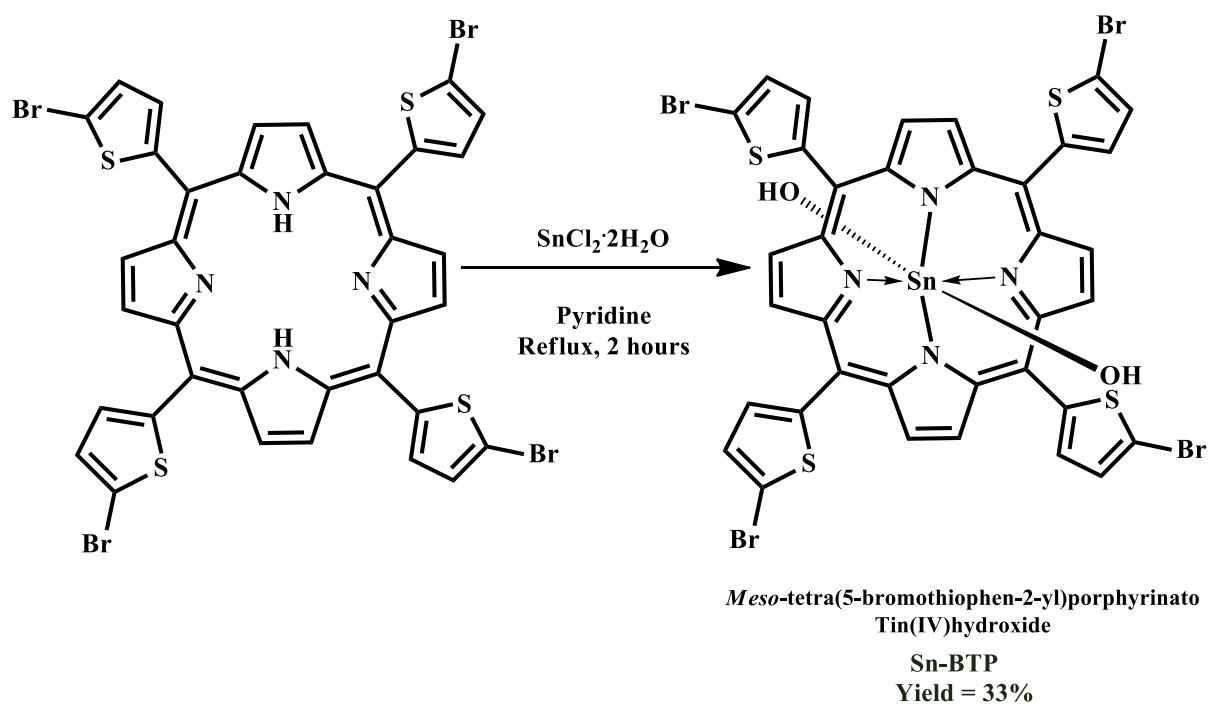
Scheme 8: Synthesis of *meso-tetra(5-bromothiophen-2-yl)porphyrinato Indium (III) chloride*. Consequently, In-BTP was a purple powder whose m/z was 1068.357, which corresponded to an empirical formula of $C_{36}H_{16}Br_4S_4In$. The same pattern of peaks as those in Zn-BTP and BTP was observed. Its UV-Vis bands were at 441.5 nm for its Soret band and 570.5 and 616 nm for its Q bands. In addition to the reduction in Q band peaks, successful metallation was further confirmed via 1H NMR by the absence of a peak at δ -3.27, as shown in [Appendix 2. 3](#).

4.2.4. Synthesis of *Meso-tetra(5-bromothiophen-2-yl)porphyrinato Tin(IV)hydroxide (Sn-BTP)*

The metallation of BTP with Sn to provide Sn-BTP was achieved following a literature protocol (Arnold, 1988; Babu *et al.*, 2019). This is illustrated in



Scheme 9



Scheme 9: Synthesis of *meso*-tetra(5-bromothiophen-2-yl)porphyrinato Tin(IV)hydroxide

As a result, Sn-BTP was isolated as a dark-green powder. The value of m/z of 1107.329

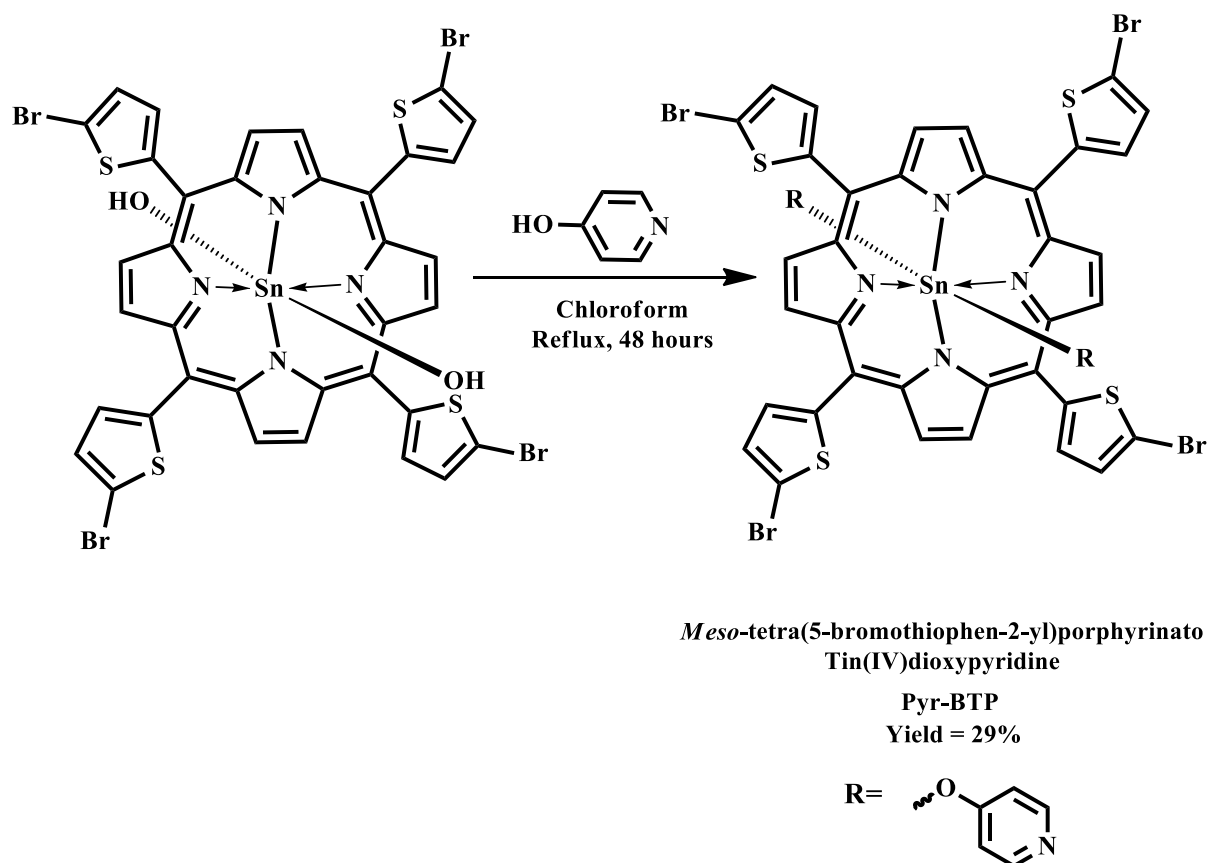
corresponded to a formula of $C_{36}H_{18}Br_4N_4O_2S_4Sn$. The mass spectra confirmed the successful

metallation of BTP with tin. The UV-Vis bands were 446 nm for the Soret band and 572 and 620 nm for the Q bands. Metallation was proven further by the absence of a peak at δ -3.27, as shown in

[Appendix 2.4.](#)

4.2.5. Synthesis of *Meso*-tetra(5-bromothiophen-2-yl)porphyrinato Tin(IV)dioxypyridine (Pyr-BTP)

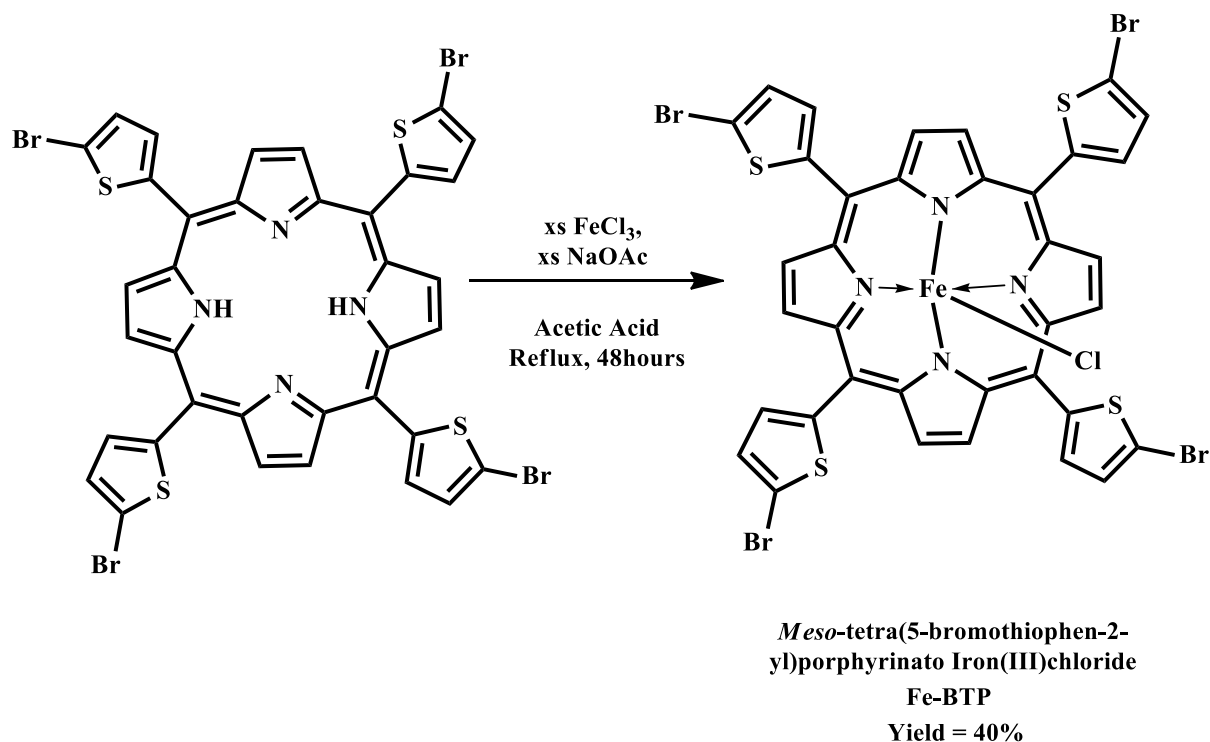
The synthesis of Pyr-BTP was achieved according to literature protocol, where Sn-BTP was axially ligated with hydroxypyridine as shown in [Scheme 10](#) (Arnold, 1988; Babu *et al.*, 2019).



Scheme 10: Synthesis of *meso*-tetra(5-bromothiophen-2-yl)porphyrinato Tin(IV)dioxypyridine. Consequently, Pyr-BTP was isolated as a green powder. The UV bands were 442.5 nm for the Soret band and 569 and 616 nm for the Q bands. The slight shift in the bands signified successful axial ligation. Successful axial ligation was further shown through the mass spectra of Pyr-BTP, which showed a m/z of 1260.308 which corresponded to an empirical formula of $C_{46}H_{24}Br_4N_6O_2S_4Sn$. This value was 152.979 greater than the m/z peak of Sn-BTP (1107.329), which corresponded to the approximate mass of two pyridine molecules.

4.2.6. Synthesis of *Meso*-tetra(5-bromothiophen-2-yl)porphyrinato Iron(III)chloride (Fe-BTP)

The synthesis of Fe-BTP involved metallating BTP with iron as shown in [Scheme 11](#).

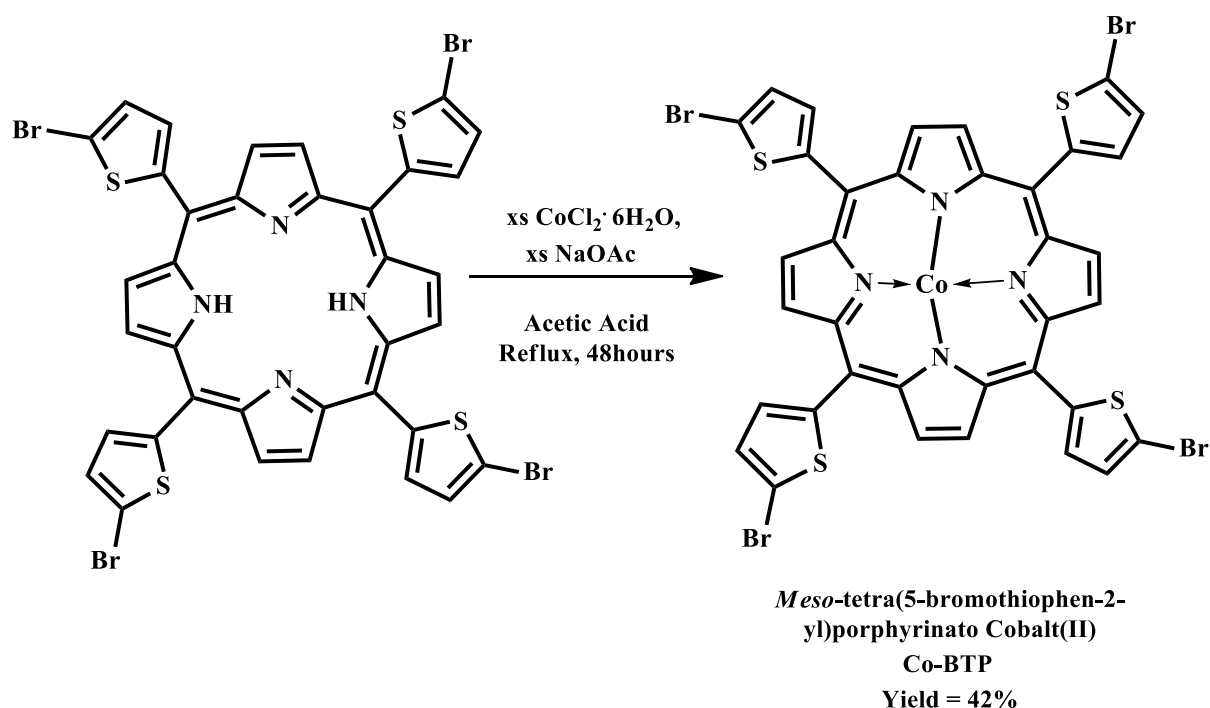


Scheme 11: Synthesis of *meso*-tetra(5-bromothiophen-2-yl)porphyrinato Iron(III)chloride

As a result, Fe-BTP was isolated as a green-brown powder whose m/z was 1008.032. This corresponded to an empirical formula of $C_{36}H_{16}Br_4S_4Fe$. This change in m/z was an indication of successful metallation of BTP with iron. Fe-BTP's UV-Vis bands were at 417.5 nm for its Soret band and 576 and 619.5 nm for its Q bands. The combination of the blue-shift observed in the Soret band relative to BTP as well as the reduction of Q bands from four to two were indicative of successful metallation.

4.2.7. Synthesis of *Meso*-tetra(5-bromothiophen-2-yl)porphyrinato Cobalt(II) (Co-BTP)

Following a protocol provided in literature (Khisra, 2020; Oloo, 2020), BTP was metallated with cobalt as shown in [Scheme 12](#).

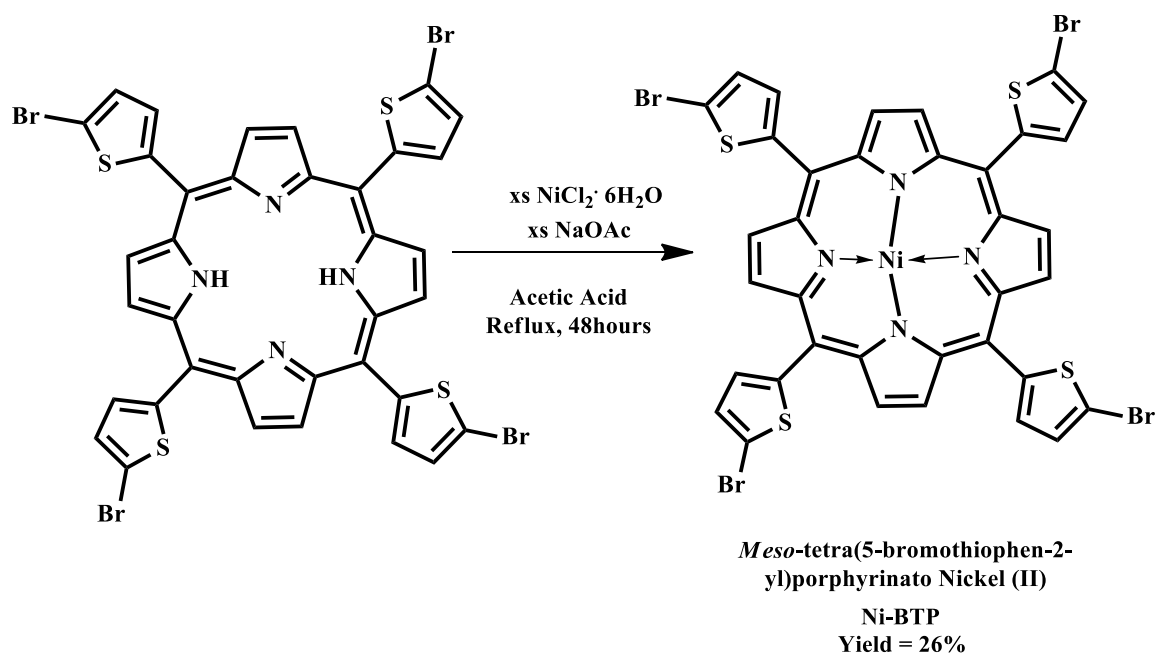


Scheme 12: Synthesis of *meso*-tetra(5-bromothiophen-2-yl)porphyrinato Cobalt(II)

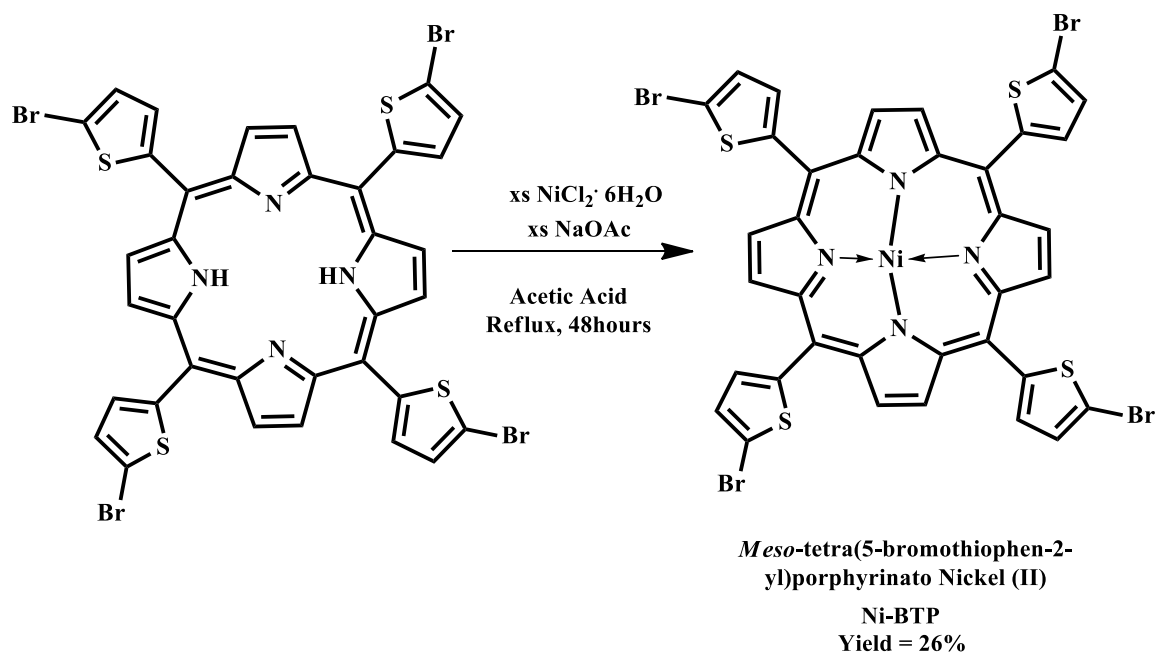
As a result, Co-BTP was isolated as a brown powder with an m/z of 1011.183, which corresponded to an empirical formula of $C_{36}H_{16}Br_4S_4Co$. The variation in the value of the molecular peak relative to BTP acted as evidence of successful metallation. The UV-Vis bands of Co-BTP were at 447 nm for its Soret band and 560 and 605.5 nm for its Q bands. The reduction of Q bands from four in the free-base (BTP) to two was also indicative of successful metallation.

4.2.8. Synthesis of *Meso*-tetra(5-bromothiophen-2-yl)porphyrinato Nickel (II) (Ni-BTP)

The synthesis of Ni-BTP was realised by metallating BTP with nickel as illustrated in



[Scheme 13.](#)



Scheme 13: Synthesis of *meso*-tetra(5-bromothiophen-2-yl)porphyrinato Nickel (II)

As a result, Ni-BTP was isolated as a red powder, whose m/z of 1012.179, corresponding to an empirical formula of $C_{36}H_{16}Br_4S_4Ni$. This value of m/z relative to that of BTP's acted as evidence of successful metallation with nickel. Ni-BTP UV-Vis bands were at 428 nm for its Soret band and 539 nm for its Q band. Both the blue-shift in the Soret band and the reduction of Q bands from four to one relative to BTP was also indicative of successful metallation.

4.3. Photo-physical Studies

Photo-physical properties relate to observable properties of a molecule due to its interaction with light. The photo-physical properties of the porphyrins that were evaluated were UV-Vis, fluorescence and infrared.

4.3.1. UV-Vis Studies

Porphyrins have a common UV-Vis spectral pattern (Conradie *et al.*, 2021). The pattern consists of two groups of peaks, the strong Soret band between 400 and 480 nm and a series of weaker peaks, Q bands from 500 to 700 nm, which were reproduced by BTP and its metal analogues as shown in [Figure 10](#).

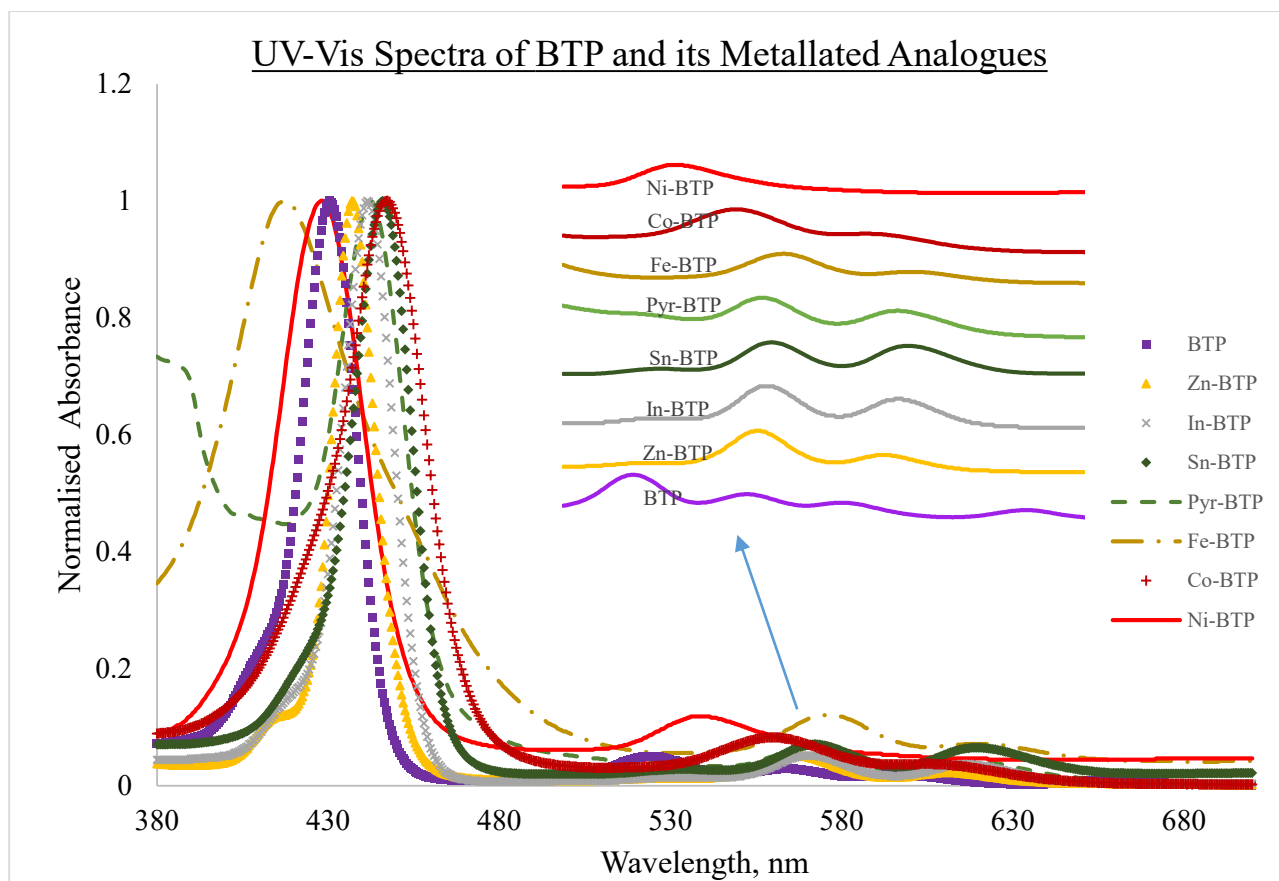


Figure 10: Over-laid UV-Vis spectra of *meso*-tetra(5-bromothiophen-2-yl)porphyrin and its metallated analogues

4.3.1.1. Soret bands

[Figure 11](#) shows the Soret band positions of the synthesised molecules on the EMS.

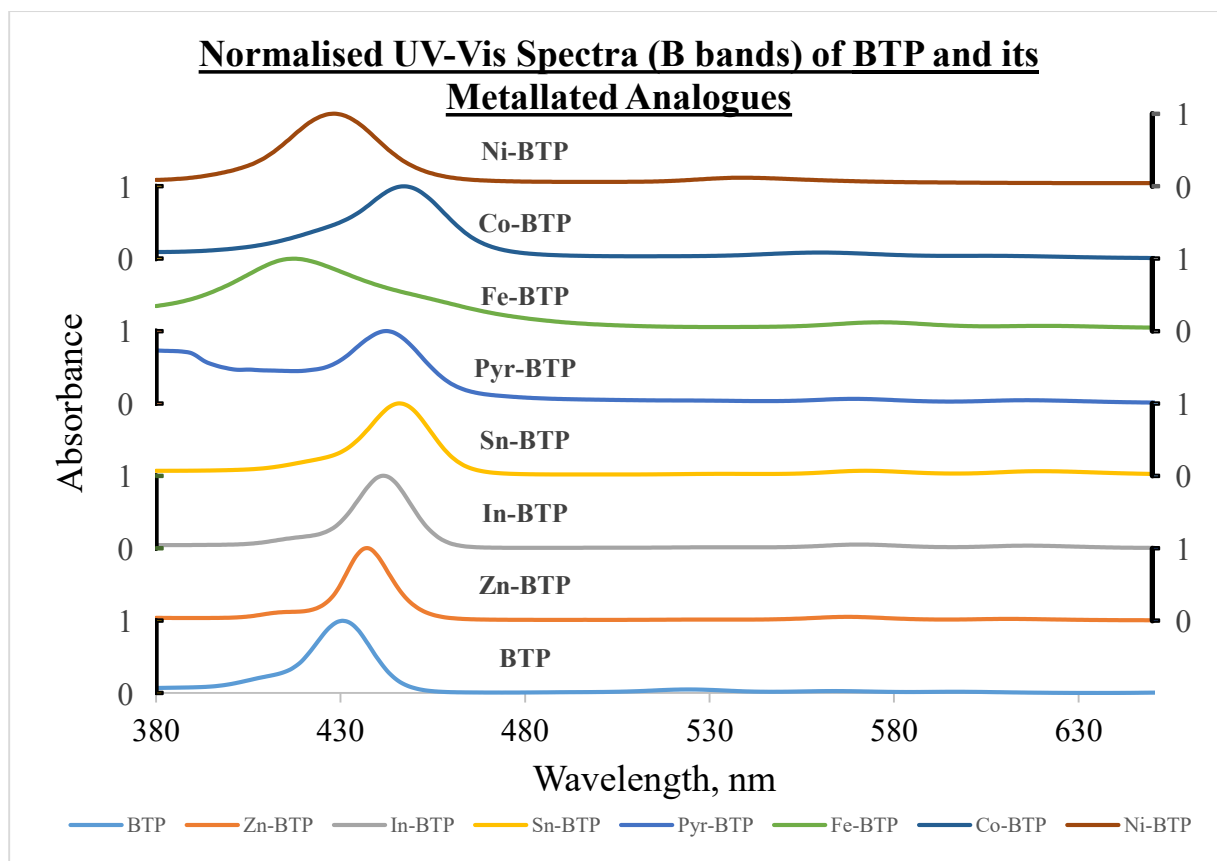


Figure 11: Overlaid Soret bands of *meso*-tetra(5-bromothiophen-2-yl)porphyrin and its metallated analogues

[Figure 12](#) also shows the Soret band positions but also contrasts BTP's Soret band with those of its metallated counterparts.

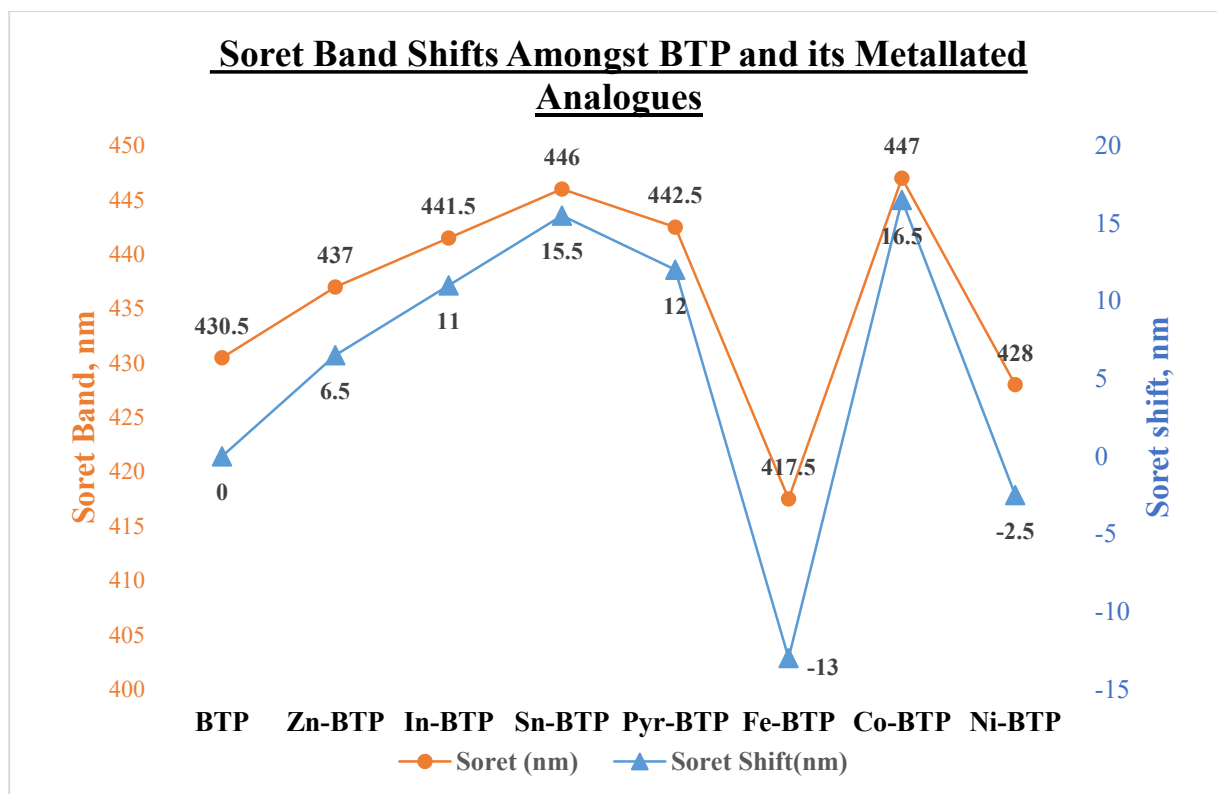


Figure 12: BTP Soret band shifts amongst *meso*-tetra(5-bromothiophen-2-yl)porphyrin and its metallated analogues

Only Fe-BTP and Ni-BTP are blue-shifted relative to BTP and all other analogues are red-shifted. Fe-BTP is the most blue-shifted, while Co-BTP is the most red-shifted followed by Sn-BTP.

Soret bands occur as a consequence of electronic transitions amongst the frontier orbitals of a porphyrin to the second excited state (S_2) (Zhang *et al.*, 2017). Frontier orbitals' responsibility in this has been illustrated by Gouterman through his four molecular orbital theory, see [Figure 13](#).

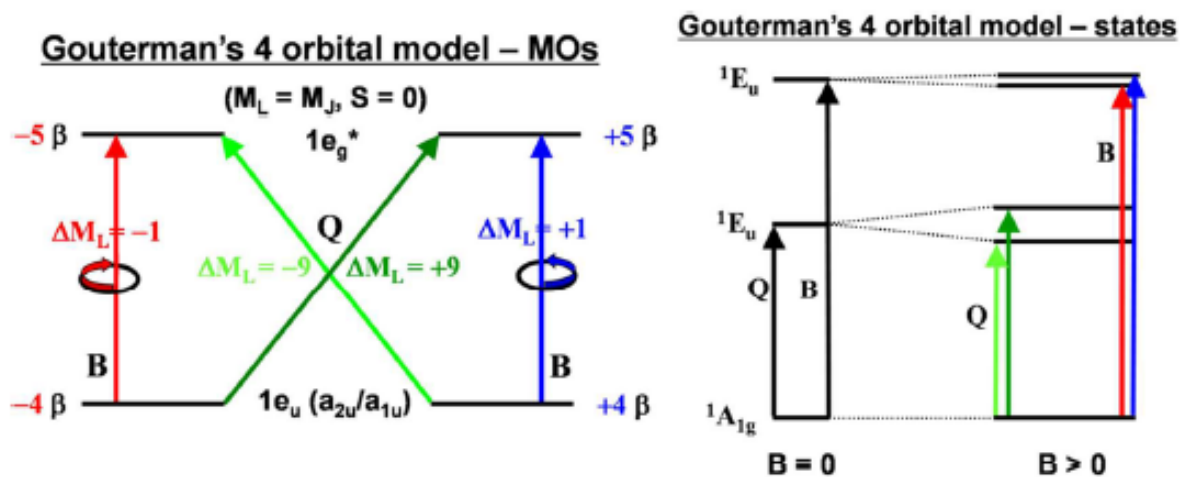


Figure 13: Gouterman's 4 orbital model (Mack, 2017)

Gouterman used an 18π aromatic metallated porphyrin to model the transitions observed in the porphyrins (Wamser and Ghosh, 2022). He calculated that for a porphyrin with D_{4h} symmetry, the HOMO orbitals (a_{1u} and a_{2u}) would be almost degenerate and the LUMO orbitals (e_g) would be degenerate as shown in [Figure 13](#) (Mack, 2017; Mack *et al.*, 2005; Wamser and Ghosh, 2022). The addition of metals to the porphyrin core or substituents on the *beta* or *meso* position can reduce the symmetry from D_{16h} (perfectly planar porphyrin) to D_{4h} , when the porphyrin is metallated and to the even lower D_{2h} , in free-base porphyrins (Oloo, 2020; Valicsek and Horváth, 2013). This would alter the position of the bands on the visible spectrum and introduce more peaks as well. More peaks would be introduced due to a break in the degeneracy of the HOMO orbitals (the e_u orbitals would now be a_{1u} and a_{2u} orbitals), hence the Soret bands and Q bands that are characteristic in identifying porphyrins (Mack, 2017). In free-base porphyrins there are usually 4 peaks due to a split in the S_1 state which is introduced due to a further reduction in symmetry (Zhang *et al.*, 2017).

The blue or red shifts observed in the metallated porphyrins could be a consequence of either; the distortion metals induce in the porphyrin or the electronic nature of the metal centre, which either reduce or increase the energy of the frontier orbitals. A more planar porphyrin would lead to a hypsochromic shift, while less planarity would lead to a bathochromic shift (Pattengale *et al.*, 2019; Sayer *et al.*, 1982; Valicsek and Horváth, 2013). The consequence of planarity on the energy levels of the Soret bands is discussed in the [Theoretical Studies](#) of this study. The

data indicated that the electronic nature of the metals played a greater role in determining the shifts in the Soret bands of the porphyrins synthesised.

Gouterman classified metallated porphyrins into three categories, hyperporphyrins, hypso-porphyrins and normal porphyrins (Wamser and Ghosh, 2022). Normal porphyrins are those with closed shell electronic configuration (d^0 and d^{10}), such as Zinc or free-base porphyrins and have spectra that obey Gouterman orbital theory. Hypso-porphyrins were those with normal spectra but were blue shifted, while hyperporphyrins were those with normal spectra but were red-shifted (Wamser and Ghosh, 2022).

The metallated analogues of BTP: Zn-BTP, In-BTP, Sn-BTP and Pyr-BTP are all red-shifted relative to the free-base, BTP. This is because of metal ligand charge transfer (MLCT) (Wamser and Ghosh, 2022) to the HOMO orbitals of the porphyrin, which leads to a decrease in the band gap amongst the frontier orbitals. This can be observed through the ^1H NMR data of the β -pyrrole's hydrogens, which are de-shielded due to an increase in the atomic size of the core metal, indicative of a stronger magnetic field. A stronger magnetic field in this context would be from increased delocalization of electrons within the porphyrin core or an increase in electron density within the aromatic ring. An increase in electron density would favour a higher wavelength for the Soret band as well as a stronger magnetic field, as evidenced by the chemical shift of β -pyrrole hydrogens of the porphyrins [Zn-BTP ($\delta 9.10$), In-BTP ($\delta 9.19$) and Sn-BTP ($\delta 9.29$)] (Arnold, 1988).

Transition metals with 6 to 9 d electrons (d^6 to d^9) usually form hypso-porphyrins. This is due to ligand to metal charge transfer (LMCT) (Wamser and Ghosh, 2022). This back-bonding results in an increase in energy difference between the HOMO and LUMO orbitals, hence the blue-shift observed (Beyene *et al.*, 2020). Back-bonding occurs between the metal's d_{xz} and d_{yz} orbitals and the LUMO orbitals (e_g). This results in the destabilisation of the LUMO orbitals and thus an increase in the energy gap between the frontier orbitals (Conradie *et al.*, 2021). For, Fe-BTP (Fe = d^6) and Ni-BTP (Ni = d^8) this was the case as they were blue-shifted. However, this documented observation did not hold for Co-BTP (Co = d^7). Implying perhaps that there exists an alternative or an additional mechanism for the hypsochromic shift observed in porphyrins metallated with d^6 - d^9 transition elements. Indeed, Conradie *et al.*, 2021 do argue for

this from their computational studies. They found that hypsochromic shifts were a consequence of electron density being donated to the porphyrin's nitrogen's 1s orbital. This resulted in the decrease in the energy level of the a_{2u} orbital which causes the energy gap between the frontier orbitals to widen (Conradie *et al.*, 2021). Modelling molecules can help in elucidating the causes of these bathochromic shifts (Zhang *et al.*, 2017).

4.3.1.2. Q bands

The Q-bands are so named after the Japanese name for the number nine, 'kyu'. From Gouterman's four orbital model. They are a result of a forbidden change in magnetic quantum number, $\Delta M_l = \pm 9$. This is juxtaposed to $\Delta M_l = \pm 1$ that causes the Soret band (Mack *et al.*, 2005). Despite being forbidden, Q bands still form due to vibrational borrowing from the B band (Zhang *et al.*, 2017). The presence of two bands for the Q bands when porphyrins are metallated is due to a split in the excited state (S_1), along the x and y axis, as a result of a reduction in the symmetry of the porphyrin. For the free-base porphyrins there is a further reduction in the symmetry of the porphyrin and this leads S_1 to be split once more leading to four Q bands (Hanna *et al.*, 2022).

In this study, the free-base porphyrin, BTP had four Q bands while all the other metallated analogues had two Q bands except Ni-BTP, which had one, as shown in [Figure 14](#) and [Figure 15](#).

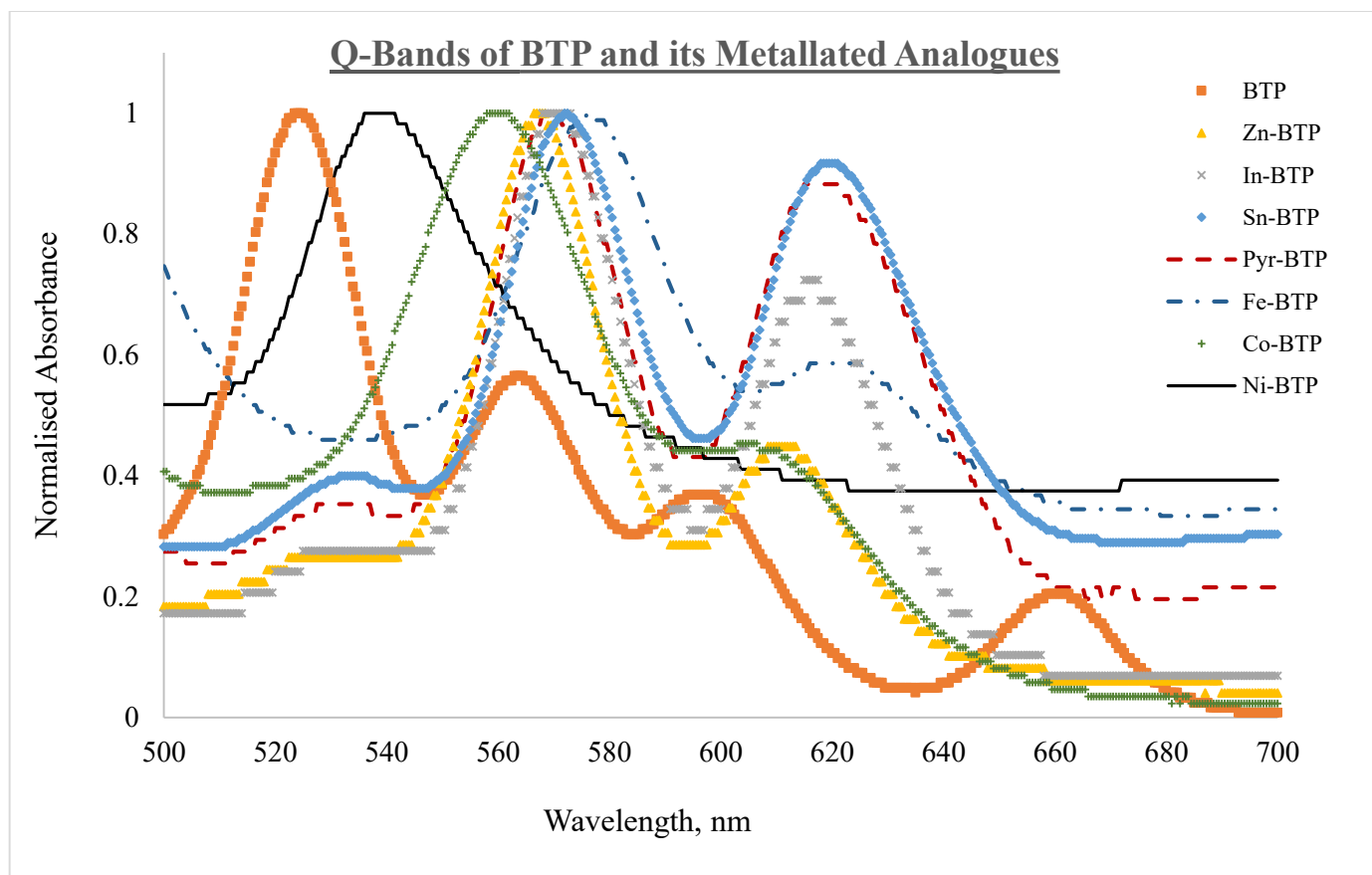


Figure 14: Q-Bands of *meso*-tetra(5-bromothiophen-2-yl)porphyrin and its metallated analogues

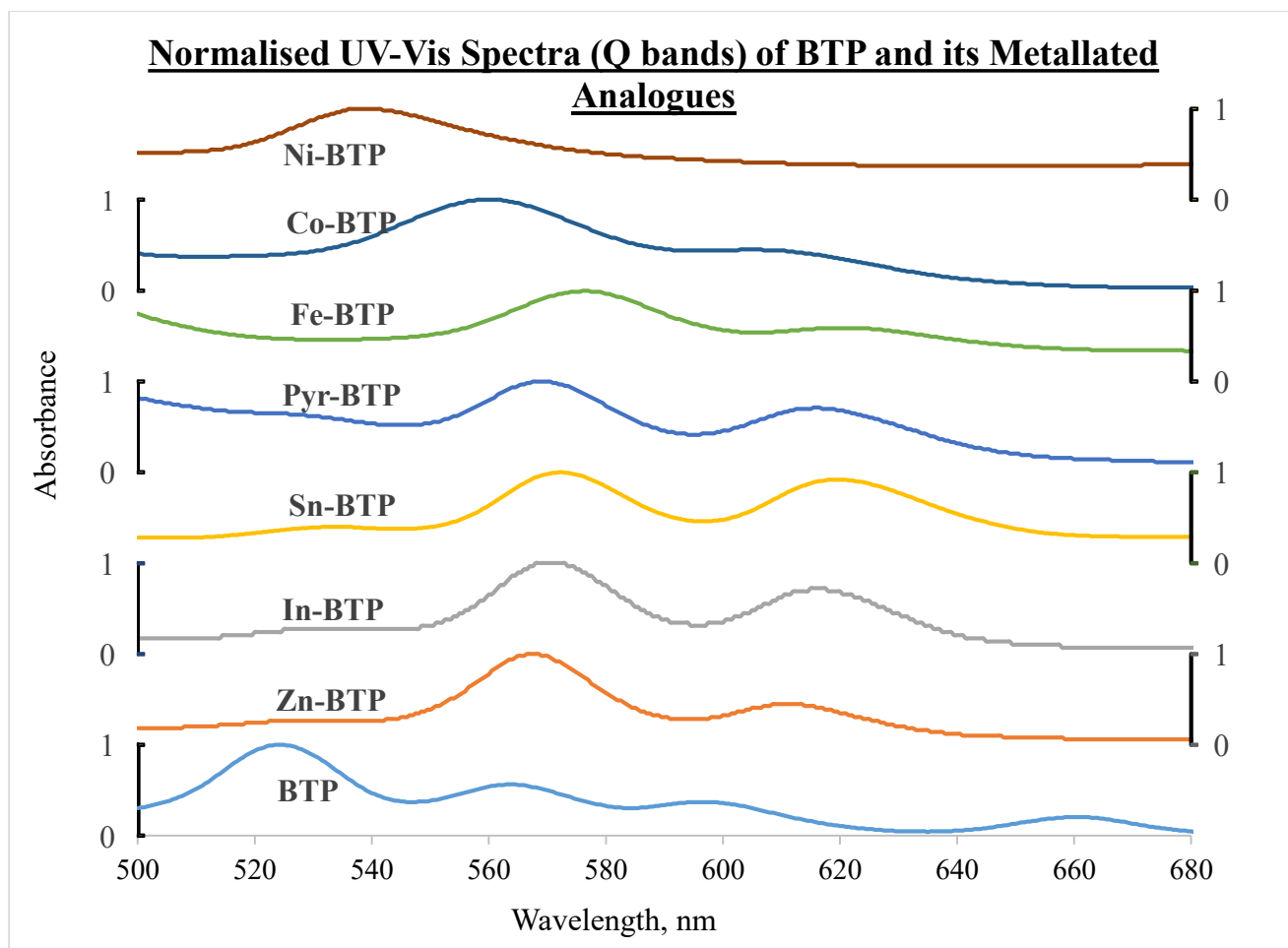


Figure 15: Overlaid UV-Vis spectra (Q bands) of *meso*-tetra(5-bromothiophen-2-yl)porphyrin and its metallated analogues

It has been noted that degeneracy could lead to reduced number of Q bands, and could be the explanation for Ni-BTP's empirical results. Increased symmetry would point to an ideal $18\text{-}\pi$ electron cyclic polyene that would have a symmetry of D_{16h} . According to Michl's calculation, at this symmetry this molecule's S_1 state has one Q band (Hanna *et al.*, 2022; Mack, 2017). One Q band for Ni-BTP means that amongst the synthesised compounds, Ni-BTP had the highest symmetry (Marsh and Mink, 1996).

4.3.1.3. Molar Absorption Coefficient

The value of the molar absorption coefficient (ϵ) gives an indication as to whether a given transition is spin-allowed or spin forbidden (Lee *et al.*, 2015; Mack *et al.*, 2007). Upon analysis of the UV-Vis spectral data of the compounds synthesised in this study, it emerged that Co-

BTP had the highest ϵ at 1,000,000 L/Mol/cm. This was just about 2.22 times greater than that of In-BTP, which had the second highest ϵ , while Sn-BTP had the least at 44,838 L/Mol/cm. This is illustrated in [Figure 16](#).

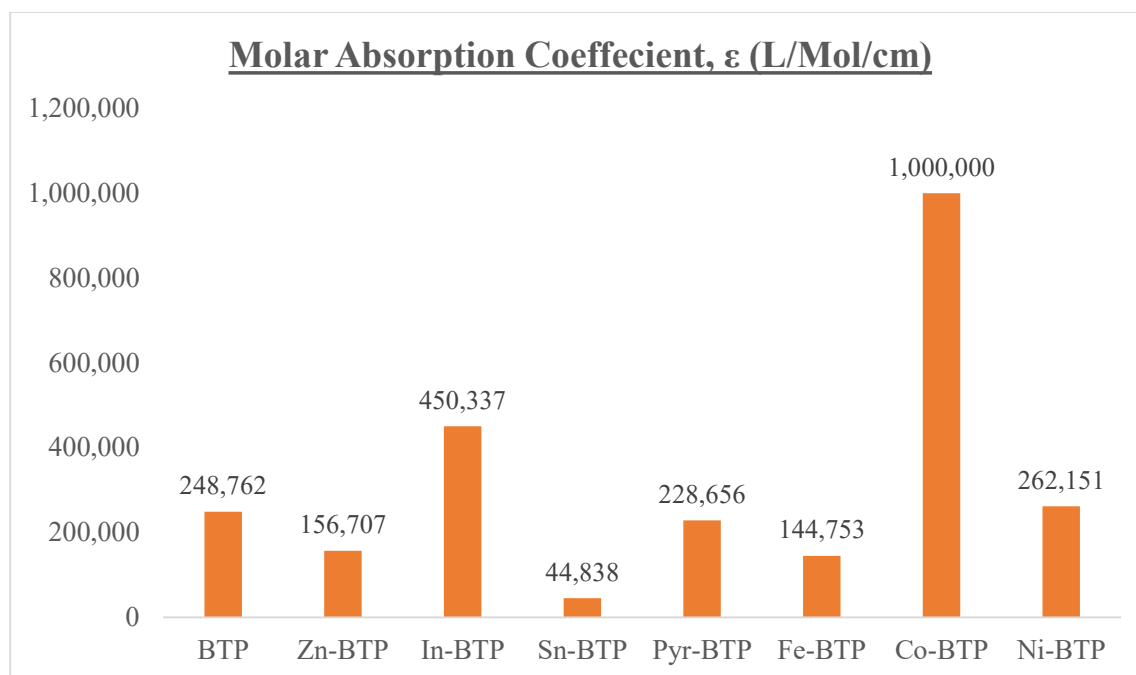


Figure 16: Molar absorption coefficient

The transition between states is also likely to be affected by whether a molecule occurs in its monomeric form or is agglomerated (Thandu *et al.*, 2015). Agglomeration reduces molar absorptivity coefficient because it introduces obstructions to the absorption of photons. This is likely to be more prevalent with Sn-BTP not only because of π - π stacking but also because of the axially ligated hydroxyl groups. The hydroxyl groups could form hydrogen bonds amongst the Sn-BTP molecules leading to a greater degree of agglomeration (Babu *et al.*, 2019). In Pyr-BTP, the hydroxyl groups of Sn-BTP have been replaced with hydroxypyridyl groups, this would reduce the degree of agglomeration due to the bulkiness of the hydroxypyridyl group thus preventing π - π stacking (Babu *et al.*, 2019). Consequently, Pyr-BTP had a ϵ of 228,656 L/Mol/cm, approximately 5 times the ϵ of Sn-BTP, as shown in [Figure 16](#).

In rationalising the ϵ based on space (volume) occupied per unit Avogadro's number of molecules per centimetre, the ϵ of Co-BTP would mean that there are 1,000,000 litres worth of Co-BTP for every mole of Co-BTP that absorb light per centimetre. But how could this work? There appears to be a force that would induce repulsion amongst Co-BTP molecules and this could explain its relatively high ϵ . This answer is based on its oscillator strength (f), derived from [Theoretical Studies](#). It is worth noting that the f values for Co-BTP do not differ greatly with those of its counterparts shown in [Figure 17](#).

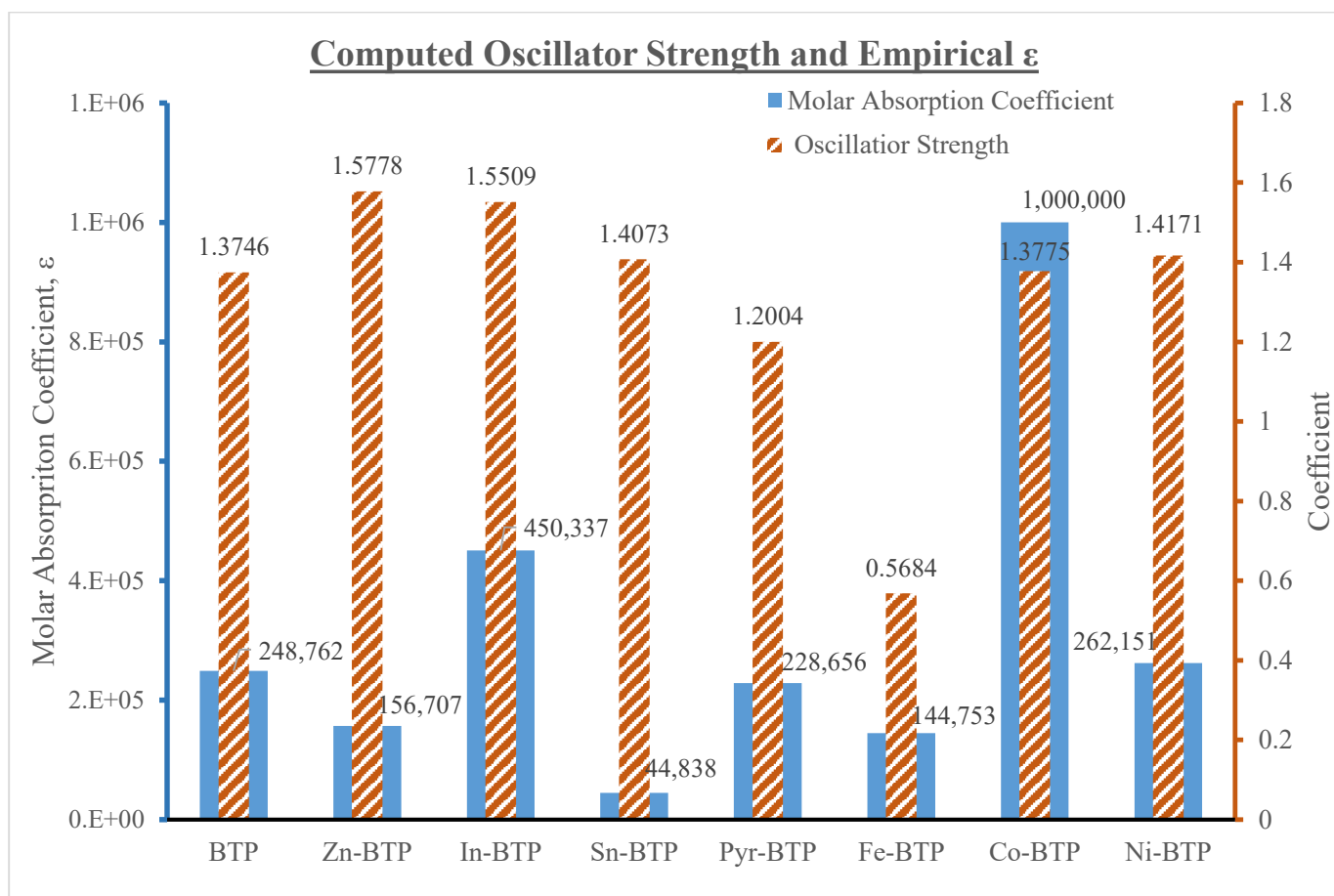


Figure 17: Computed oscillator strength and empirical ϵ

In [Figure 17](#), Co-BTP had the highest ϵ , however its f resembled all other compounds except Fe-BTP. This implies that a physical manifestation could be responsible for its high ϵ . For

instance, a physical manifestation such as agglomeration has been attributed to the low ϵ observed in Sn-BTP relative to that of Pyr-BTP as their f are very similar (Babu *et al.*, 2019).

4.3.2. *Fluorescence Spectroscopy*

Fluorescence spectroscopy is a measure of the wavelength at which a molecule emits photons after initially absorbing photons. The photons emitted are usually of lower energy than those absorbed due to the principle of conservation of energy. The pattern of the fluorescence spectra can be used to establish whether a molecule maintained its geometric and orbital organisation in its excited state (Wardle, 2009). This is determined when it appears that the absorption and emission spectra are mirror images of each other. In the case of BTP and its metallated analogues, this was the case when both spectra were normalised, as shown in [Figure 18](#).

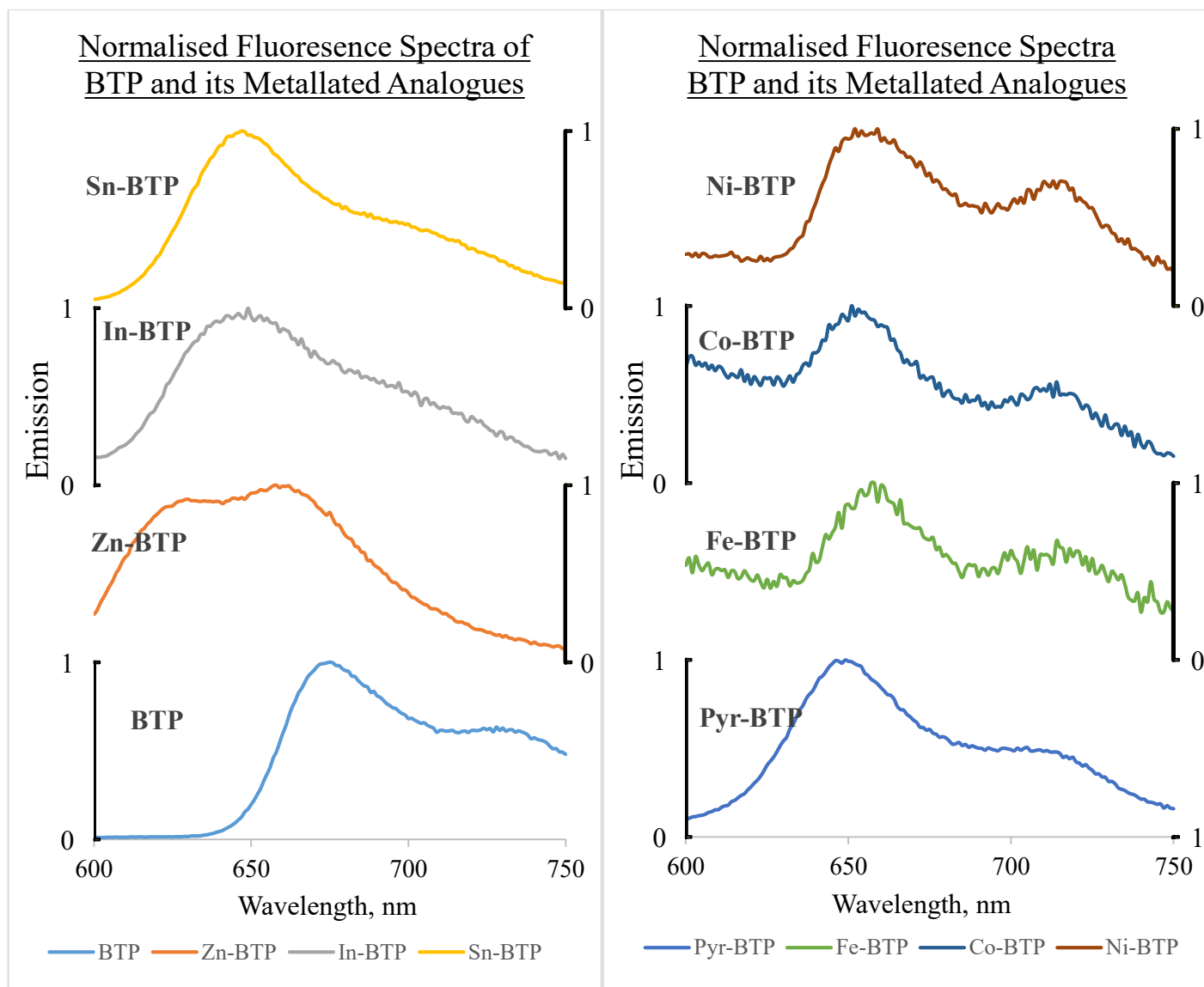


Figure 18: Normalised fluorescence spectra of *meso*-tetra(5-bromothiophen-2-yl)porphyrin and its metallated analogues

The mirrored images of the UV-Vis spectra and fluorescence spectra can be found in [Appendix 3](#). These mirrored spectra are indicative of the photo-stability of the synthesised compounds in their excited state. Thus as photosensitisers in water disinfection they would neither take up more reactive forms nor generate other artefacts while in use.

4.3.2.1. Fluorescence quantum yield

Fluorescence quantum yield (Φ_f) is a relative measure of the photons fluoresced by the molecule to those that are absorbed. It is in direct competition with inter-system crossing (ISC).

A low Φ_f translates to more electrons being available for ISC (high ISC), which in turn increases the probability of formation of singlet oxygen (Khisa, 2020). In this study, it was observed that the Φ_f of BTP and its metal analogues were lower than the standard *meso*-tetra(phenyl)pophyrinato zinc(II) (Zn-TPP) at 3.3E-02, as shown in [Figure 19](#). This low Φ_f is largely attributed to the heavy atom effect, induced by the bromine atoms on the thiophenyl substituents. Heavy atom effect leads to spin-orbit coupling, which encourages ISC (Fushimi *et al.*, 2017; Wardle, 2009)

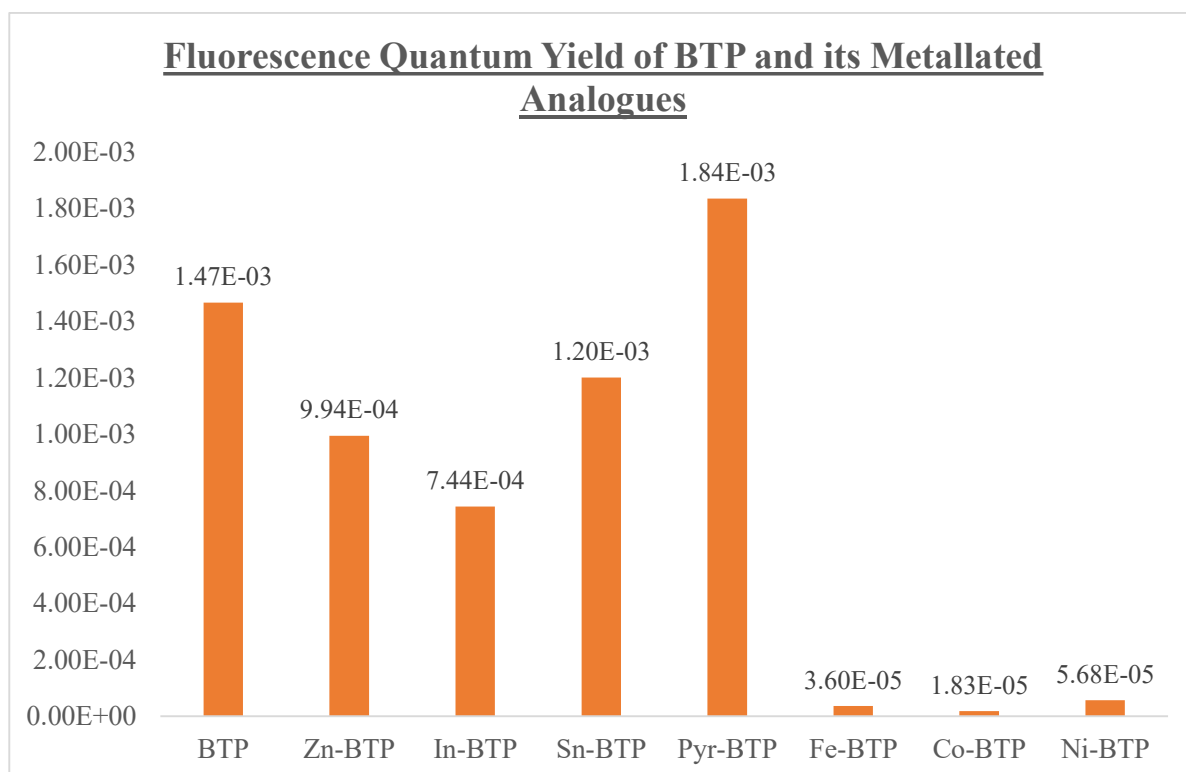


Figure 19: Fluorescence quantum yield of *meso*-tetra(5-bromothiophen-2-yl)porphyrin and its metallated analogues

With regard to heavy atom effect, it would be expected that the order of decreasing Φ_f would have been: Fe-BTP, Co-BTP, Ni-BTP, Zn-BTP, In-BTP, Sn-BTP and finally Pyr-BTP. However, from the observations in this study, the converse is true with the transition metal analogues (Co, Fe and Ni) having the lowest Φ_f . The low Φ_f amongst the transition metal derivatives (Fe, Co and Ni) is attributed to the d_π and π^* back-bonding between the metal's

orbitals and the porphyrin ligand's orbitals as well as the heavy atom effect (Marsh and Mink, 1996). The former explanation falls within El-Sayed's selection rule. El-Sayed's selection rule states that a change in orbital type will facilitate a faster rate of intersystem crossing, from the lowest excited singlet state to the triplet manifold (Figure 20), back-bonding would have an effect on the orbital type (Wardle, 2009).

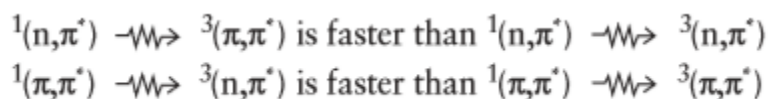


Figure 20: Illustration of El-Sayed's selection rule (Wardle, 2009)

In this study, Zn-BTP and In-BTP behaved as expected, this is based on the fact that Indium (In) is heavier than zinc (Zn) and thus indium (In) would have a comparatively larger heavy atom effect than Zn. However, for Sn-BTP and Pyr BTP, it was observed that Sn-BTP had a higher Φ_f than In-BTP despite the former having a greater atomic mass. Furthermore, Pyr-BTP had the greatest Φ_f even more so than the free-base. It is also worth noting that electron-donating groups cause an increase in fluorescence (Wardle, 2009). In this regard, Pyr-BTP and Sn-BTP have electron donating groups as substituents (oxypyridyl and hydroxyl groups, respectively) that appear to counteract the heavy atom effect for tin. It also implies that the oxypyridyl group is a stronger electron donor than the hydroxyl group.

4.3.2.2. *Stoke's shift*

Stoke's shift is a measure of the difference between the wavelength of the absorption band and the emission band (Zhang *et al.*, 2017). Stoke's shift can be used to determine whether a molecule will generate photons that would lead to self-excitation (Destruel *et al.*, 1989; Zhu *et al.*, 2017). The ability to self-excite would enhance the production of singlet oxygen for every electron that is excited in the PS. In this study, Ni-BTP had the highest Stoke's shift of the synthesised molecules, this is on account of its solitary Q-band, as shown in Figure 21.

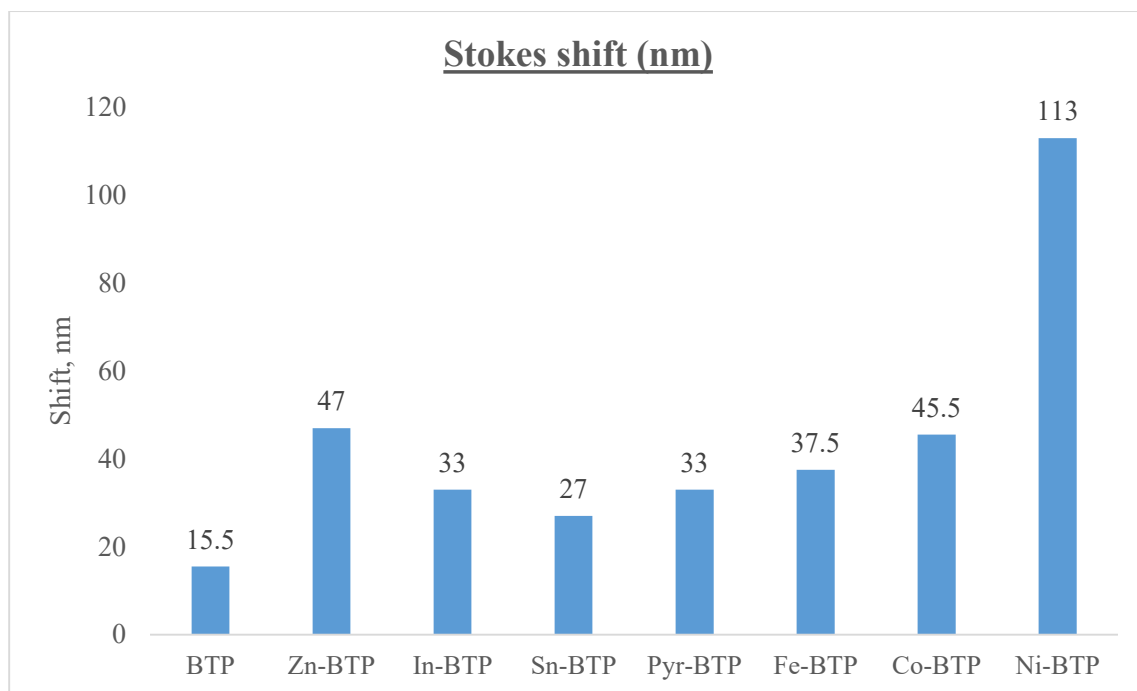


Figure 21: Stoke's shift

In this case, self-excitation of the synthesised porphyrins is possible as the Q-bands are in close proximity to the emitted bands (BTP has a proximity of 15.5 nm). However, given the observed low Φ_f yields, this is unlikely to be a significant factor in the excitation of BTP and its metallated derivatives for applications in photodynamic water disinfection.

4.4. Theoretical Studies

Theoretical studies were conducted in line with the third objective of the study. This was to explain the variations in the empirical UV-Vis spectroscopic properties of the porphyrins. The molecules were modelled using density functional theory (DFT) through theoretical models, B3LYP and CAM-B3LYP. Although, from previous studies, both CAM-B3LYP and B3LYP had been shown to have good predictive powers when modelling porphyrins, CAM-B3LYP is the superior of the two (Goerigk and Mehta, 2019; Oyim *et al.*, 2022). To mimic solvent conditions, the polarizable continuum model (PCM) was used with the compounds being modelled in solvent conditions (DMSO) and vacuum conditions.

In order to identify the appropriate model to explain the photo-physical properties observed, the model generated soret bands and soret shifts were compared with empirical ones, as shown in [Figure 22](#).

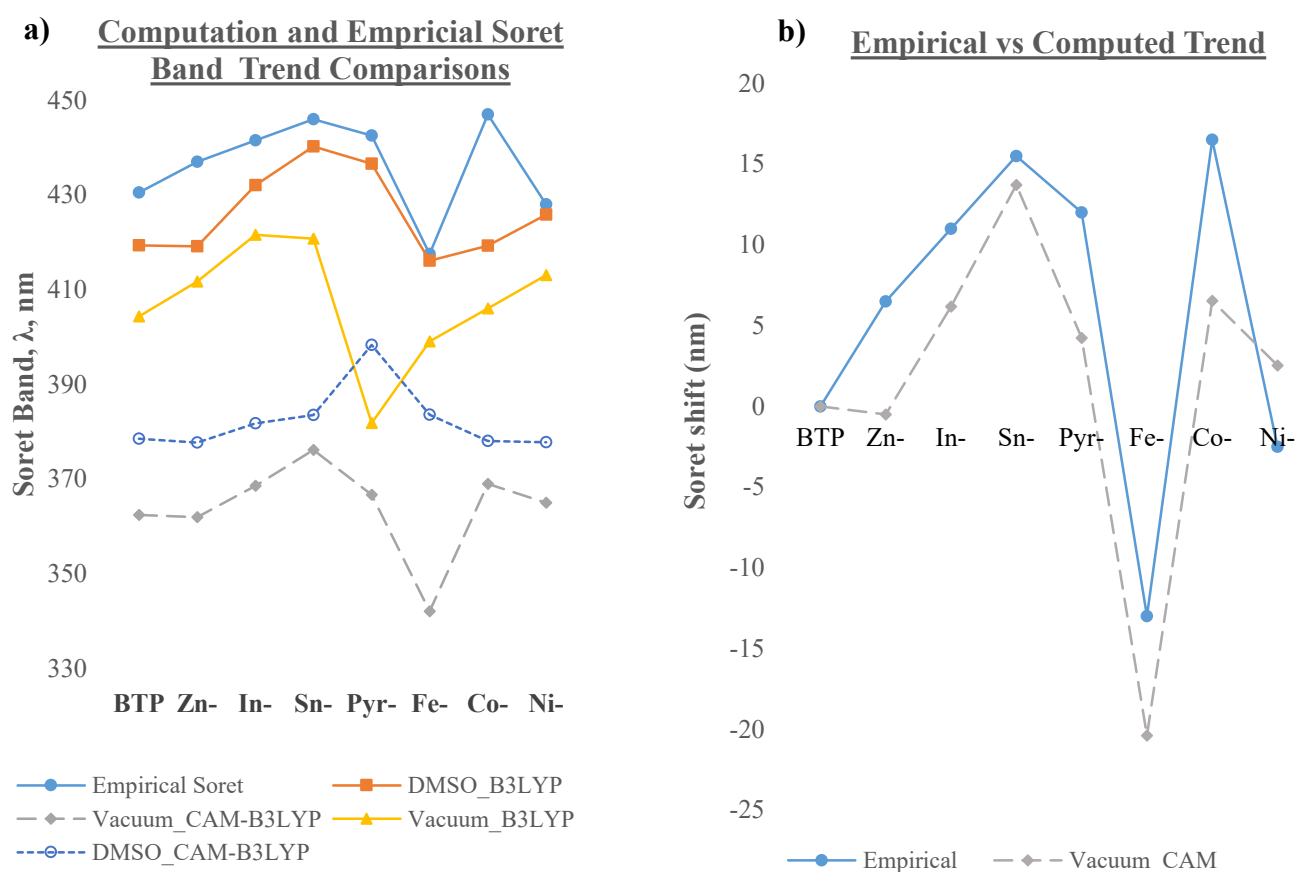


Figure 22: Comparison of computed and empirical UV-Vis spectra

a) Computational's and empirical's Soret band trend comparison b) Empirical's vs vacuum CAM-B3LYP' Soret band comparison

Upon comparison of the models and empirical data, CAM-B3LYP in vacuum had a trend that had close semblance to the empirical data with the highest coefficient of determination ($r^2 = 0.7719$) relative to the empirical data. It was thus the model chosen to simulate the properties of the synthesised porphyrins. Although DMSO-B3LYP also had a similar trend, it was disqualified on account of a lower r^2 value of 0.3447.

4.4.1. Optimised Geometry

The functional, CAM-B3LYP was used to compute the minimum energy of the synthesised molecules. This was done by altering the geometry of the molecule with a view to minimising its energy in order to optimise its geometry. An output file that contains the coordinates of the atoms gives a virtual image of the molecule. The output files contain the energy levels of the orbitals of the synthesised molecules. For BTP and its metallated analogues the thiophenyl group was mostly perpendicular to the porphyrin core which is what was expected for thiophenyl groups, this can be seen for Zn-BTP in [Figure 23](#) and [Appendix 5](#) for the remaining molecules.

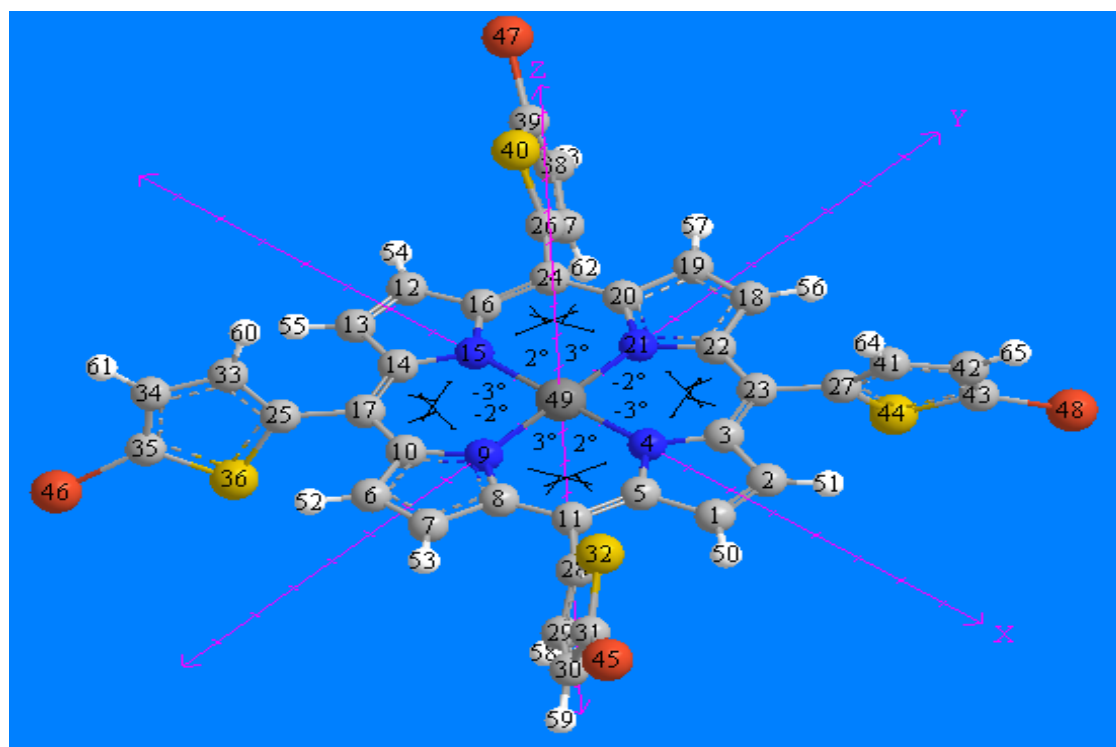


Figure 23: *Meso*-tetra(5-bromothiophen-2-yl)porphyrinato Zinc (II) showing atom labels referenced in dihedral angle table

This is mostly due to steric hindrance occasioned by the size of the sulphur molecule. The modelling matched the predictions of Ghosh *et al.*, (2010).

4.4.1.1. Distortion of Geometry

Distortion in the porphyrin core is measured based on the dihedral angle $C_{\alpha}-C_{meso}-C_{meso}-N$ angles as shown in [Table 2](#) (Valicsek and Horváth, 2013).

Table 2: Dihedral angles showing distortion in synthesised porphyrins

| Molecule | C(3)-C(23)- C(22)-N(21) | C(22)-C(23)- C(3)-N(4) | C(5)-C(11)- C(8)-N(9) | C(10)-C(17)- C(14)-N(15) | C(16)-C(24)- C(20)-N(21) | C(8)-C(11)- C(5)-N(4) | C(14)-C(17)- C(10)-N(9) | C(20)-C(24)- C(16)-N(15) |
|----------------|----------------------------|---------------------------|--------------------------|-----------------------------|-----------------------------|--------------------------|----------------------------|-----------------------------|
| BTP | 3.1 | 3.1 | -2.4 | 3.1 | -2.4 | -3.8 | 3.1 | -3.8 |
| Zn-BTP | -2.7 | -1.8 | 1.8 | -1.8 | 1.8 | 2.7 | -2.7 | 2.7 |
| In-BTP | 1.6 | -2.8 | -0.9 | -2.4 | -1.8 | 3.0 | 1.8 | 1.8 |
| Sn-BTP | -3.5 | -3.5 | 1.5 | -0.9 | 2.5 | 2.6 | -0.3 | 1.6 |
| Pyr-BTP | 1.1 | -2.0 | 3.2 | -2.2 | 1.1 | -2.2 | 3.2 | -2.0 |
| Fe-BTP | 2.3 | -7.6 | 8.0 | -7.6 | 8.0 | -3.0 | 2.3 | -3.0 |
| Co-BTP | -11.7 | 4.7 | -4.8 | 5.0 | -4.7 | 11.8 | -11.8 | 11.6 |
| Ni-BTP | 5.3 | -12.0 | 12.0 | -11.6 | 12.0 | -5.2 | 5.2 | -5.5 |

The BTP analogues metalated with transition elements were more distorted than their non-transition element counter-parts except for Zn-BTP. The non-linearity of the effects of ring distortion on Soret band shifts relative to the free-base (BTP) was observed in the optimised geometries of the molecule. Where a hypsochromic shift was expected for a planar molecule, a bathochromic shift was observed as in Sn-BTP (Sn-BTP is relatively planar) and vice-versa for Fe-BTP (Fe-BTP was more distorted). The comparison amongst the Soret band bears significance because empirically distortion has been confirmed as a contributing factor in Soret band shifts in porphyrins (Pattengale *et al.*, 2019).

This means that these distortions affect the positions of HOMO and LUMO. For in-plane porphyrins, blue-shifts are a consequence of metal charge transfer between the metal and the porphyrin ring. This causes a reduction in the energy level of the HOMO orbitals and consequently a blue-shift in the porphyrin's Soret bands (Valicsek and Horváth, 2013). The definition of in-plane porphyrin is one whose metal centre is planar to the porphyrin core. However, given the results arrived at from the calculations whereby Fe-BTP was geometrically optimised but was observed to be more distorted relative to the other metal analogues of BTP and BTP itself, the resultant blue-shift can only be attributed to metal charge transfer between the metal and the porphine ring with minimal regard to distortion.

The dominance of the electronic nature of the metals on the optical properties can be viewed by contrasting the geometries calculated with the UV-Vis data where hyperporphyrins are more planar than their hypsoporphyrins counterparts as shown in [Table 2](#).

4.4.1.2. Frontier Orbitals

Orbitals represent points in a molecule where electrons have the highest probability of being found. Frontier orbitals refer to the highest occupied orbitals and the lowest unoccupied orbitals in a compound. They are the orbitals between which excited and relaxing electrons transition. For BTP and its metal analogues, the energy levels of their orbitals as well as Gouterman's four orbitals are captured in the output files shown in [Figure 24](#). The 'a' and 's' notations used in [Figure 24](#) serve to distinguish between orbitals which have a node running through their y-axis and those that do not. Those that have a node are denoted as 'a' while those that have an anti-node are denoted as 's', to differentiate the HOMO orbitals from the LUMO orbitals, LUMO orbitals' notations have a negative sign (-a and -s) (Mack, 2017; Oyim *et al.*, 2022).

-

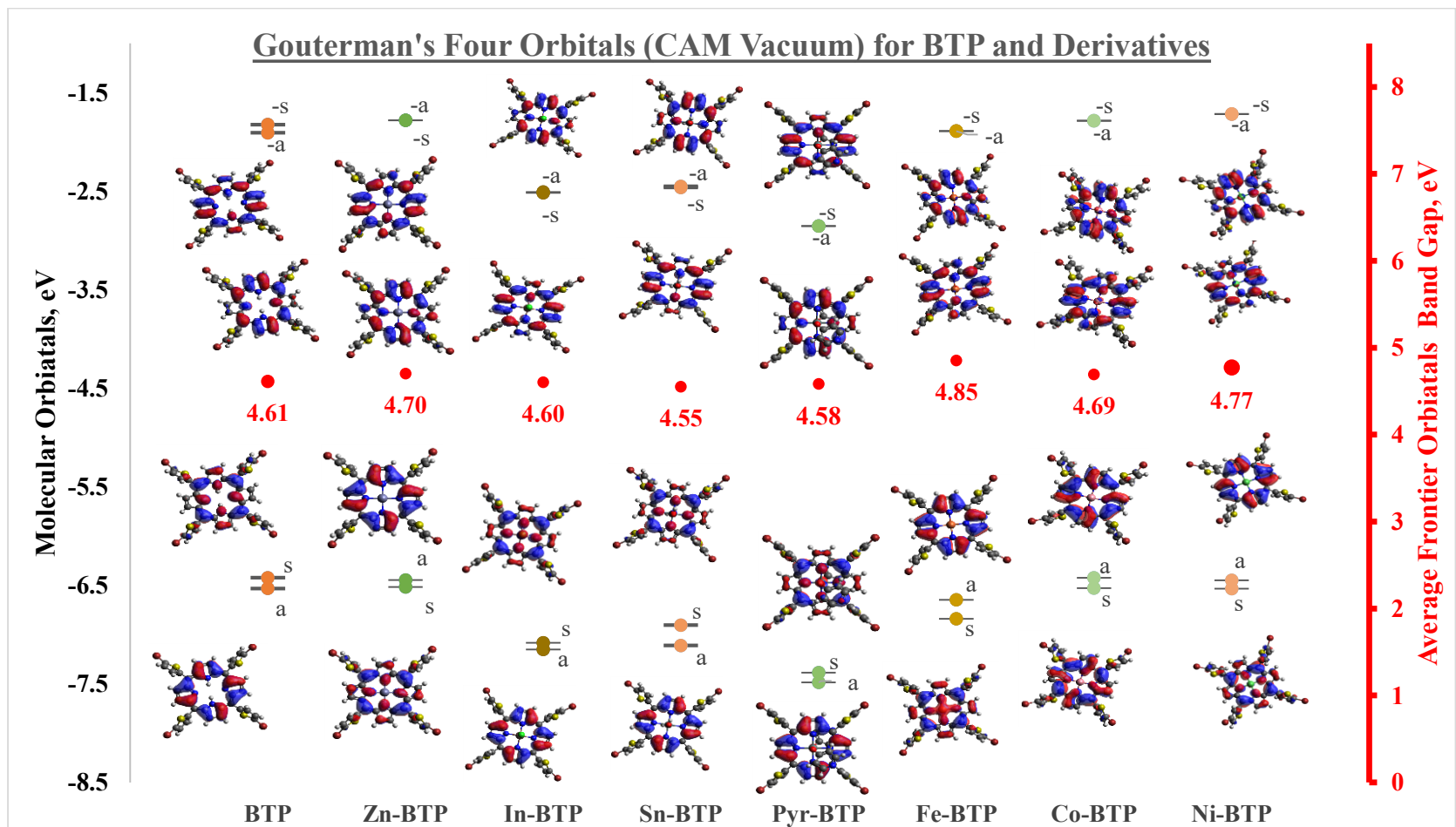


Figure 24: Gouterman's four molecular orbitals (CAM_Vacuum) for *meso*-tetra(5-bromothiophen-2-yl)porphyrin and its metal analogues

From [Figure 24](#), it is possible to observe the effect that addition of the metals had on the frontier orbitals of the porphyrin, in terms of energy level. Porphyrins and their metal derivatives are classified as normal porphyrins, when they have their distinct UV-Vis spectral pattern as in closed d-shell metals such as in Zinc (d^{10}) or in their free-base form and as hypso-porphyrins when they are blue-shifted relative to normal porphyrins such as in d^6 - d^9 transition element porphyrin derivatives. They are also classified as hyperporphyrins when, they are red-shifted relative to normal porphyrins such as in d^1 - d^5 or as metalloid porphyrin derivatives (Ghosh and Conradie, 2021). This latter distinction between the metalloids and the transition metals and their effect on the frontier orbitals is apparent in [Figure 24](#).

4.4.1.2.1. Metalloid Elements

The metalloids employed in this study are Indium and Tin, represented by In-BTP, Sn-BTP and Pyr-BTP. In all cases, relative to the normal porphyrins their HOMO positions have decreased further (in descending order, that is Sn-BTP, In-BTP and finally Pyr-BTP), as shown in [Figure 24](#). This agrees with the prevalent theory that hyperporphyrins are a consequence of metal ligand charge transfer (MLCT), which results in a lowering of the HOMO orbitals and subsequent decrease in HOMO-LUMO gap (Wamser and Ghosh, 2022).

4.4.1.2.2. Transition Elements

The transition elements that were employed in this study are: iron, cobalt, nickel and zinc through their corresponding metal-complexes: Fe-BTP, Co-BTP, Ni-BTP and Zn-BTP. From [Figure 24](#) it is apparent that relative to BTP, all transition element analogues of BTP were predicted to have larger band-gaps with Fe-BTP having the greatest band-gap and Co-BTP having the least. The relative average energy changes of the orbitals are illustrated in [Figure 24](#). In this case, only Co-BTP's HOMO orbitals were elevated in energy relative to BTP, while all the other transition metal HOMO orbital energies' decreased. As for the LUMO orbitals, only Fe-BTP LUMO orbitals' decreased while all other transition metal LUMO orbitals' increased in energy. The standard reason given for blue-shifts in hypso-porphyrins of transition elements is that the LUMO orbitals interact with the $d\pi$ orbitals of the metals. This stabilises the $d\pi$ orbitals but causes a subsequent de-stabilisation of the LUMO orbitals causing an increase in energy, in other words ligand metal charge transfer (LMCT) (Wamser and Ghosh, 2022). While this could explain the variation in energy for Co-BTP and Ni-BTP, it does not explain the variation in energy for Fe-BTP. Fortunately Ghosh and Conradie, (2021) did a

theoretical study to establish the cause for hypsochromic shifts in transition element porphyrins, in an article entitled ‘The Dog that did not Bark’. They were also surprised to find that the cause was not LMCT (they based this on the finding that the LUMO orbitals of the Zinc porphyrin remained constant irrespective of the transition elements substituted for it, namely palladium and platinum) but rather a withholding of electron density by the transition elements (Ghosh and Conradie, 2021). Mulliken charges were used to establish the degree of electron-negativity with the more blue-shifted element having a greater Mulliken charge relative to their red-shifted counterparts at greater than 1 for the former and less than 1 for the latter (Ghosh and Conradie, 2021). The same was observed amongst the transition element analogues for BTP, as shown in [Table 3](#). That being said, based on the results of this modelling, it appears that both LMCT (for Ni-BTP) and electron density denial (for Fe-BTP) could be used to explain hypsochromic shifts in transition element porphyrins.

Table 3: Mulliken charges of transition elements

| Mulliken Charges | | | |
|-------------------------|---------------|---------------|---------------|
| Fe-BTP | Co-BTP | Ni-BTP | Zn-BTP |
| 1.110404 | 0.91104 | 0.781073 | 0.939455 |

4.4.2. Time Dependent –Density Functional Theory Studies

Time dependent-density functional theory (TD-DFT) enables chemists to simulate UV-Vis spectra of molecules as well as the oscillator strength (f) of various transitions. This conforms with the Gouterman’s theory by showing the orbitals responsible for a particular transition (Conradie *et al.*, 2021).

These simulations provide an opportunity to observe what would happen to an individual molecule when it is excited. This is especially relevant when trying to determine the potential of a molecule for a particular application (Conradie *et al.*, 2021; Oyim *et al.*, 2022). This is illustrated in this study through comparison of the empirical and calculated results of Sn-BTP. Sn-BTP had a ϵ of 44,836L/Mol/cm but is shown to have an oscillator strength (f) of 1.4073, as shown in [Figure 25](#).

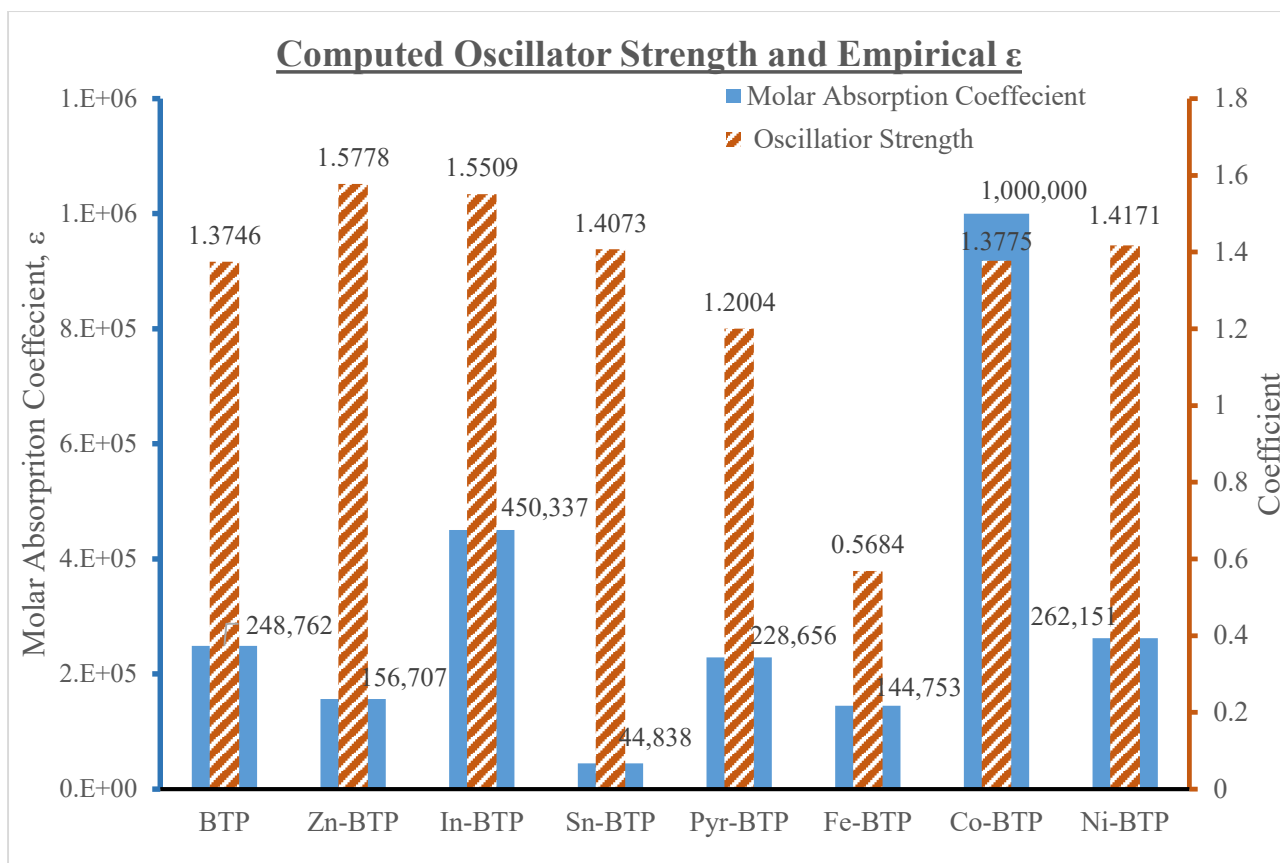


Figure 25: Computed oscillator strength and empirical ϵ

This f value of Sn-BTP is similar to those observed with all other BTP molecules except for Fe-BTP which had an f value of 0.5684. It was thus concluded that the reduction in ϵ for Sn-BTP was due to hydrogen bonding. The same applies for Co-BTP, where empirically it had a ϵ of 1,000,000L/Mol/cm, but upon interrogation of its computed oscillator strength (f), 1.3475 it was found to lie alongside most other metallated BTPs. In conclusion it could be inferred that a factor such as repulsion may play a role in the high ϵ of Co-BTP.

TD-DFT calculations also showed that for all the synthesised porphyrins, the Soret band and Q-band transitions were a consequence of excitation of electrons amongst the frontier orbitals as shown in [Table 4](#) for BTP, while BTP's metal analogues are shown in [Appendix 7](#).

Table 4: Computed photo-physical properties of *meso*-tetra(5-bromothiophen-2-yl)porphyrin

| Molecule | Band | State | f, oscillator strength | Calculated | | Empirical | | Wavefunction | | Probability (%) |
|------------|------|--------|------------------------------|------------|------------------|-----------|------------------|--------------|----------|-----------------|
| | | | | nm | cm ⁻¹ | nm | cm ⁻¹ | HOMO(□) | -LUMO(□) | |
| BTP | Q | 1 | 0.0018 | 589.1 | 16,975.05 | 660.5 | 15,140.05 | a(-1) | a | 45 |
| | | | | | | 596.5 | 16,764.46 | s | s(+1) | 52 |
| | Q | 2 | 0.0252 | 537.47 | 18,605.69 | 563 | 17,761.99 | a(-1) | s(+1) | 43 |
| | | | | | | 524 | 19,083.97 | s | a | 54 |
| | B | 3 | 1.3746 | 372.86 | 26,819.72 | | | a(-1) | a | 48 |
| | | | | | | | | a(-1) | s(+1) | 2 |
| | | | | | | | | s(-1) | s(+1) | 38 |
| | | | | | | 430.5 | 23,228.80 | a(-1) | a | 2 |
| | | | | | | | | a(-1) | s(+1) | 53 |
| | | | | | | | | s | a | 43 |
| B | 4 | 1.7717 | 362.39 | 27,594.58 | | | s | s(+1) | 2 | |

This further conforms to the Gouterman's four orbital theory, where he determined that only the frontier orbitals would be responsible for these transitions. This is because the remaining orbitals were energetically too far from the frontier orbitals (Conradie *et al.*, 2021).

4.5. Antimicrobial Studies

Antimicrobial studies were conducted using broth micro-dilution technique. This method involved testing the antimicrobial activity of a compound at varying concentrations against bacteria in a 96-well plate (Balouiri *et al.*, 2016). Carbapenem resistant *E. coli* (*CRE.coli*) and methicillin resistant *Staphylococcus aureus* (MRSA) were exposed to BTP and three of its metal analogues (Zn-BTP, In-BTP and Fe-BTP). The concentrations chosen were: 20µM, 40µM, 60µM, 80µM and 100µM. In order to ascertain the role of light in antimicrobial activity, the bacteria were assayed in light and dark conditions. The resultant survival rate of the bacteria was then determined by comparing the absorbance of bacteria that had survived exposure relative to those that were not exposed to the antimicrobial, via [Equation \(4\)](#).

$$\text{Antimicrobial activity} = \frac{\Delta \text{ Average Abs(sample)}}{\Delta \text{ Average Abs(Control)}} \times 100 \dots\dots\dots \text{Equation (4)}$$

Key: Abs= Absorbance, Δ= Change

The two species of bacteria assayed are representative of two categories of bacteria namely, gram-positive (MRSA) and gram negative (*CRE.coli*) bacteria. Note that gram-positive and gram-negative bacteria are differentiated based on the ability of their membranes to be stained by crystal violet (gram-positive can be stained while gram-negative bacteria cannot) (Khisa, 2020). This points to a difference in the morphology of their membranes. In gram-positive bacteria, their membrane is composed of 70% by dry weight peptidoglycan and is the reason why it stains in the presence of crystal violet. While, gram-negative bacteria membranes are composed of less than 10% by dry-weight of peptidoglycan, which does not stain, however they do have a more complex membrane. (Hogg, 2013)

4.5.1. Methicillin Resistant *Staphylococcus aureus*

To demonstrate the role of light in the antimicrobial activity of BTP and its metal analogues against methicillin resistant *Staphylococcus aureus* (MRSA), their activity was compared under light and dark conditions. The results are summarised in [Figure 26](#).

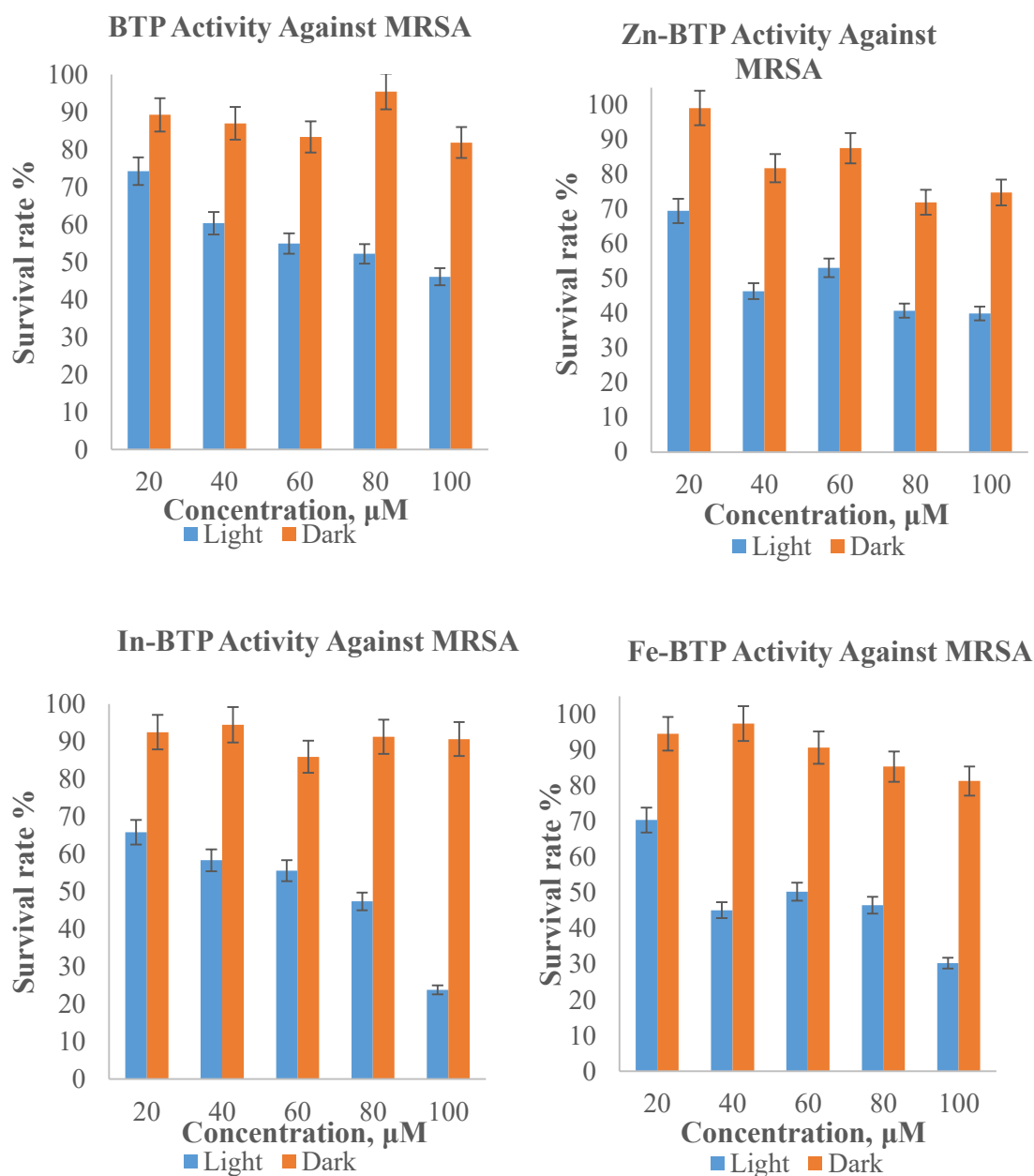


Figure 26: Antimicrobial activity of *meso*-tetra(5-bromothiophen-2-yl)porphyrin (BTP) and metal analogues against Methicillin Resistant *Staphylococcus aureus*

The survival rate of MRSA in dark conditions was higher than those in light conditions, demonstrating the necessity of light in photosensitising BTP and its metal analogues for potential application in photodynamic water disinfection. This was further supported by analysis of variance (ANOVA) one-factor tests, which showed a significant difference between the two conditions as shown in [Table 5](#).

Table 5: Significance tests for light against dark conditions- methicillin resistant *Staphylococcus aureus*

| MRSA ANOVA-One Factor | | |
|------------------------------|----------|-------------------|
| Compound | F | F critical |
| BTP | 10.7006 | 5.3177 |
| Zn-BTP | 21.5859 | 5.3177 |
| In-BTP | 30.9690 | 5.3177 |
| Fe-BTP | 34.4185 | 5.3177 |

The concentration-dependent antibacterial activity of BTP and its metal analogues and their respective 50% minimum inhibitory concentration (IC₅₀) against MRSA under light conditions are summarised in [Figure 27](#) and [Table 6](#), respectively.

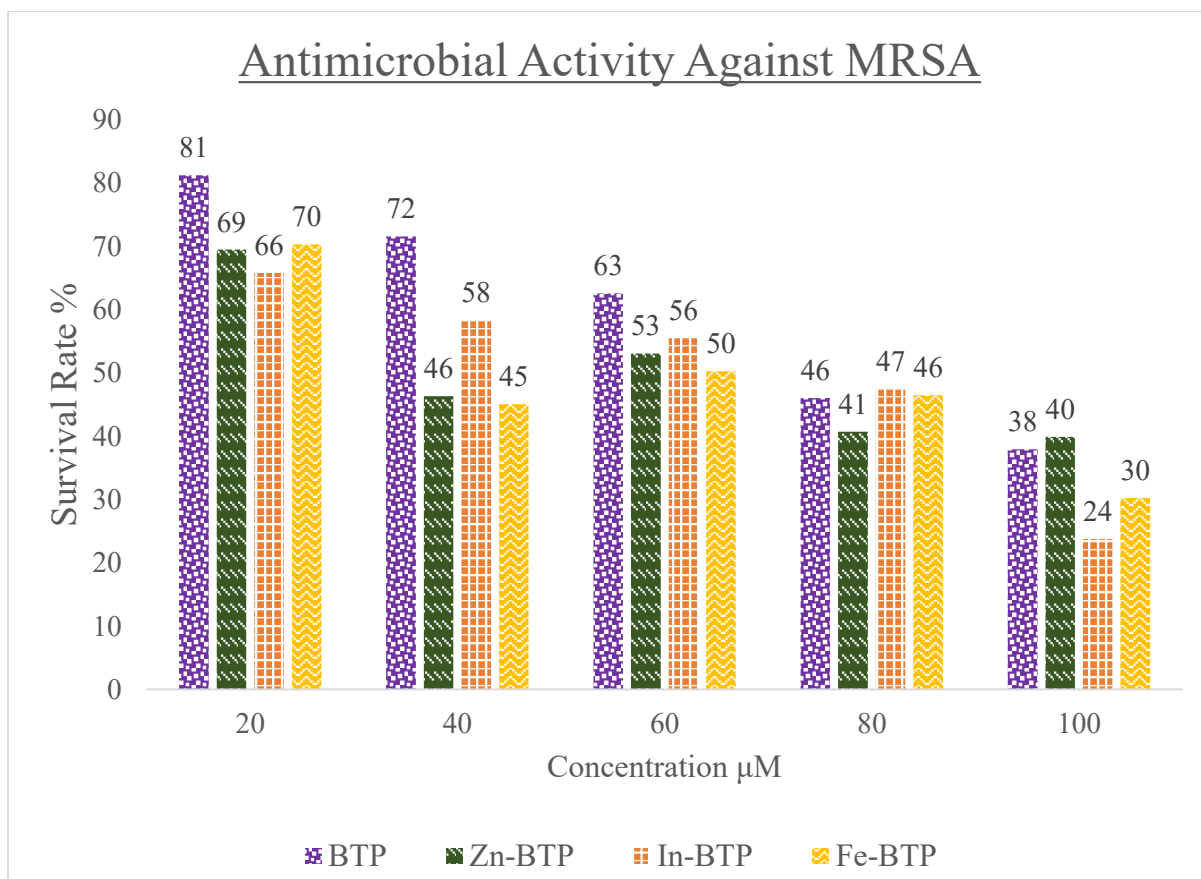


Figure 27: Antimicrobial activity against methicillin resistant *Staphylococcus aureus*

Table 6: Methicillin resistant *Staphylococcus aureus*'s 50% Minimum inhibitory concentration

| Compound | IC ₅₀ MRSA (µM) |
|----------|----------------------------|
| BTP | 75 |
| Zn-BTP | 34 |
| In-BTP | 76 |
| Fe-BTP | 33 |

Based on the IC₅₀ (Gomis-Tena *et al.*, 2020) values in [Table 6](#) the most potent porphyrins against MRSA were Fe-BTP and Zn-BTP.

4.5.2. Carbapenem Resistant *Escherichia coli*

To demonstrate the role of light in the antimicrobial activity of BTP and its metal analogues against carbapenem resistant *Escherichia coli* (*CRE.coli*), their activity was compared under light and dark conditions. The results are summarised in [Figure 28](#).

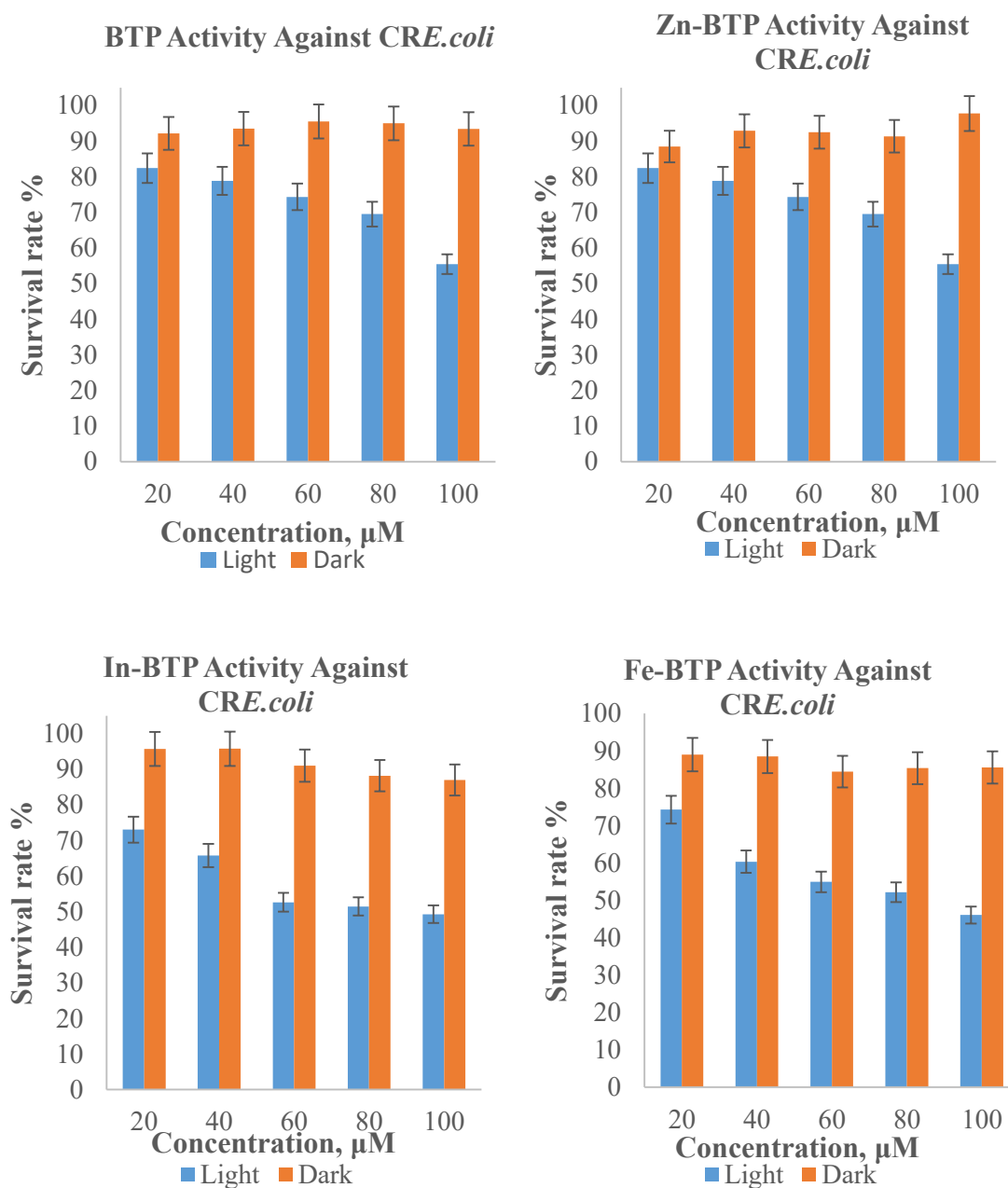


Figure 28: Antimicrobial activity of *meso*-tetra(5-bromothiophen-2-yl)porphyrin and metallated analogues against carbapenem resistant *Escherichia coli*

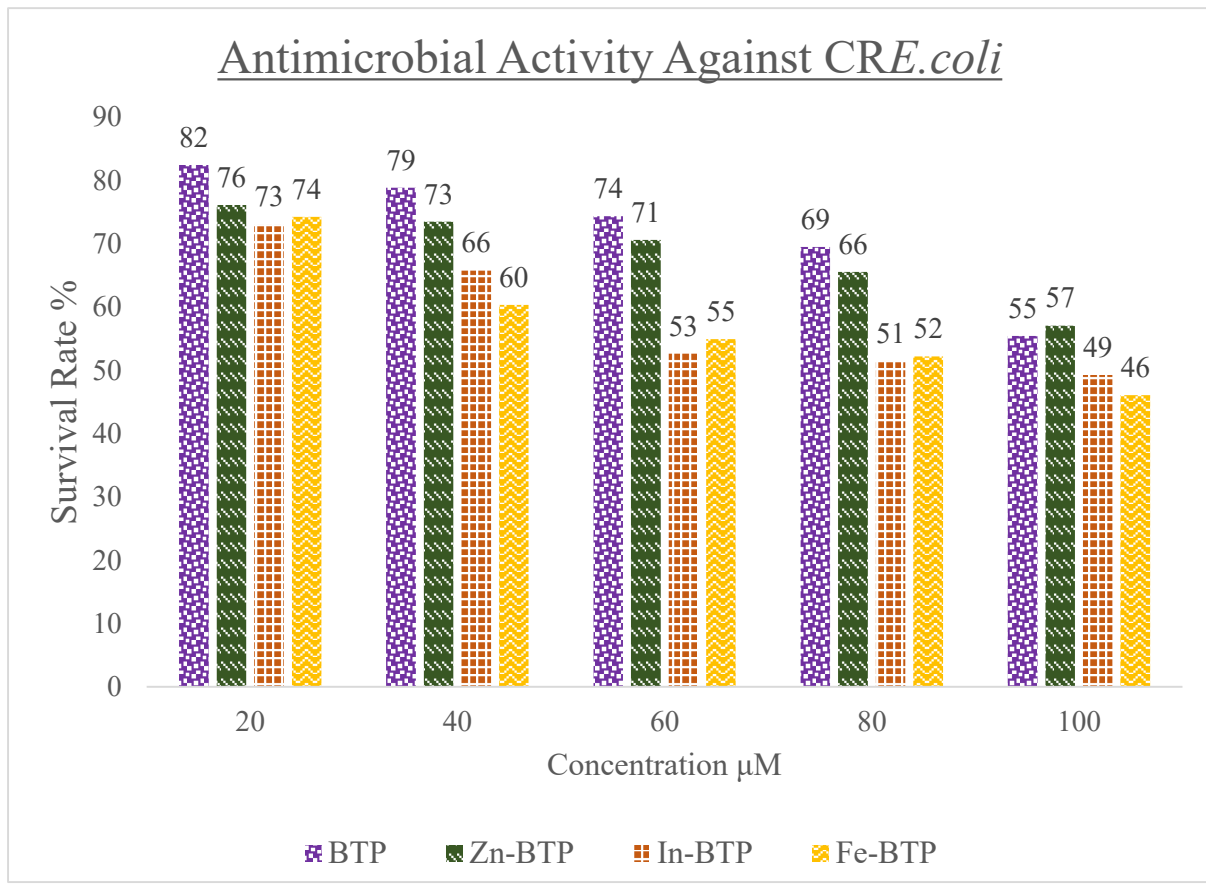
From [Figure 28](#), it was clear that the survival rate of *CRE.coli* in dark conditions was higher than those in light conditions, demonstrating the necessity of light in photosensitising BTP and its metal analogues for potential application in photodynamic water disinfection. This was further supported by analysis of variance (ANOVA) one-factor test, which showed a significant difference between the two conditions, thus highlighting the necessity of light in photodynamic water disinfection. [Table 7](#)

Table 7: Significance tests for light against dark conditions- carbapenem resistant *Escherichia coli*

| CRE.coli ANOVA-One Factor | | |
|----------------------------------|----------|-------------------|
| Compound | F | F critical |
| BTP | 21.3906 | 5.3177 |
| Zn-BTP | 41.9825 | 5.3177 |
| In-BTP | 42.6894 | 5.3177 |
| Fe-BTP | 36.2188 | 5.3177 |

Having demonstrated the importance of light in the antimicrobial activity of BTP and its metal analogues, the rest of the antimicrobial studies are discussed under light conditions. The concentration-dependent antibacterial activity of BTP and its metal analogues and their

respective IC₅₀s against MRSA under light conditions are summarised in



[Figure 29](#) and [Table 8](#), respectively.

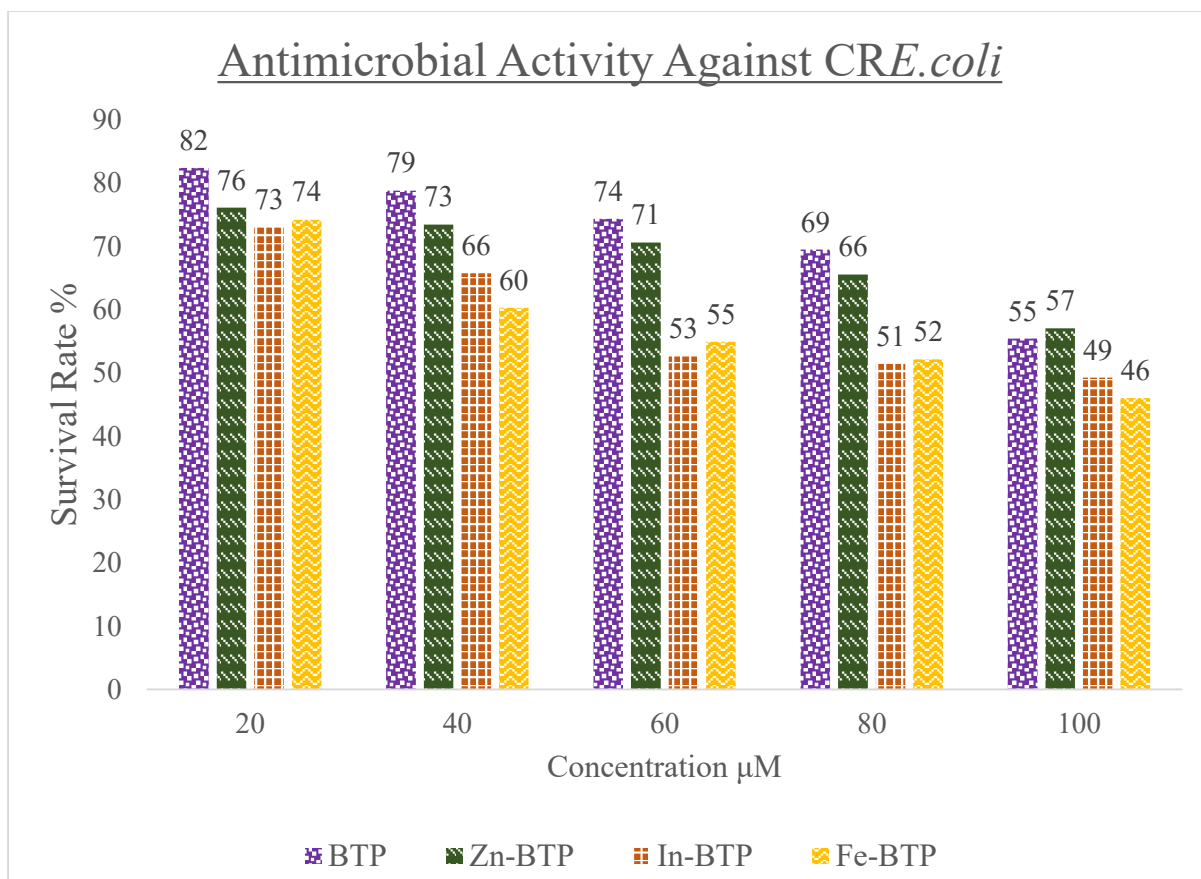


Figure 29: Antimicrobial activity against carbapenem resistant *Escherichia coli*

Fe-BTP and In-BTP were the only ones to have a 50% inhibitory concentration (IC₅₀) below 100 μM each as shown in [Table 8](#).

Table 8: Carbapenem resistant *Escherichia coli*'s 50% Minimum inhibitory concentration

| Compound | IC ₅₀ <i>CRE.coli</i> (μM) |
|----------|---------------------------------------|
| BTP | - |
| Zn-BTP | - |
| In-BTP | 91 |
| Fe-BTP | 87 |

The most potent porphyrins assayed against *CRE.coli* based on their IC₅₀ values were Fe-BTP and In-BTP. Note that IC₅₀ is used as the standard measure for efficacy of compounds against bacteria (Gomis-Tena *et al.*, 2020).

CRE.coli was more resilient to BTP and its metal analogues than MRSA, with higher concentrations of Fe-BTP and In-BTP needed to arrive at IC₅₀. This may be due to an adaptation that is unique to *CRE.coli*. Indeed, *CRE.coli* is a gram-negative bacteria, which are known to be more resilient against ¹O₂ (Huang *et al.*, 2012). This resilience is based on the nature of the membrane of gram-negative bacteria that affords it better protection against ¹O₂. (Dahl *et al.*, 1989; Hogg, 2013). Fe-BTP was the most efficacious compound against both gram-negative and gram-positive bacteria.

The membrane of gram-negative bacteria is composed of a thin-peptidoglycan layer (~10% by dry-weight) enclosed in a lipid bi-layer of a leaflet of lipopolysaccharide. This increases the impermeability of the gram-negative bacteria and furthermore, the lipopolysaccharide layer is said to possess species that may react with ¹O₂. (Huang *et al.*, 2012; Maisch *et al.*, 2007). This is in contrast to gram-positive bacteria, whose membrane is 70-80% peptidoglycan by dry-weight and is more permeable (Hogg, 2013). This allows for the porphyrin to gain access to the membrane and internal components of the bacteria (Maisch *et al.*, 2007). Indeed in this study it was observed that the antimicrobial activity of BTP and its metallated analogues resemble those of other porphyrins (Xu *et al.*, 2016). This is that: gram-positive bacteria are more susceptible to neutral porphyrins than gram-negative bacteria (Huang *et al.*, 2012; Khisa, 2020).

CHAPTER 5: CONCLUSION AND RECOMMENDATIONS

5.1. Conclusion

In this study, the following conclusions can be drawn:

- (i) The compounds in this study, BTP and its six metallated analogues (Zn, In, Sn, Fe, Co and Ni) were synthesised and characterised successfully.
- (ii) The photo-physical properties of BTP and its metal analogues were determined successfully. For Co-BTP, a hyperchromic shift was observed where a hypsochromic shift was expected. This lent credence to the findings of (Conradie *et al.*, 2021) that there is possibly an alternative explanation for hypsochromic shifts observed in transition elements of d^6 - d^9 electrons.
- (iii) The photo-physical properties of BTP and its metal analogues were simulated successfully using DFT through the functional CAM-B3LYP. The direction of soret band shifts was predicted accurately for the metalloid analogues but for the transition element analogues, the predictions were less accurate.
- (iv) The role of light in the antimicrobial activity of BTP and its metal analogues was established. Gram-positive MRSA was more susceptible to BTP and its analogues compared to *CRE.coli*, with Fe-BTP having the highest efficacy based on its IC_{50} values ($33\mu\text{M}$ for MRSA and $87\mu\text{M}$ for *CRE.coli*). This agreed with the findings of other studies which show that gram-positive bacteria are more susceptible to neutral porphyrins than gram-negative ones.

5.2. Recommendations

As a result of this study, the following recommendations are made:

- (i) In order to enhance the antimicrobial activity of BTP and its metal analogues, a study to enhance the molar absorption coefficient through attachment to substrates or as metal organic frameworks should be conducted. This may allow more light to reach the compounds and thus increase their antimicrobial activity.
- (ii) In order to improve the predictive capacity of CAM-B3LYP amongst the transition metal analogues of BTP, DFT studies for BTP and its metal analogues should be

conducted with correction for London dispersion effects and or with constraints on the geometry of the porphyrins.

- (iii) In order to determine the reason for Fe-BTP's unexpectedly high efficacy, an investigation to establish the mechanism by which it induces microbicidal activity should be conducted. This could bring greater insight on what other criteria should be looked into when choosing PSs.

REFERENCES

- Agardy, F., and Nemerow, N. (2005). *Environmental Solutions*. Elsevier. <https://doi.org/10.1016/B978-0-12-088441-4.X5000-X>
- Ali, M., Nelson, A. R., Lopez, A. L., and Sack, D. A. (2015). Updated Global Burden of Cholera in Endemic Countries. *PLOS Neglected Tropical Diseases*, 9(6), e0003832. <https://doi.org/10.1371/journal.pntd.0003832>
- Arnold, D. P. (1988). Aromatic Ring Currents Illustrated-NMR Spectra of Tin(IV) porphyrin Complexes: An advanced undergraduate experiment. *Journal of Chemical Education*, 65(12), 1111. <https://doi.org/10.1021/ed065p1111>
- Azeh Engwa, G., Udoka Ferdinand, P., Nweke Nwalo, F., and N. Unachukwu, M. (2019). Mechanism and Health Effects of Heavy Metal Toxicity in Humans. In O. Karcioğlu and B. Arslan (Eds.), *Poisoning in the Modern World—New Tricks for an Old Dog?* IntechOpen. <https://doi.org/10.5772/intechopen.82511>
- Babu, B., Amuhaya, E., Oluwole, D., Prinsloo, E., Mack, J., and Nyokong, T. (2019). Preparation of NIR absorbing axial substituted tin(IV) porphyrins and their photocytotoxic properties. *MedChemComm*, 10(1), 41–48. <https://doi.org/10.1039/C8MD00373D>
- Balouiri, M., Sadiki, M., and Ibsouda, S. K. (2016). Methods for in vitro evaluating antimicrobial activity: A review. *Journal of Pharmaceutical Analysis*, 6(2), 71–79. <https://doi.org/10.1016/j.jpha.2015.11.005>
- Bohrerova, Z., and Linden, K. G. (2006). Assessment of DNA Damage and Repair in *Mycobacterium Terraе* after Exposure to UV Irradiation. *Journal of Applied Microbiology*, 101(5), 995–1001. <https://doi.org/10.1111/j.1365-2672.2006.03023.x>
- Boretti, A., and Rosa, L. (2019). Reassessing the Projections of the World Water Development Report. *Npj Clean Water*, 2(1), 15. <https://doi.org/10.1038/s41545-019-0039-9>
- Boyd, R. I., Ahmad, S., Singh, R., Fazal, Z., Prins, G. S., Madak Erdogan, Z., Irudayaraj, J., and Spinella, M. J. (2022). Toward a Mechanistic Understanding of Poly- and Perfluoroalkylated Substances and Cancer. *Cancers*, 14(12), 2919. <https://doi.org/10.3390/cancers14122919>
- Bridier, A., Briandet, R., Thomas, V., and Dubois-Brissonnet, F. (2011). Resistance of Bacterial Biofilms to Disinfectants: A review. *Biofouling*, 27(9), 1017–1032. <https://doi.org/10.1080/08927014.2011.626899>
- Cabral, J. P. S. (2010). Water Microbiology. Bacterial Pathogens and Water. *International Journal of Environmental Research and Public Health*, 7(10), 3657–3703. <https://doi.org/10.3390/ijerph7103657>
- Castro-Alfárez, M., Polo-López, M. I., and Fernández-Ibáñez, P. (2016). Intracellular Mechanisms of Solar Water Disinfection. *Scientific Reports*, 6(1), 38145. <https://doi.org/10.1038/srep38145>

- Ceci, A., Pinzari, F., Russo, F., Persiani, A. M., and Gadd, G. M. (2019). Roles Of Saprotrophic Fungi In Biodegradation or Transformation of Organic and Inorganic Pollutants in Co-contaminated Sites. *Applied Microbiology and Biotechnology*, 103(1), 53–68. <https://doi.org/10.1007/s00253-018-9451-1>
- Cevallos-Mendoza, J., Amorim, C. G., Rodríguez-Díaz, J. M., and Montenegro, M. da C. B. S. M. (2022). Removal of Contaminants from Water by Membrane Filtration: A Review. *Membranes*, 12(6), 570. <https://doi.org/10.3390/membranes12060570>
- Chu, C., Ryberg, E. C., Loeb, S. K., Suh, M.-J., and Kim, J.-H. (2019). Water Disinfection in Rural Areas Demands Unconventional Solar Technologies. *Accounts of Chemical Research*, 52(5), 1187–1195. <https://doi.org/10.1021/acs.accounts.8b00578>
- Cieplik, F., Deng, D., Crielaard, W., Buchalla, W., Hellwig, E., Al-Ahmad, A., and Maisch, T. (2018). Antimicrobial Photodynamic Therapy – what we know and what we don't. *Critical Reviews in Microbiology*, 44(5), 571–589. <https://doi.org/10.1080/1040841X.2018.1467876>
- Cohen, M. (2020). Turning up the Heat on COVID-19: Heat as a therapeutic intervention. *F1000Research*, 9, 292. <https://doi.org/10.12688/f1000research.23299.2>
- Collado, G. A., Valladares, M. A., and Méndez, M. A. (2013). Hidden Diversity in Spring Snails from the Andean Altiplano, the Second Highest Plateau on Earth, and the Atacama Desert, the Driest Place in the World. *Zoological Studies*, 52(1), 50. <https://doi.org/10.1186/1810-522X-52-50>
- Conradie, J., Wamser, C. C., and Ghosh, A. (2021). Understanding Hyperporphyrin Spectra: TDDFT Calculations on Diprotonated Tetrakis(p -aminophenyl)porphyrin. *The Journal of Physical Chemistry A*, 125(46), 9953–9961. <https://doi.org/10.1021/acs.jpca.1c06621>
- Craig, R. A., McCoy, C. P., Gorman, S. P., and Jones, D. S. (2015). Photosensitisers – The progression from photodynamic therapy to anti-infective surfaces. *Expert Opinion on Drug Delivery*, 12(1), 85–101. <https://doi.org/10.1517/17425247.2015.962512>
- Cramer, C. J. (2004). *Essentials of computational chemistry: Theories and models* (2nd ed). Wiley.
- Cullom, A. C., Martin, R. L., Song, Y., Williams, K., Williams, A., Pruden, A., and Edwards, M. A. (2020). Critical Review: Propensity of Premise Plumbing Pipe Materials to Enhance or Diminish Growth of Legionella and Other Opportunistic Pathogens. *Pathogens*, 9(11), 957. <https://doi.org/10.3390/pathogens9110957>
- Dahl, T. A., Midden, W. R., and Hartman, P. E. (1989). Comparison of Killing of Gram-negative and Gram-positive Bacteria by Pure Singlet Oxygen. *Journal of Bacteriology*, 171(4), 2188–2194. <https://doi.org/10.1128/jb.171.4.2188-2194.1989>
- de Castro Medeiros, L., de Alencar, F. L. S., Navoni, J. A., de Araujo, A. L. C., and do Amaral, V. S. (2019). Toxicological Aspects of Trihalomethanes: A systematic review. *Environmental Science and Pollution Research*, 26(6), 5316–5332. <https://doi.org/10.1007/s11356-018-3949-z>

- Destruel, P., Taufer, M., D'Ambrosio, C., Da Via, C., Fabre, J. P., Kirkby, J., and Leutz, H. (1989). A New Plastic Scintillator with Large Stokes Shift. *Nuclear Instruments and Methods in Physics Research Section A: Accelerators, Spectrometers, Detectors and Associated Equipment*, 276(1–2), 69–77. [https://doi.org/10.1016/0168-9002\(89\)90617-7](https://doi.org/10.1016/0168-9002(89)90617-7)
- Drinking Water and Health,: Volume 2 (p. 1904). (1980). National Academies Press. <https://doi.org/10.17226/1904>
- Fukuzaki, S. (2006). Mechanisms of Actions of Sodium Hypochlorite in Cleaning and Disinfection Processes. *Biocontrol Science*, 11(4), 147–157. <https://doi.org/10.4265/bio.11.147>
- Fushimi, Y., Koinuma, M., Yasuda, Y., Nomura, K., and Asano, M. S. (2017). Effects of End-Groups on Photophysical Properties of Poly(9,9-di-n-octylfluorene-2,7-vinylene)s Linked with Metalloporphyrins: Synthesis and Time-Resolved Fluorescence Spectroscopy. *Macromolecules*, 50(5), 1803–1814. <https://doi.org/10.1021/acs.macromol.7b00047>
- Galal-Gorchev, H. (1996). Chlorine in Water Disinfection. *Pure and Applied Chemistry*, 68(9), 1731–1735. <https://doi.org/10.1351/pac199668091731>
- Ghosh, A., and Conradie, J. (2021). The Dog That Didn't Bark: A New Interpretation of Hypso-porphyrin Spectra and the Question of Hypso-corroles. *The Journal of Physical Chemistry A*, 125(46), 9962–9968. <https://doi.org/10.1021/acs.jpca.1c08425>
- Ghosh, A., Mobin, S. M., Fröhlich, R., Butcher, R. J., Maity, D. K., and Ravikanth, M. (2010). Effect of Five Membered Versus Six Membered Meso-Substituents on Structure and Electronic Properties of Mg(II) Porphyrins: A Combined Experimental and Theoretical Study. *Inorganic Chemistry*, 49(18), 8287–8297. <https://doi.org/10.1021/ic1008522>
- Goerigk, L., and Mehta, N. (2019). A Trip to the Density Functional Theory Zoo: Warnings and Recommendations for the User. *Australian Journal of Chemistry*, 72(8), 563. <https://doi.org/10.1071/CH19023>
- Gomis-Tena, J., Brown, B. M., Cano, J., Trenor, B., Yang, P.-C., Saiz, J., Clancy, C. E., and Romero, L. (2020). When Does the IC50 Accurately Assess the Blocking Potency of a Drug? *Journal of Chemical Information and Modeling*, 60(3), 1779–1790. <https://doi.org/10.1021/acs.jcim.9b01085>
- Goncharuk, V. V., Kovalenko, V. F., Saprykina, M. N., Bolgova, E. S., and Osmalenyi, N. S. (2019). Biotesting of Water Contaminated by Microorganisms. *Journal of Water Chemistry and Technology*, 41(1), 63–66. <https://doi.org/10.3103/S1063455X19010107>
- Gonsalves, A. M. d'A R., Varejão, J. M. T. B., and Pereira, M. M. (1991). Some New Aspects Related to the Synthesis of Meso-substituted Porphyrins. *Journal of Heterocyclic Chemistry*, 28(3), 635–640. <https://doi.org/10.1002/jhet.5570280317>

- Gottschalk, C., Libra, J. A., and Saupe, A. (2010). *Ozonation of Water and Waste Water: A practical guide to understanding ozone and its applications* (2nd completely rev. and updated ed). Wiley-VCH.
- Gray, N. (2013). Free and Combined Chlorine. In *Microbiology of Waterborne Diseases* (2nd ed., pp. 571–581). Elsevier Science and Technology.
- Gray, N. F. (2014). Ozone Disinfection. In *Microbiology of Waterborne Diseases* (pp. 599–615). Elsevier. <https://doi.org/10.1016/B978-0-12-415846-7.00033-0>
- Hally, C., Rodríguez-Amigo, B., Bresolí-Obach, R., Planas, O., Nos, J., Boix-Garriga, E., Ruiz-González, R., and Nonell, S. (2018). CHAPTER 4. Photodynamic Therapy. In M. Thanou (Ed.), *Drug Discovery* (pp. 86–122). Royal Society of Chemistry. <https://doi.org/10.1039/9781788010597-00086>
- Hanna, L., Movsesian, E., Orozco, M., Bernot Jr., A. R., Asadinamin, M., Shenje, L., Ullrich, S., Zhao, Y., Marshall, N., Weeks, J. A., Thomas, M. B., Teprovich Jr., J. A., and Ward, P. A. (2022). Spectroscopic Investigation of the Electronic and Excited State Properties of Para-Substituted Tetraphenyl Porphyrins and their Electrochemically Generated Ions. *Spectrochimica Acta Part A: Molecular and Biomolecular Spectroscopy*, 278, 121300. <https://doi.org/10.1016/j.saa.2022.121300>
- Hoff, J. C., and Akin, E. W. (1986). Microbial resistance to disinfectants: Mechanisms and Significance. *Environmental Health Perspectives*, 69, 7–13. <https://doi.org/10.1289/ehp.86697>
- Hogg, S. (2013). *Essential microbiology* (2nd ed). Wiley-Blackwell.
- Huang, L., Xuan, Y., Koide, Y., Zhiyentayev, T., Tanaka, M., and Hamblin, M. R. (2012). Type I and Type II Mechanisms of Antimicrobial Photodynamic Therapy: An in vitro study on gram-negative and gram-positive bacteria. *Lasers in Surgery and Medicine*, 44(6), 490–499. <https://doi.org/10.1002/lsm.22045>
- Jensen, F. (2017). *Introduction to computational chemistry* (Third edition). John Wiley and Sons.
- Jori, G. (2011). Photosensitization: Basic Principles. In *Organic Photochemistry and Photobiology* (3rd ed., Vol. 2, pp. 1105–1114).
- Jyoti, K. K., and Pandit, A. B. (2004). Ozone and Cavitation for Water Disinfection. *Biochemical Engineering Journal*, 18(1), 9–19. [https://doi.org/10.1016/S1369-703X\(03\)00116-5](https://doi.org/10.1016/S1369-703X(03)00116-5)
- Khisa, J. (2020). Synthesis, Characterisation and Photophysical Studies of Novel Porphyrin Based Compounds for Application in Photodynamic Antimicrobial Chemotherapy [University of Nairobi]. http://erepository.uonbi.ac.ke/bitstream/handle/11295/152926/Khisa%20Jackline%20N_Synthesis,%20Characterization%20and%20Photophysical%20Studies%20of%20Novel%20Porphyrin-based%20Compounds%20for%20Application%20in%20Photodynamic%20Antimicrobial%20Chemotherapy%20%20Pact.pdf?sequence=1

- Kortov, V., and Ustyantsev, Yu. (2013). Chernobyl Accident: Causes, consequences and problems of radiation measurements. *Radiation Measurements*, 55, 12–16. <https://doi.org/10.1016/j.radmeas.2012.05.015>
- Lee, Y., Jo, A., and Park, S. B. (2015). Rational Improvement of Molar Absorptivity Guided by Oscillator Strength: A Case Study with Furoindolizine-Based Core Skeleton. *Angewandte Chemie International Edition*, 54(52), 15689–15693. <https://doi.org/10.1002/anie.201506429>
- Li, F., Kexin Yang, Tyhonas, J. S., MacCrum, K. A., and Lindsey, J. S. (1997). Beneficial Effects of Salts on an Acid-Catalyzed Condensation Leading to Porphyrin Formation. *Tetrahedron*, 53(37), 12339–12360. [https://doi.org/10.1016/S0040-4020\(97\)00770-9](https://doi.org/10.1016/S0040-4020(97)00770-9)
- Lindsey, J. S. (2010). Synthetic Routes to Meso -Patterned Porphyrins. *Accounts of Chemical Research*, 43(2), 300–311. <https://doi.org/10.1021/ar900212t>
- Lismont, M., Dreesen, L., and Wuttke, S. (2017). Metal-Organic Framework Nanoparticles in Photodynamic Therapy: Current Status and Perspectives. *Advanced Functional Materials*, 27(14), 1606314. <https://doi.org/10.1002/adfm.201606314>
- Mack, J. (2017). Expanded, Contracted, and Isomeric Porphyrins: Theoretical Aspects. *Chemical Reviews*, 117(4), 3444–3478. <https://doi.org/10.1021/acs.chemrev.6b00568>
- Mack, J., Asano, Y., Kobayashi, N., and Stillman, M. J. (2005). Application of MCD Spectroscopy and TD-DFT to a Highly Non-Planar Porphyrinoid Ring System. New Insights on Red-Shifted Porphyrinoid Spectral Bands. *Journal of the American Chemical Society*, 127(50), 17697–17711. <https://doi.org/10.1021/ja0540728>
- Mack, J., Stillman, M. J., and Kobayashi, N. (2007). Application of MCD Spectroscopy to Porphyrinoids. *Coordination Chemistry Reviews*, 251(3–4), 429–453. <https://doi.org/10.1016/j.ccr.2006.05.011>
- Magana-Arachchi, D. N., and Wanigatunge, R. P. (2020). Ubiquitous Waterborne Pathogens. in *Waterborne Pathogens* (pp. 15–42). Elsevier. <https://doi.org/10.1016/B978-0-12-818783-8.00002-5>
- Magaraggia, M., Coppellotti, O., Fabris, C., Guidolin, L., and Jori, G. (2011). Chapter 17. Inactivation of Microbial Pathogens by Photosensitized Processes: Environmental Applications. In M. R. Hamblin and G. Jori (Eds.), *Comprehensive Series in Photochemical and Photobiological Sciences* (pp. 403–423). Royal Society of Chemistry. <https://doi.org/10.1039/9781849733083-00403>
- Maisch, T., Baier, J., Franz, B., Maier, M., Landthaler, M., Szeimies, R.-M., and Bäuml, W. (2007). The Role of Singlet Oxygen and Oxygen Concentration in Photodynamic Inactivation of Bacteria. *Proceedings of the National Academy of Sciences*, 104(17), 7223–7228. <https://doi.org/10.1073/pnas.0611328104>
- Malinowski, N., Domingos, S., Wylie, J., Morgan, M. J., Metcalfe, S., Walsh, T., Ahmed, W., Kaksonen, A. H., and Puzon, G. J. (2022). Free-Living Amoeba and Associated Pathogenic Bacteria in Well-Chlorinated Drinking Water Storage Tanks. *ACS ES and T Water*, 2(9), 1511–1520. <https://doi.org/10.1021/acsestwater.1c00428>

- Managa, M., Amuhaya, E. K., and Nyokong, T. (2015). Photodynamic Antimicrobial Chemotherapy Activity of (5,10,15,20-tetrakis(4-(4-carboxyphenylcarbonoimidoyl)phenyl)porphyrinato) chloro gallium(III). *Spectrochimica Acta Part A: Molecular and Biomolecular Spectroscopy*, 151, 867–874. <https://doi.org/10.1016/j.saa.2015.06.088>
- Marsh, D., and Mink, L. (1996). Microscale Synthesis and Electronic Absorption Spectroscopy of Tetraphenylporphyrin H₂(TPP) and Metalloporphyrins ZnII(TPP) and NiII(TPP). *Journal of Chemical Education*, 73(12), 1188. <https://doi.org/10.1021/ed073p1188>
- Méndez-Vilas, A. (2011). *Science Against Microbial Pathogens: Communicating current research and technological advances*. Formatex Research Center.
- Munzeiwa, W. A., Ruziwa, D. T., and Chaukura, N. (2022). Environmental Pollutants: Metal(loid)s and Radionuclides. In R. Selvasembian, E. D. van Hullebusch, and J. Mal (Eds.), *Biotechnology for Environmental Protection* (pp. 1–23). Springer Nature Singapore. https://doi.org/10.1007/978-981-19-4937-1_1
- Murray, C. J., Ikuta, K. S., Sharara, F., Swetschinski, L., Robles Aguilar, G., Gray, A., Han, C., Bisignano, C., Rao, P., Wool, E., Johnson, S. C., Browne, A. J., Chipeta, M. G., Fell, F., Hackett, S., Haines-Woodhouse, G., Kashef Hamadani, B. H., Kumaran, E. A. P., McManigal, B., ... Naghavi, M. (2022). Global burden of bacterial antimicrobial resistance in 2019: A systematic analysis. *The Lancet*, 399(10325), 629–655. [https://doi.org/10.1016/S0140-6736\(21\)02724-0](https://doi.org/10.1016/S0140-6736(21)02724-0)
- Murray, P. R., Rosenthal, K. S., and Pfaller, M. A. (2013). *Medical Microbiology* (7th Edition). Elsevier/Saunders.
- Nonell, S., and Flors, C. (Eds.). (2016). *Singlet Oxygen: Applications in Biosciences and Nanosciences* (Vol. 1). Royal Society of Chemistry. <https://doi.org/10.1039/9781782622208>
- Oloo, S. (2020). *Solar-driven Photocatalytic Activity of Porphyrin Sensitized Titanium Dioxide in Methylene Blue Degradation and Sacrificial Hydrogen Generation*. University of Nairobi.
- Oyim, J., Amuhaya, E., Matshitse, R., Mack, J., and Nyokong, T. (2022). Integrated Photocatalyst Adsorbents Based on Porphyrin Anchored to Activated Carbon Granules for Water Treatment. *Carbon Trends*, 8, 100191. <https://doi.org/10.1016/j.cartre.2022.100191>
- Pattengale, B., Liu, Q., Hu, W., Yang, S., He, P., Tender, S. L., Wang, Y., Zhang, X., Zhou, Z., Zhang, J., and Huang, J. (2019). Selective Excited-State Dynamics in a Unique Set of Rationally Designed Ni Porphyrins. *The Journal of Physical Chemistry C*, 123(29), 17994–18000. <https://doi.org/10.1021/acs.jpcc.9b05413>
- Pegau, W. S., Gray, D., and Zaneveld, J. R. V. (1997). Absorption and Attenuation of Visible and Near-Infrared Light in Water: Dependence on temperature and salinity. *Applied Optics*, 36(24), 6035. <https://doi.org/10.1364/AO.36.006035>

- Percival, S. L. (Ed.). (2014). *Microbiology of Waterborne Diseases: Microbiological aspects and risks* (Second edition). Elsevier, Academic Press.
- Radhouani, H., Silva, N., Poeta, P., Torres, C., Correia, S., and Igrejas, G. (2014). Potential Impact of Antimicrobial Resistance in Wildlife, Environment and Human Health. *Frontiers in Microbiology*, 5. <https://doi.org/10.3389/fmicb.2014.00023>
- Rosen, G. M., Pou, S., Ramos, C. L., Cohen, M. S., and Britigan, B. E. (1995). Free Radicals And Phagocytic Cells. *The FASEB Journal*, 9(2), 200–209. <https://doi.org/10.1096/fasebj.9.2.7540156>
- Ruziwa, D. T., Rutsito, D. D., and Chaukura, N. (2022). Environmental Pollutants: Organic and Emerging Contaminants. In R. Selvasembian, E. D. van Hullebusch, and J. Mal (Eds.), *Biotechnology for Environmental Protection* (pp. 25–41). Springer Nature Singapore. https://doi.org/10.1007/978-981-19-4937-1_2
- Sarma, H., and Prasad, M. N. V. (2016). Phytomanagement of Polycyclic Aromatic Hydrocarbons and Heavy Metals-Contaminated Sites in Assam, North Eastern State of India, for Boosting Bioeconomy. In *Bioremediation and Bioeconomy* (pp. 609–626). Elsevier. <https://doi.org/10.1016/B978-0-12-802830-8.00024-1>
- Sayer, P., Gouterman, M., and Connell, C. R. (1982). Metalloid Porphyrins and Phthalocyanines. *Accounts of Chemical Research*, 15(3), 73–79. <https://doi.org/10.1021/ar00075a002>
- Senge, M. O., Sergeeva, N. N., and Hale, K. J. (2021). Classic Highlights in Porphyrin And Porphyrinoid Total Synthesis and Biosynthesis. *Chemical Society Reviews*, 50(7), 4730–4789. <https://doi.org/10.1039/C7CS00719A>
- Sharma, S., and Bhattacharya, A. (2017). Drinking Water Contamination and Treatment Techniques. *Applied Water Science*, 7(3), 1043–1067. <https://doi.org/10.1007/s13201-016-0455-7>
- Śmiech, K. M., Kovács, T., Wildschut, R. F., Criado Monleon, A. J., de Vries-Onclin, B., Bowen, J. G., and Agostinho, L. L. F. (2020). Thermal Disinfection Of Hospital Wastewater in a Pilot-Scale Continuous-Flow System. *Applied Water Science*, 10(4), 101. <https://doi.org/10.1007/s13201-020-01181-8>
- Steinhauser, G., Brandl, A., and Johnson, T. E. (2014). Comparison of the Chernobyl And Fukushima Nuclear Accidents: A review of the environmental impacts. *Science of The Total Environment*, 470–471, 800–817. <https://doi.org/10.1016/j.scitotenv.2013.10.029>
- Sun, Z., Jiao, S., Li, F., Wen, J., Yu, Y., Liu, Y., Cao, M., Li, L., Zhou, Y., and She, Y. (2019). Cover Feature: Acid Activation and Chemical Oxidation in the Synthesis of Meso - Tetraphenylporphyrin using a Mixed-Solvent System (*Asian J. Org. Chem.* 4/2019). *Asian Journal of Organic Chemistry*, 8(4), 429–429. <https://doi.org/10.1002/ajoc.201900186>

- Sun, Z., She, Y., Cao, M., Zhou, Q., Lu, X., and Zhang, S. (2013). Synthesis of substituted Meso-tetraphenylporphyrins in Mixed Solvent Systems. *Arkivoc*, 2013(3), 389–400. <https://doi.org/10.3998/ark.5550190.p008.097>
- Thandu, M., Comuzzi, C., and Goi, D. (2015). Phototreatment of Water by Organic Photosensitizers and Comparison with Inorganic Semiconductors. *International Journal of Photoenergy*, 2015, 1–22. <https://doi.org/10.1155/2015/521367>
- Trucks, G. W., Schlegel, H. B., Scuseria, G. E., Robb, M. A., Cheeseman, J. R., Scalmani, G., Barone, V., Mennucci, B., Petersson, G. A., Nakatsuji, H. M., Caricato, M., Li, X. H. P., Hratchian, H. P., Zheng, G., Sonnenberg, J.L, Hada, M, Ehara, M, Toyota, K, Fukuda, R, ... Fox, D. J. (2013). Gaussian 09 [Computer software]. Gaussian, Inc.,
- United Nations Department for Economic and Social Affairs. (2023). World Population Prospects 2022: Summary of results. UNITED NATIONS.
- United Nations, Department of Economic and Social Affairs, and Population Division. (2019). World urbanization prospects: The 2018 revision.
- United Nations Environment Programme. (2022). Environmental Dimensions of Antimicrobial Resistance—Summary for Policymakers. United Nations Environment Programme. <https://wedocs.unep.org/20.500.11822/38373>
- Valicsek, Z., and Horváth, O. (2013). Application of the Electronic Spectra of Porphyrins for Analytical Purposes: The effects of metal ions and structural distortions. *Microchemical Journal*, 107, 47–62. <https://doi.org/10.1016/j.microc.2012.07.002>
- Vázquez-Tapia, I., Salazar-Martínez, T., Acosta-Castro, M., Meléndez-Castolo, K. A., Mahlkecht, J., Cervantes-Avilés, P., Capparelli, M. V., and Mora, A. (2022). Occurrence Of Emerging Organic Contaminants and Endocrine Disruptors in Different Water Compartments in Mexico – A review. *Chemosphere*, 308, 136285. <https://doi.org/10.1016/j.chemosphere.2022.136285>
- Wainwright, M. (1998). Photodynamic Antimicrobial Chemotherapy (PACT). *Journal of Antimicrobial Chemotherapy*, 42(1), 13–28. <https://doi.org/10.1093/jac/42.1.13>
- Wamser, C. C., and Ghosh, A. (2022). The Hyperporphyrin Concept: A Contemporary Perspective. *JACS Au*, *jacsau.2c00255*. <https://doi.org/10.1021/jacsau.2c00255>
- Wang, C., and Wamser, C. C. (2015). NMR Study of Hyperporphyrin Effects in the Protonations of Porphyrins with 4-Aminophenyl and 4-Pyridyl Meso Substituents. *The Journal of Organic Chemistry*, 80(15), 7351–7359. <https://doi.org/10.1021/acs.joc.5b00690>
- Wang, L., Ye, C., Guo, L., Chen, C., Kong, X., Chen, Y., Shu, L., Wang, P., Yu, X., and Fang, J. (2021). Assessment of the UV/Chlorine Process in the Disinfection of *Pseudomonas aeruginosa*: Efficiency and Mechanism. *Environmental Science and Technology*, 55(13), 9221–9230. <https://doi.org/10.1021/acs.est.1c00645>
- Wardle, B. (2009). Principles and Applications of Photochemistry. Wiley.

- Xu, Z., Gao, Y., Meng, S., Yang, B., Pang, L., Wang, C., and Liu, T. (2016). Mechanism and In Vivo Evaluation: Photodynamic Antibacterial Chemotherapy of Lysine-Porphyrin Conjugate. *Frontiers in Microbiology*, 7. <https://doi.org/10.3389/fmicb.2016.00242>
- Xue, Y., Dou, Y., An, L., Zheng, Y., Zhang, L., and Liu, Y. (2016). Electronic Structure and Spectral Properties of Aurones as Visible Range Fluorescent Probes: A DFT/TDDFT study. *RSC Advances*, 6(9), 7002–7010. <https://doi.org/10.1039/C5RA25733F>
- Yanai, T., Tew, D. P., and Handy, N. C. (2004). A New Hybrid Exchange–Correlation Functional Using the Coulomb–Attenuating Method (CAM-B3LYP). *Chemical Physics Letters*, 393(1–3), 51–57. <https://doi.org/10.1016/j.cplett.2004.06.011>
- Zhang, A., Kwan, L., and Stillman, M. J. (2017). The Spectroscopic Impact of Interactions with the Four Gouterman Orbitals from Peripheral Decoration of Porphyrins with Simple Electron Withdrawing and Donating Groups. *Organic and Biomolecular Chemistry*, 15(43), 9081–9094. <https://doi.org/10.1039/C7OB01960B>
- Zheng, W., Shan, N., Yu, L., and Wang, X. (2008). UV–Visible, Fluorescence And EPR Properties of Porphyrins and Metalloporphyrins. *Dyes and Pigments*, 77(1), 153–157. <https://doi.org/10.1016/j.dyepig.2007.04.007>
- Zhu, X., Su, Q., Feng, W., and Li, F. (2017). Anti-Stokes Shift Luminescent Materials for Bio-Applications. *Chemical Society Reviews*, 46(4), 1025–1039. <https://doi.org/10.1039/C6CS00415F>
- Zhu, Z.-H., Liu, Y., Song, C., Hu, Y., Feng, G., and Tang, B. Z. (2022). Porphyrin-Based Two-Dimensional Layered Metal–Organic Framework with Sono-/Photocatalytic Activity for Water Decontamination. *ACS Nano*, 16(1), 1346–1357. <https://doi.org/10.1021/acsnano.1c09301>

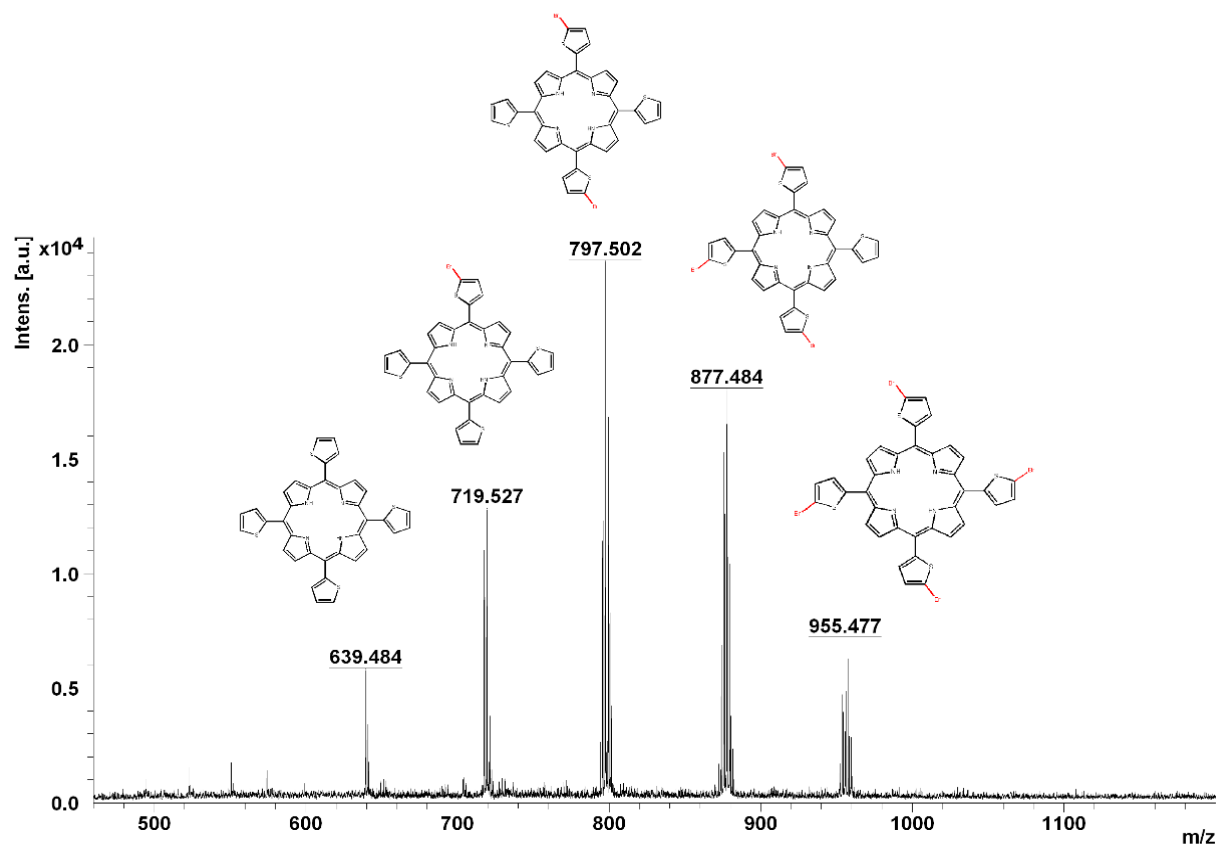
Internet References

- Centers for Disease Control and Prevention. (2023, August 2). Disinfection and Sterilization. Infection Control. <https://www.cdc.gov/infectioncontrol/guidelines/disinfection/glossary.html>, link accessed on 2nd August, 2023.
- Tomberg, A. (2019). An Introduction to Computational Chemistry Using G09W and Avogadro Software. Barrett-Group; November, 2019. <https://barrett-group.mcgill.ca/tutorials/Gaussian%20tutorial.pdf>, link accessed on 22nd April, 2023.
- United Nations Environment Programme. (2022). Environmental Dimensions of Antimicrobial Resistance—Summary for Policymakers. United Nations Environment Programme. <https://wedocs.unep.org/20.500.11822/38373>, link accessed on 22nd April, 2023.
- World Bank. (2022). GDP (Current US\$)- Peru [Database]. The World Bank IRDA-IDA. <https://data.worldbank.org/indicator/NY.GDP.MKTP.CD?end=2021&locations=PE&start=1960&view=chart>, link accessed on 22nd April, 2023.
- World Health Organization. (2016). Protecting Surface Water for Health: Identifying, Assessing and Managing Drinking-Water Quality Risks in Surface-Water Catchments. World Health Organization. <https://apps.who.int/iris/handle/10665/246196>, link accessed on 22nd April, 2023.
- World Health Organization. (2018). WHO Housing and Health Guidelines. World Health Organization. <https://apps.who.int/iris/handle/10665/276001>, link accessed on 22nd April, 2023.
- World Health Organization. (2020). WHO Global Water, Sanitation and Hygiene: Annual report 2019. World Health Organization. <https://apps.who.int/iris/handle/10665/336582>, link accessed on 22nd April, 2023.

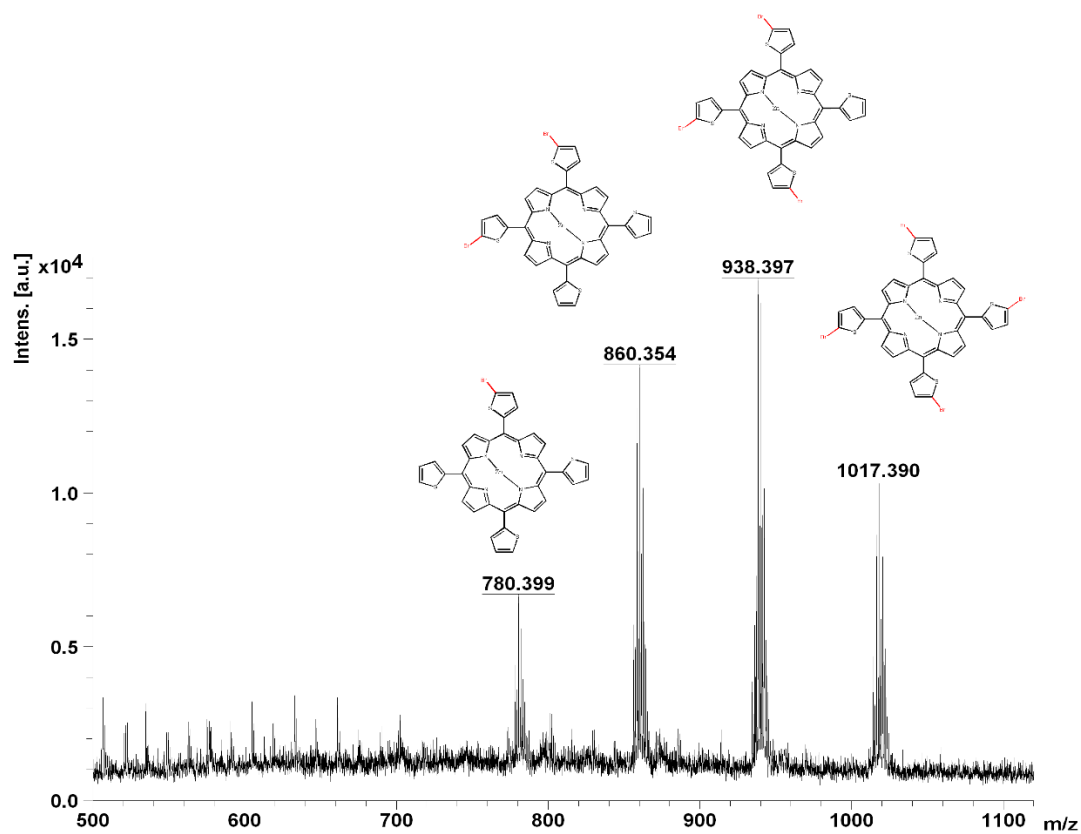
APPENDICES

Appendix 1: Mass Spectra

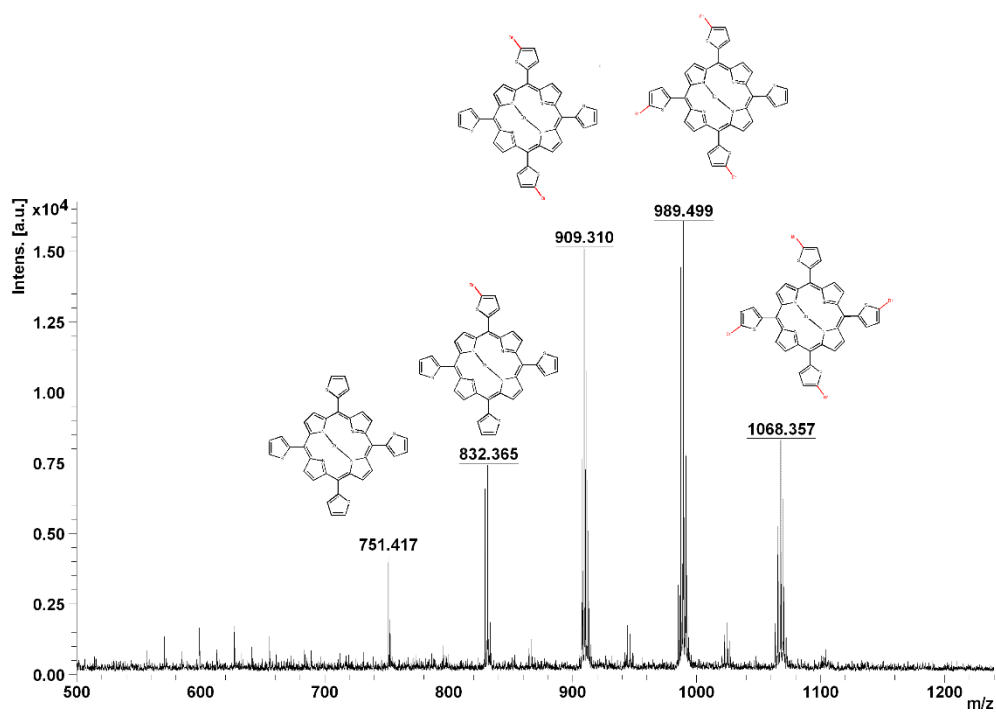
Appendix 1. 1 Mass Spectra of *Meso*-tetra(5-bromothiophen-2-yl)porphyrin



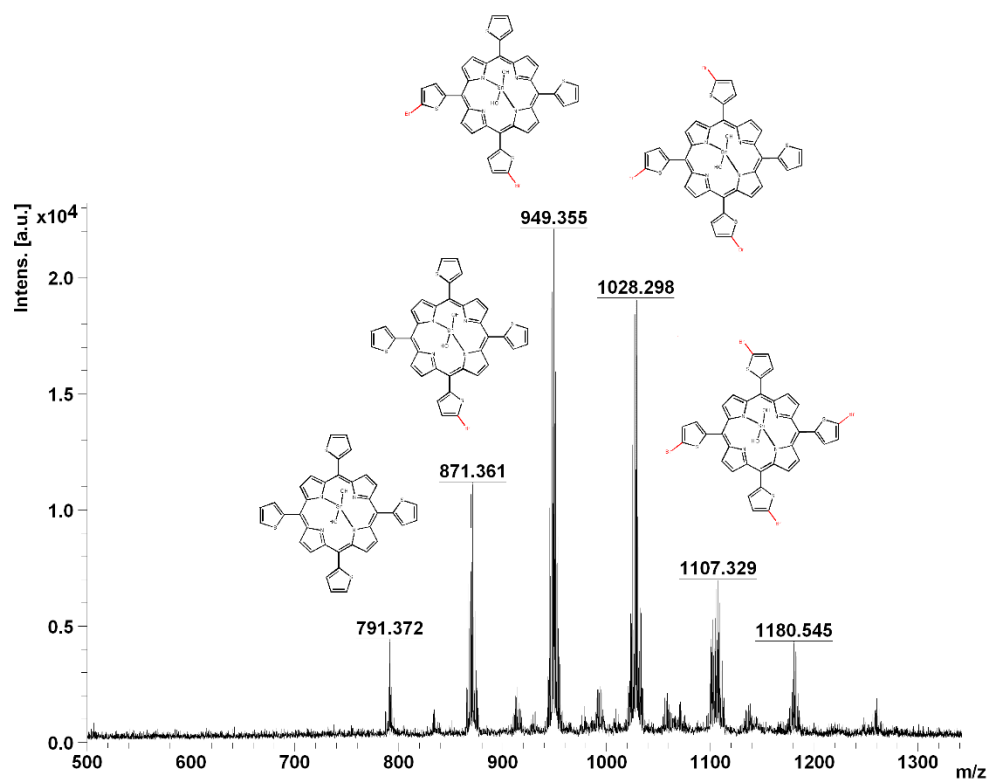
Appendix 1. 2: Mass Spectra of *Meso*-tetra(5-bromothiophen-2-yl)porphyrinato Zinc (II)



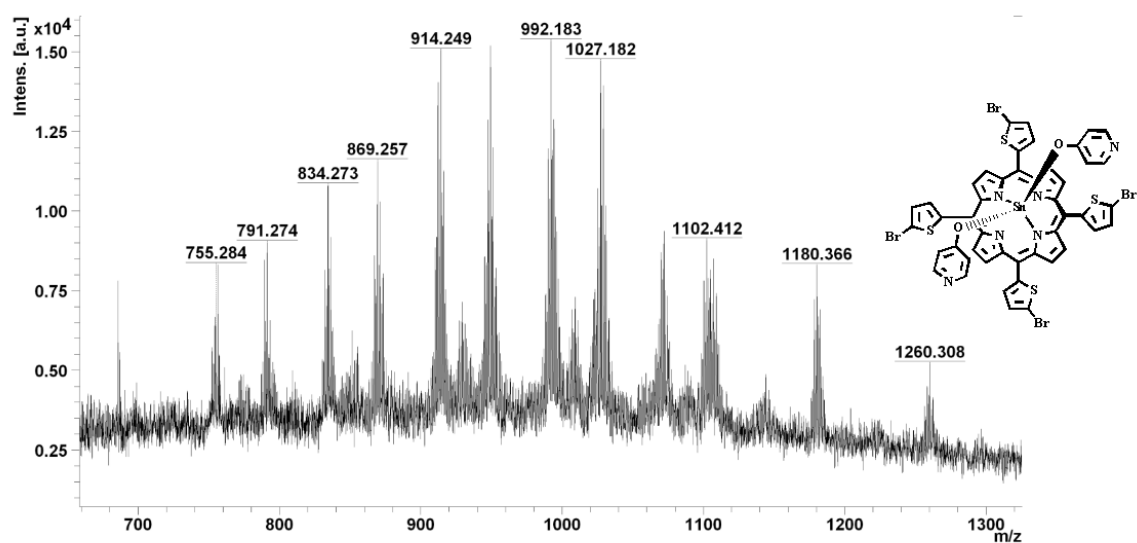
Appendix 1. 3: Mass Spectra of *Meso*-tetra(5-bromothiophen-2-yl)porphyrinato Indium (III) chloride



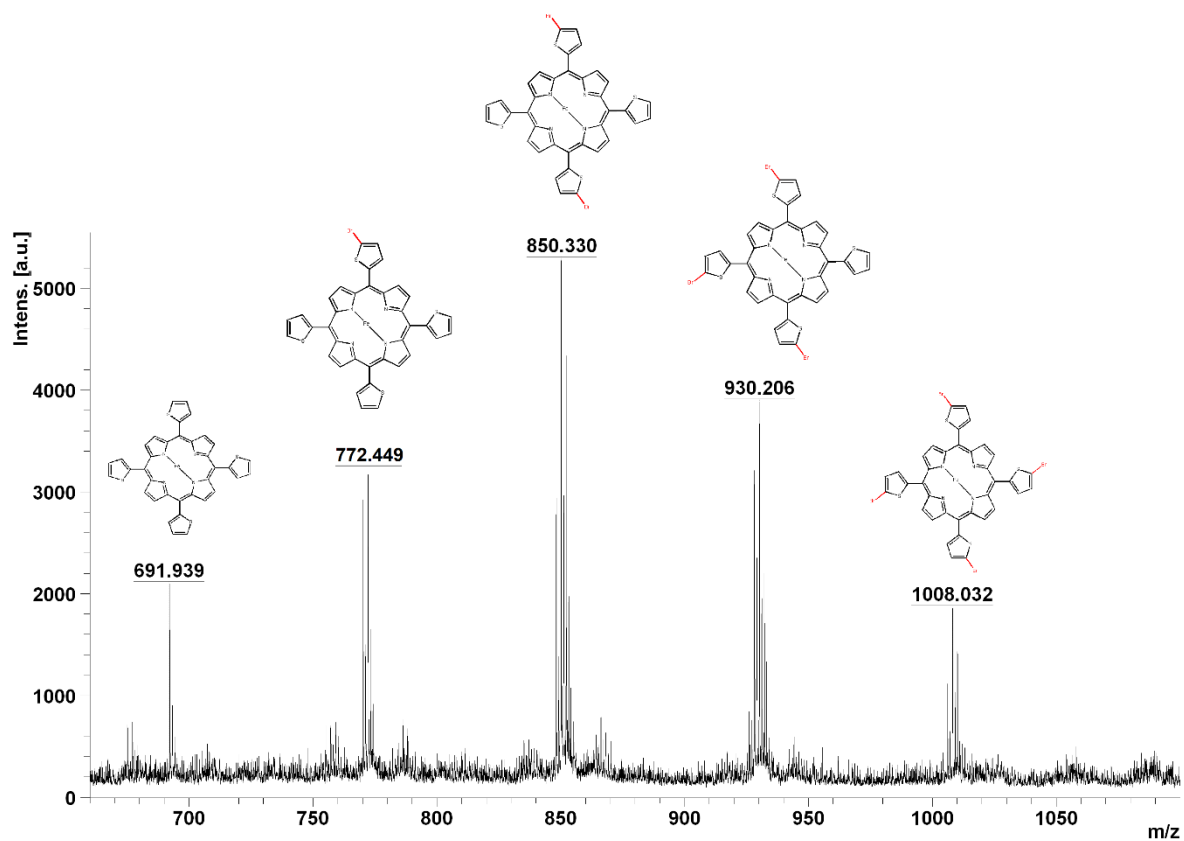
Appendix 1.4: Mass Spectra of *Meso*-tetra(5-bromothiophen-2-yl)porphyrinato Tin(IV)hydroxide



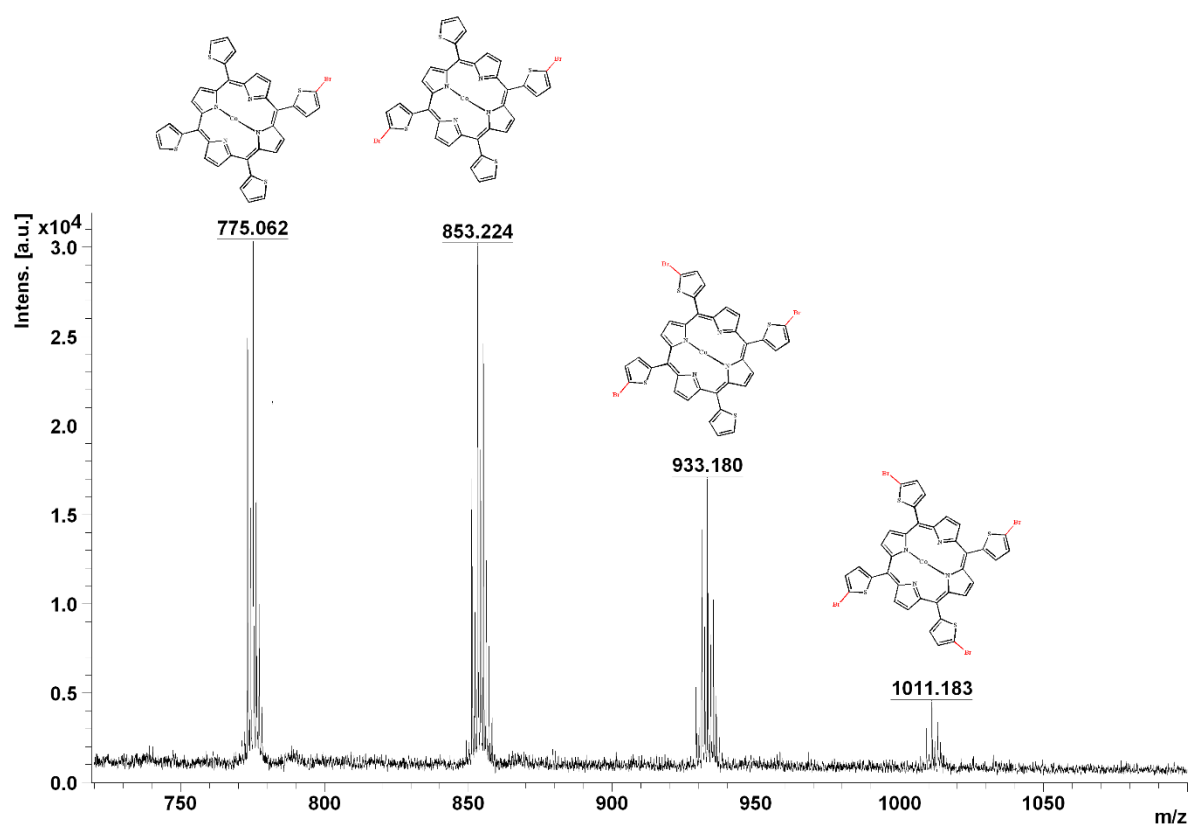
Appendix 1. 5: Mass Spectra of *Meso*-tetra(5-bromothiophen-2-yl)porphyrinato Tin(IV)dioxypyridine



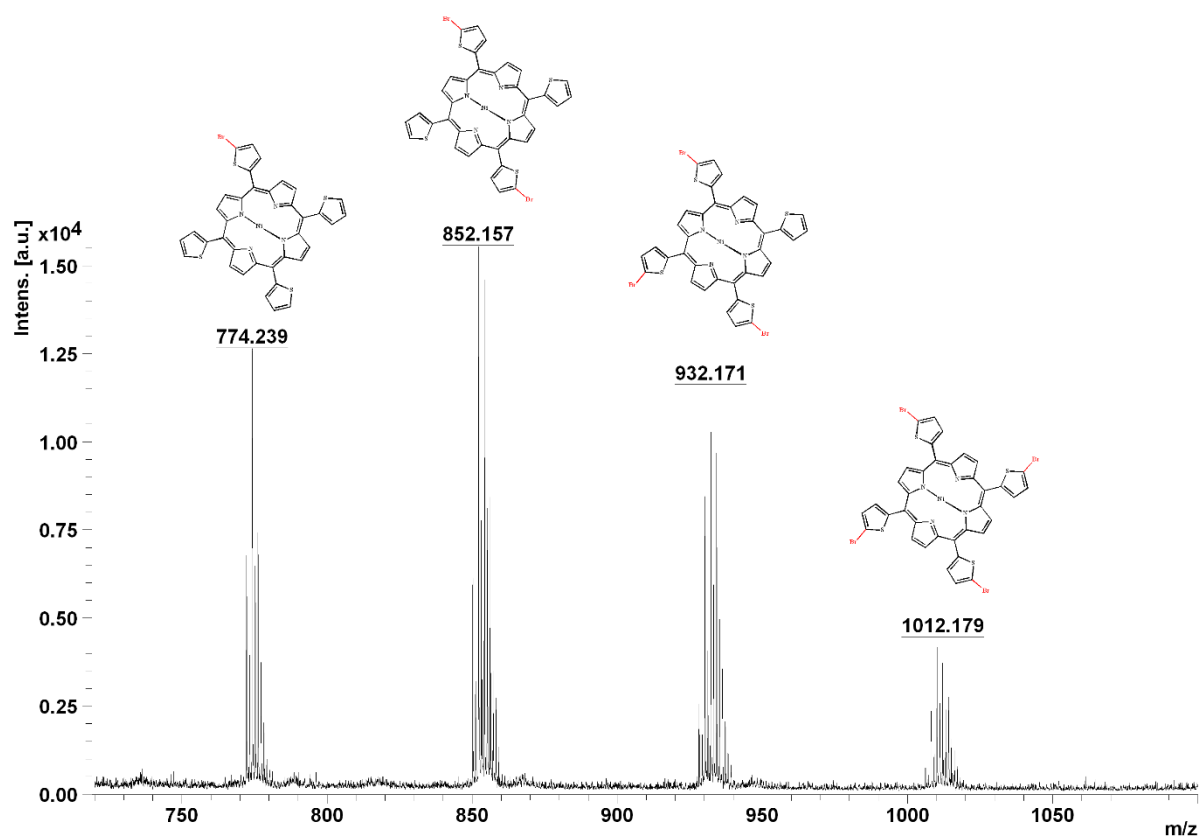
Appendix 1. 6: Mass Spectra of *Meso*-tetra(5-bromothiophen-2-yl)porphyrinato Iron(III)chloride



Appendix 1. 7: Mass Spectra of *Meso*-tetra(5-bromothiophen-2-yl)porphyrinato Cobalt(II)

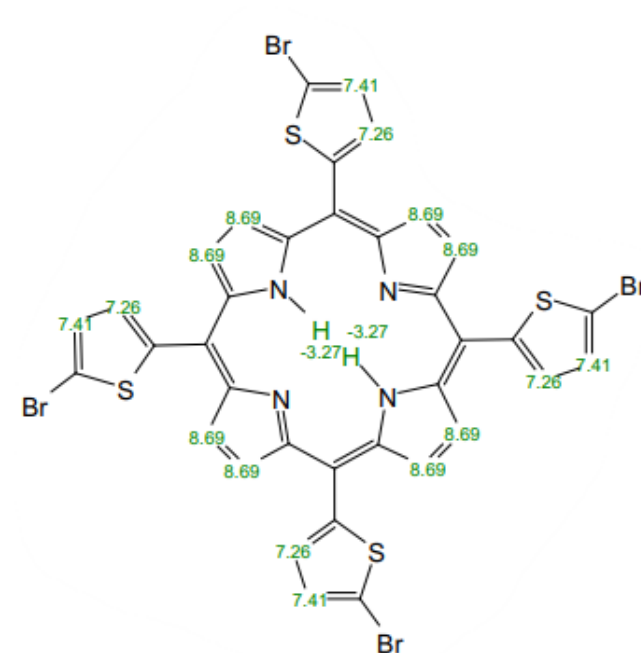
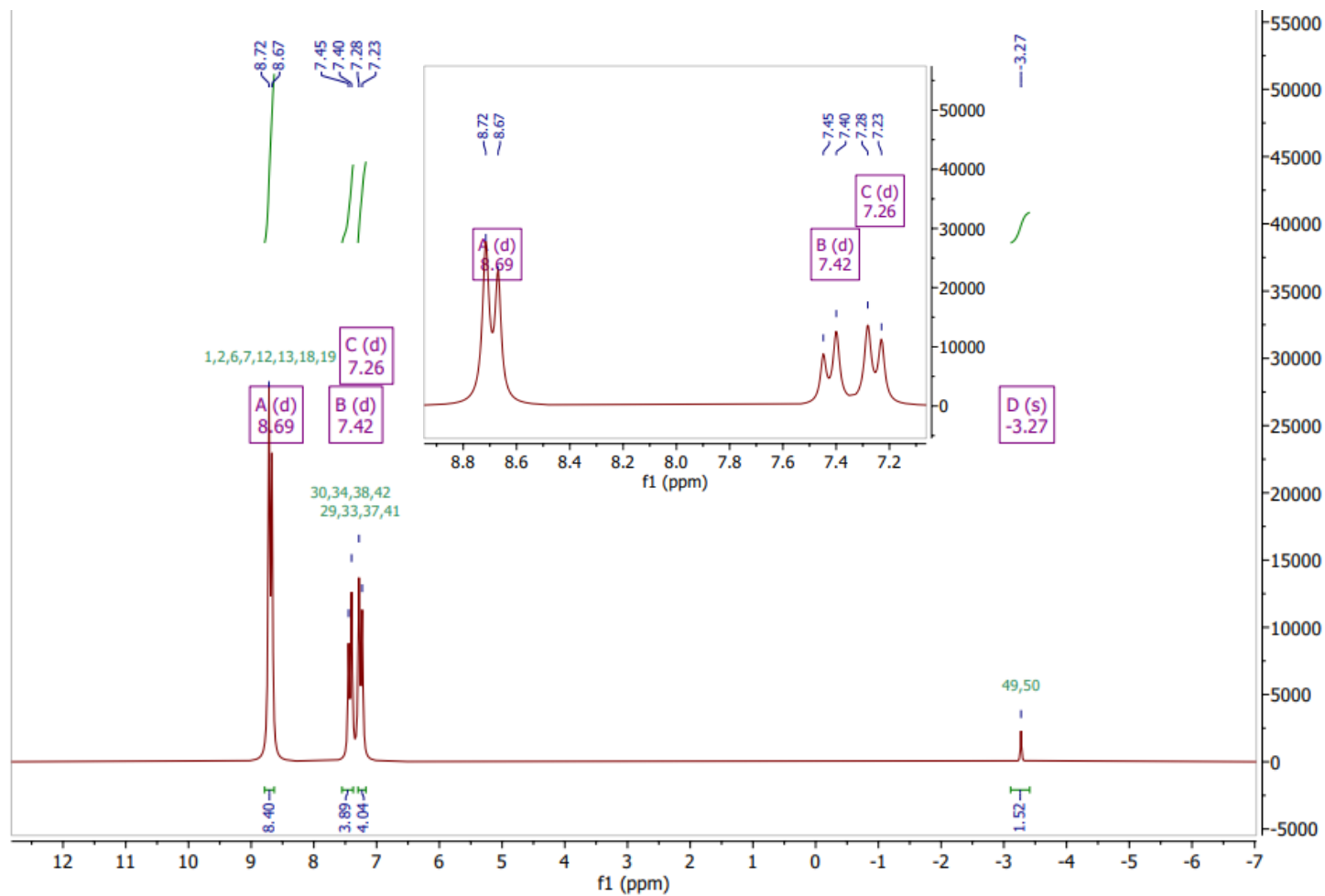


Appendix 1. 8: Mass Spectra of *Meso*-tetra(5-bromothiophen-2-yl)porphyrinato Nickel (II)

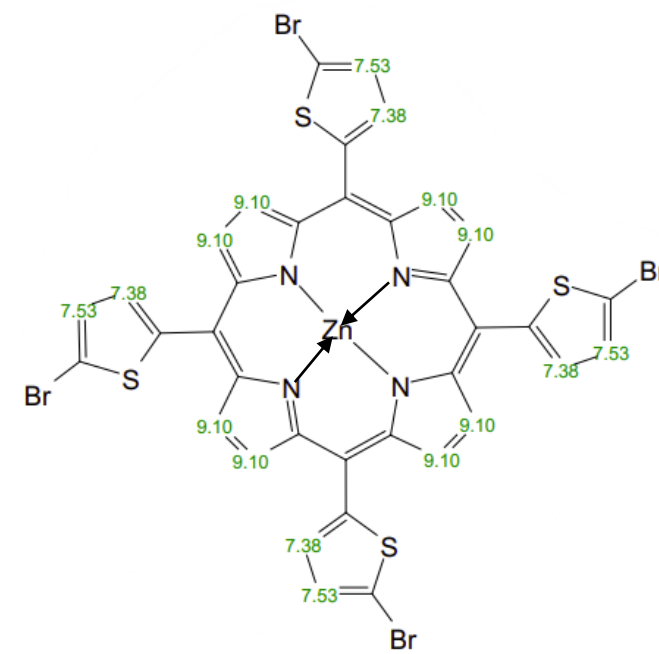
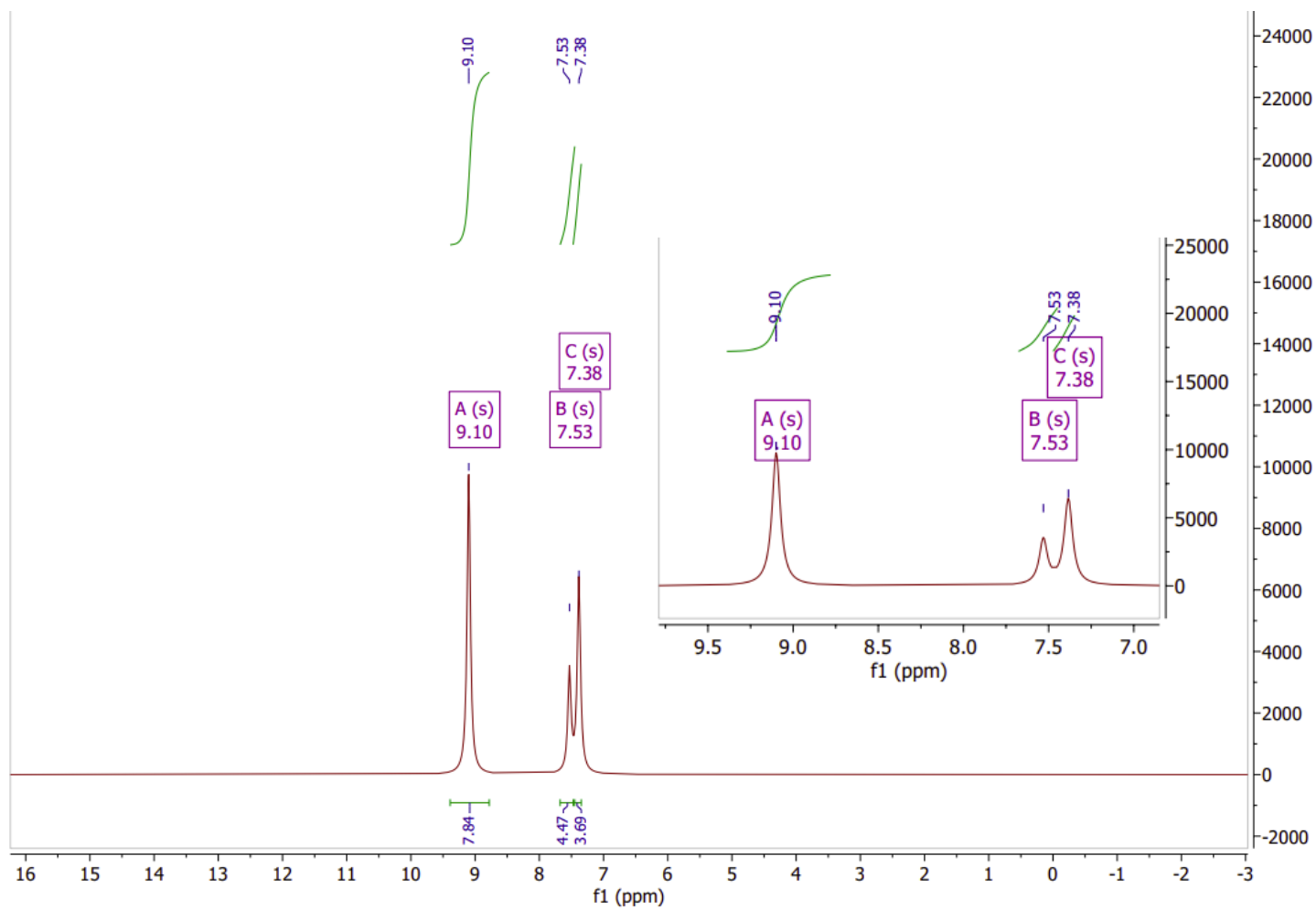


Appendix 2: ^1H NMR

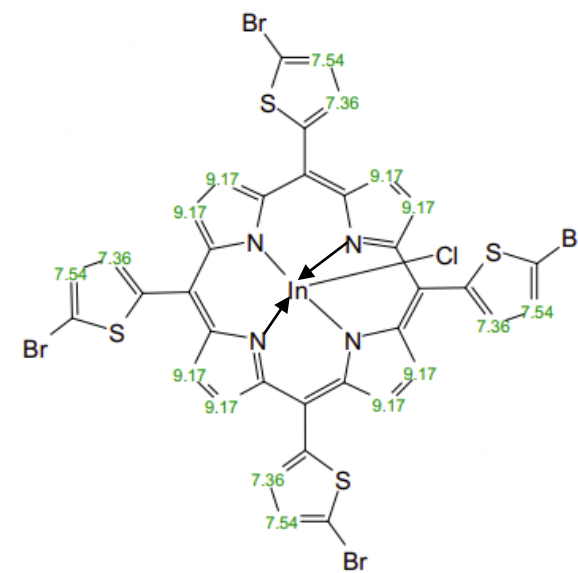
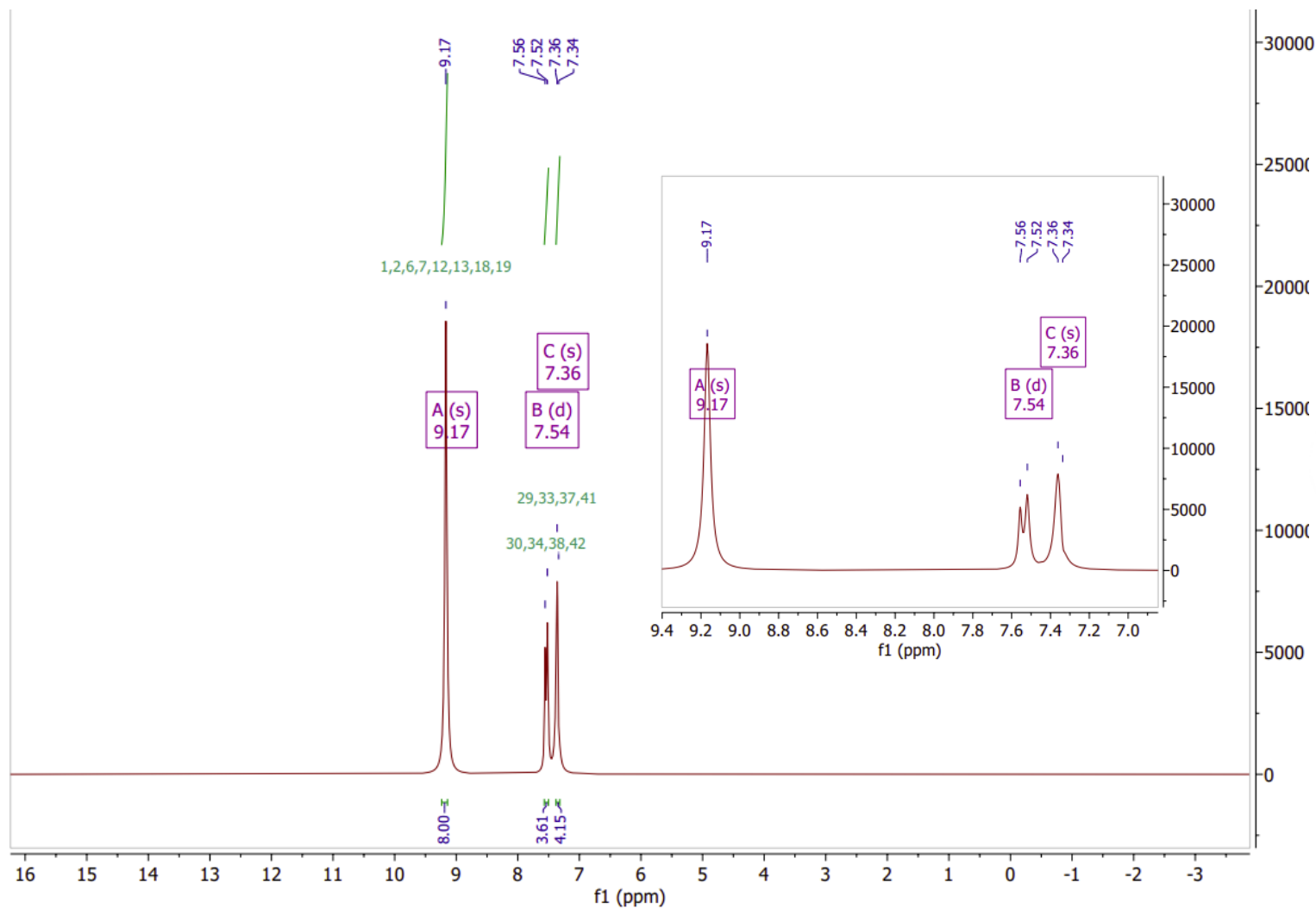
Appendix 2. 1: ^1H NMR of *Meso*-tetra(5-bromothiophen-2-yl)porphyrin



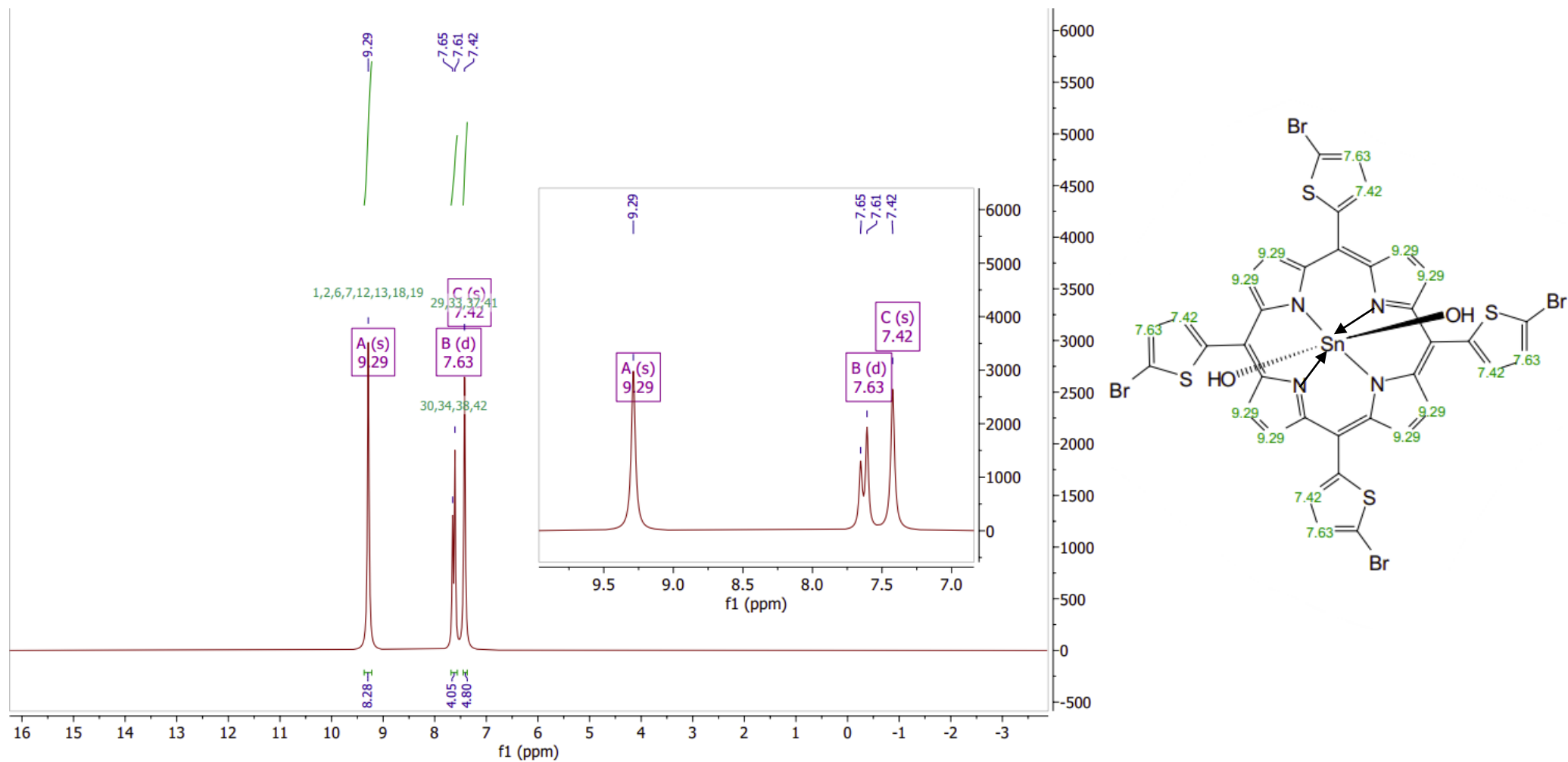
Appendix 2. 2: ^1H NMR of *Meso*-tetra(5-bromothiophen-2-yl)porphyrinato Zinc (II)



Appendix 2. 3: ^1H NMR of *Meso*-tetra(5-bromothiophen-2-yl)porphyrinato Indium (III) chloride

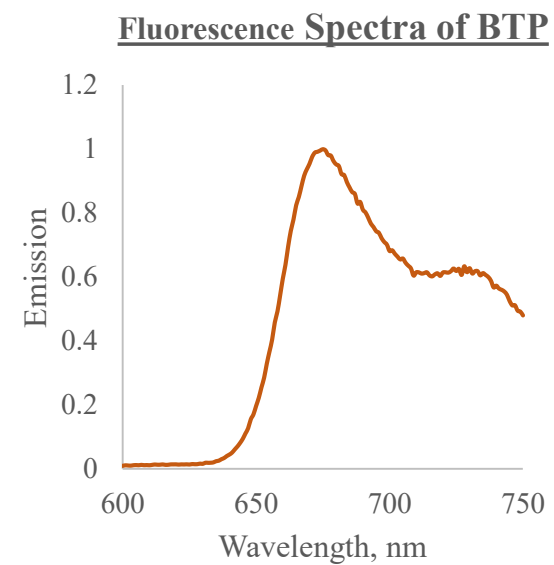
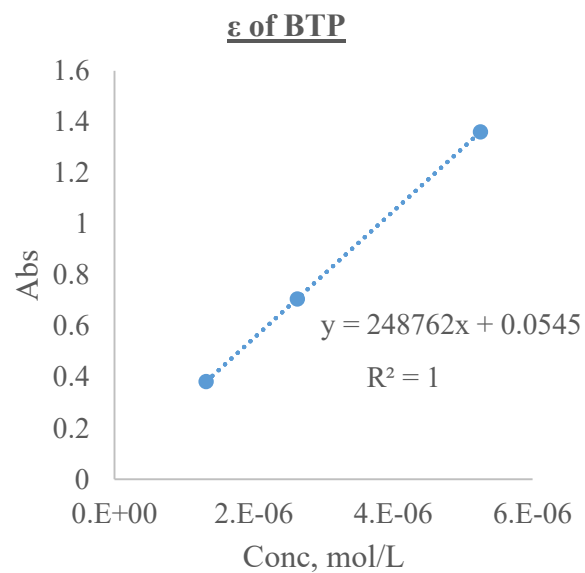
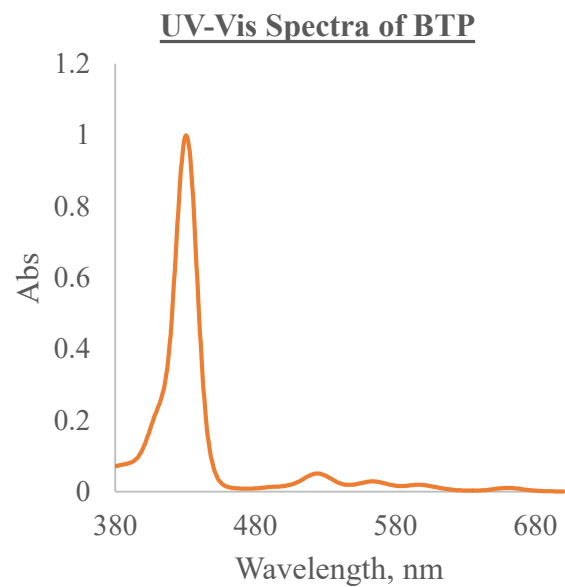


Appendix 2. 4: ^1H NMR of *Meso*-tetra(5-bromothiophen-2-yl)porphyrinato Tin(IV)hydroxide

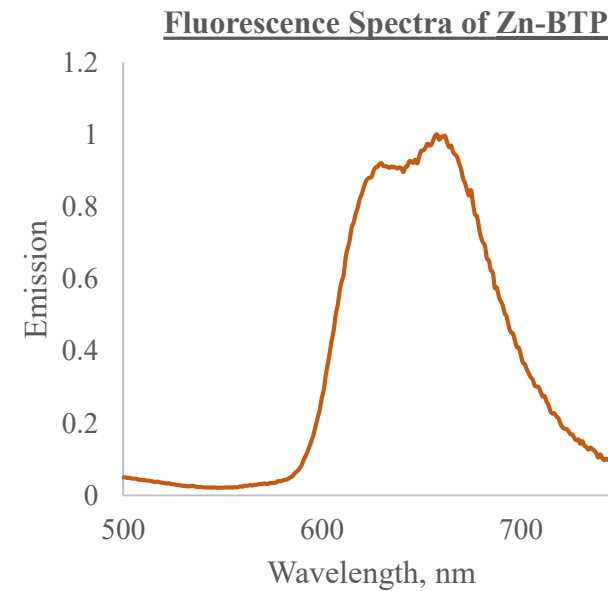
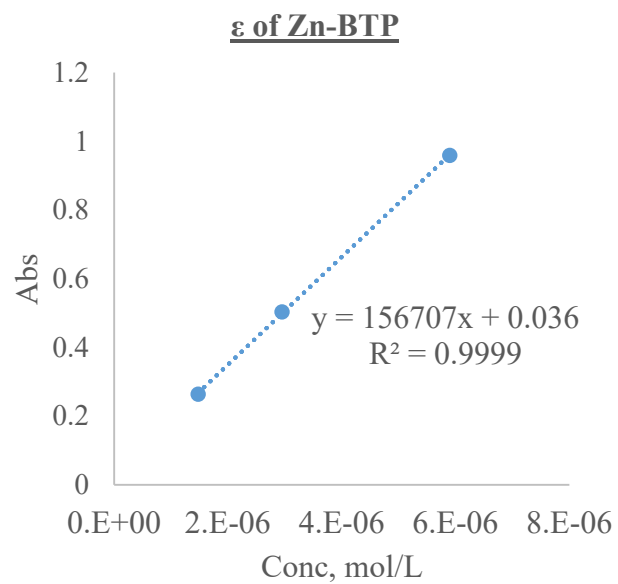
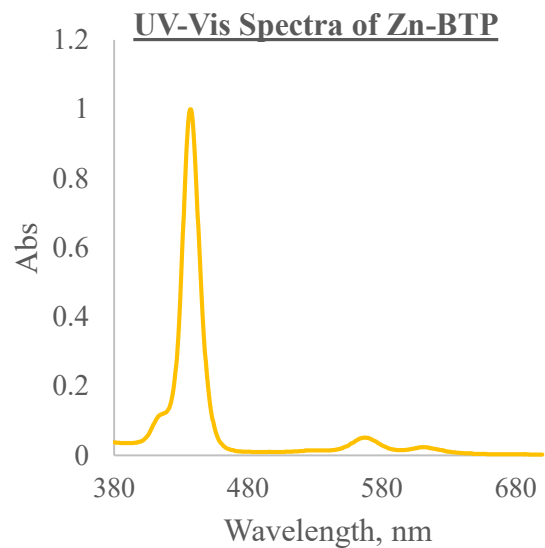


Appendix 3: Empirical Photo-physical Properties (UV-Vis, Molar Absorption Coefficient and Fluorescence)

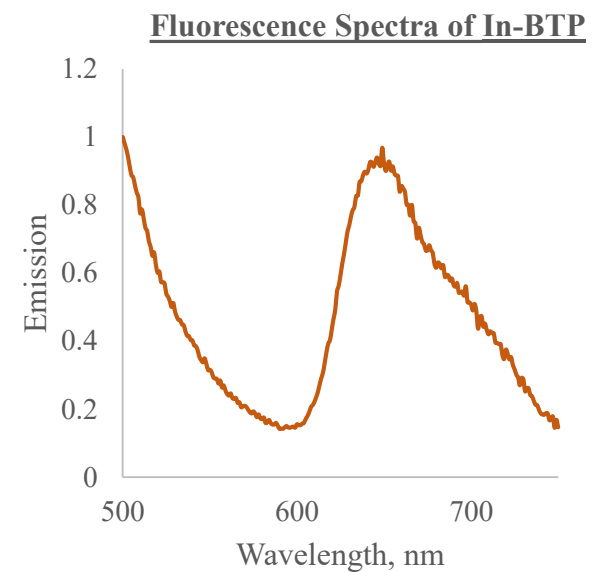
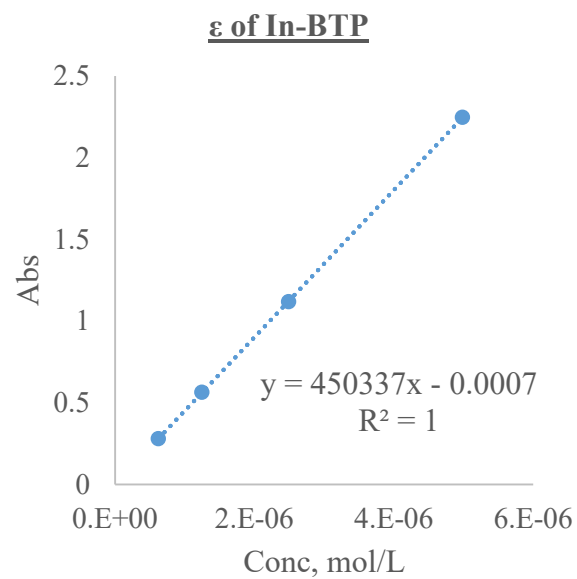
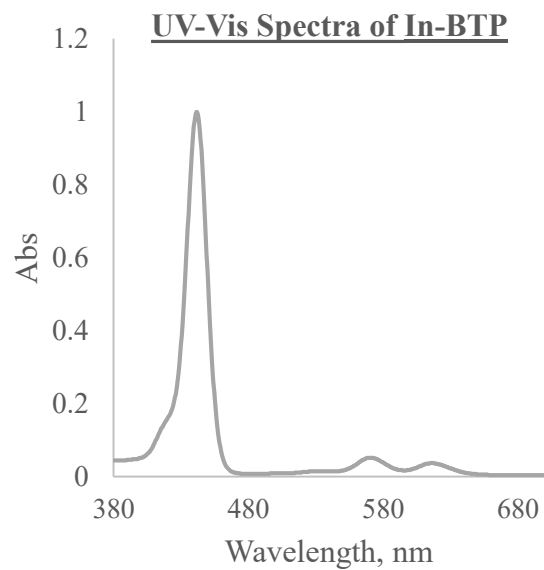
Appendix 3. 1: Empirical Photophysical Properties of *Meso*-tetra(5-bromothiophen-2-yl)porphyrin



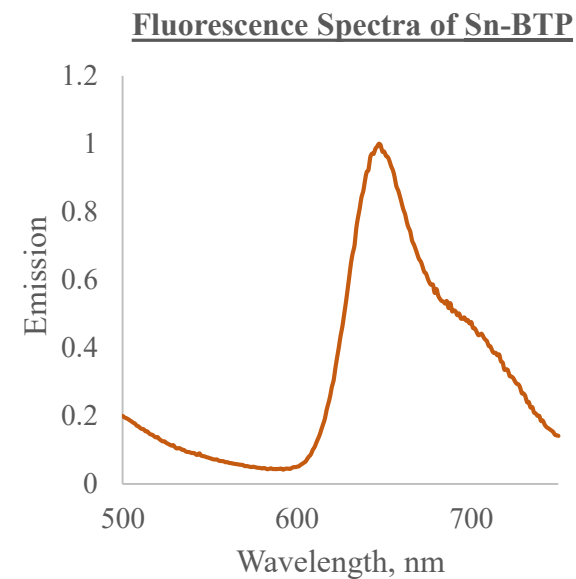
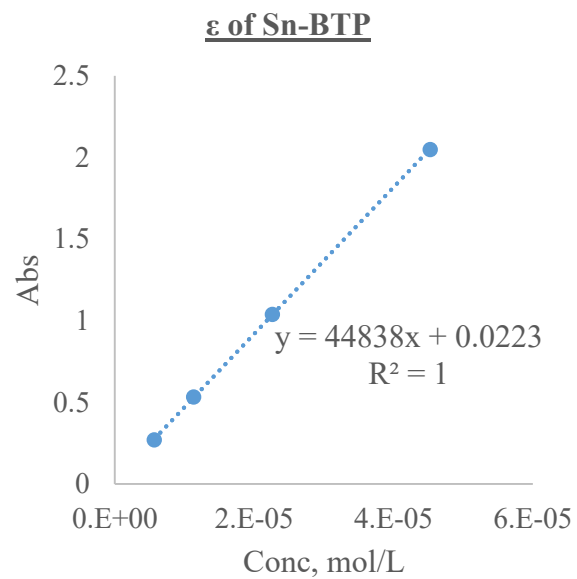
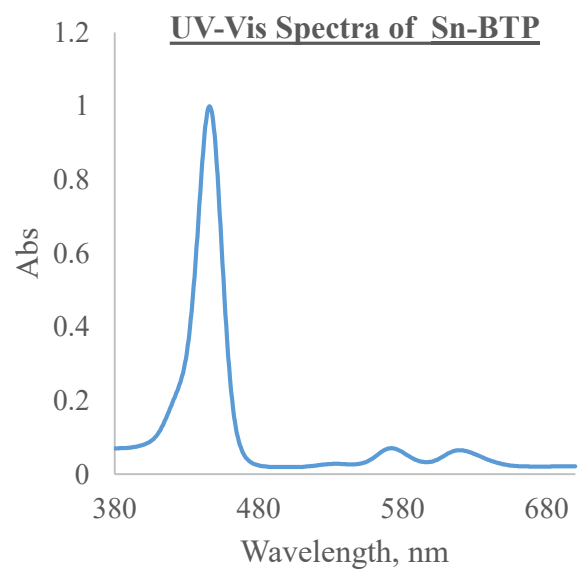
Appendix 3. 2: Empirical Photophysical Properties of *Meso*-tetra(5-bromothiophen-2-yl)porphyrinato Zinc (II)



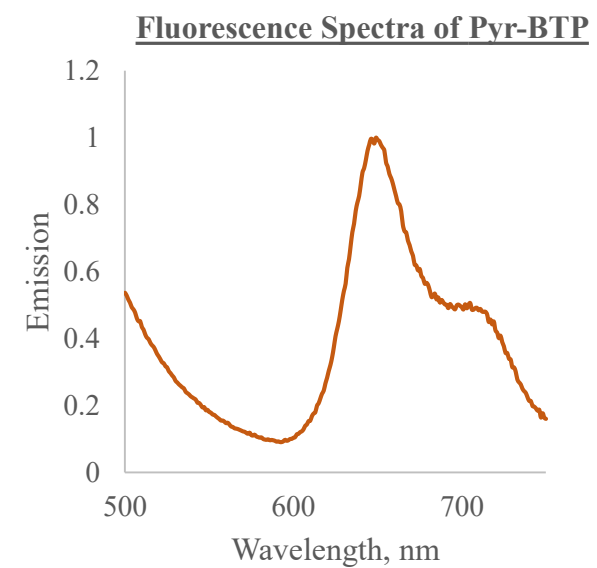
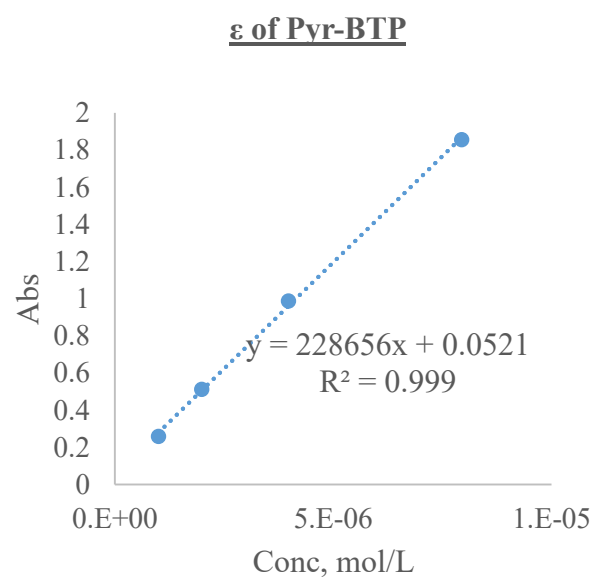
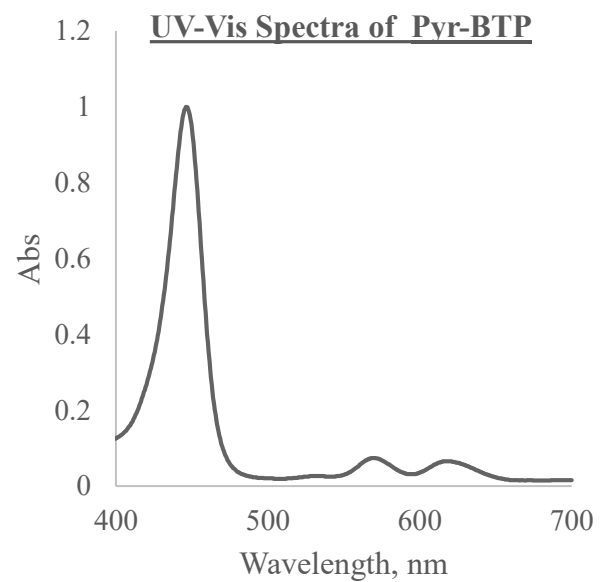
Appendix 3. 3 Empirical Photophysical Properties of *Meso*-tetra(5-bromothiophen-2-yl)porphyrinato Indium (III) chloride



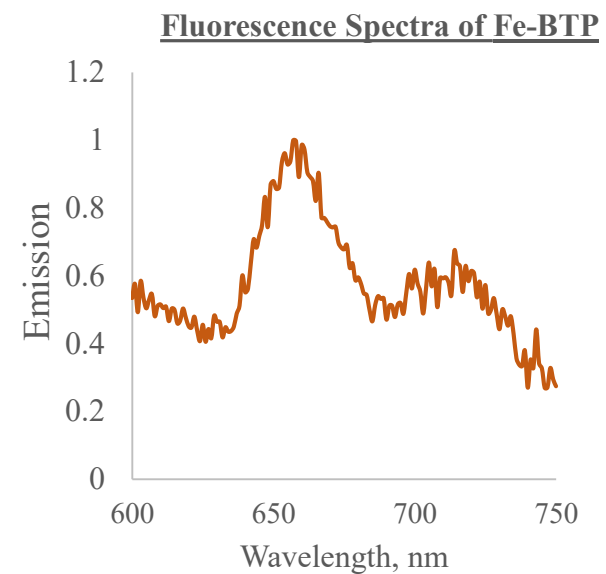
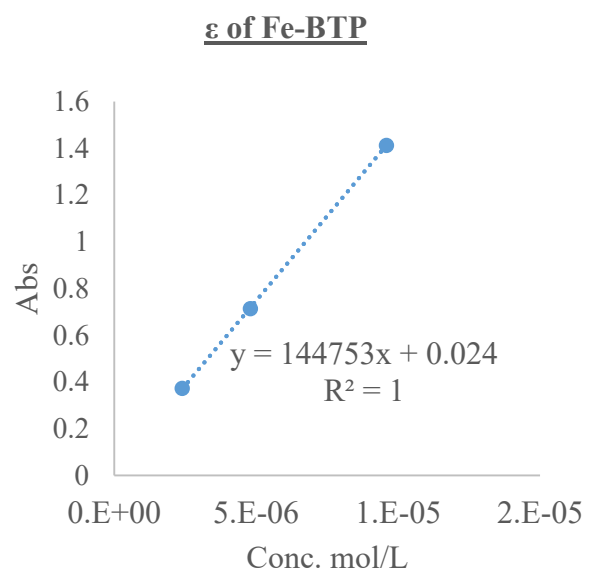
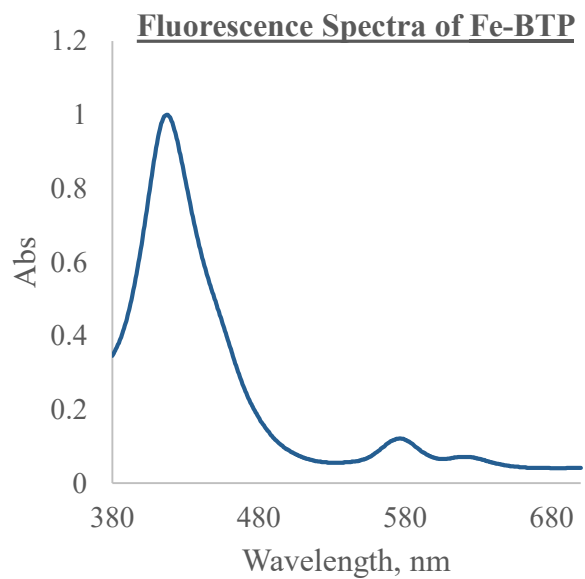
Appendix 3. 4: Empirical Photophysical Properties of *Meso*-tetra(5-bromothiophen-2-yl)porphyrinato Tin(IV)hydroxide



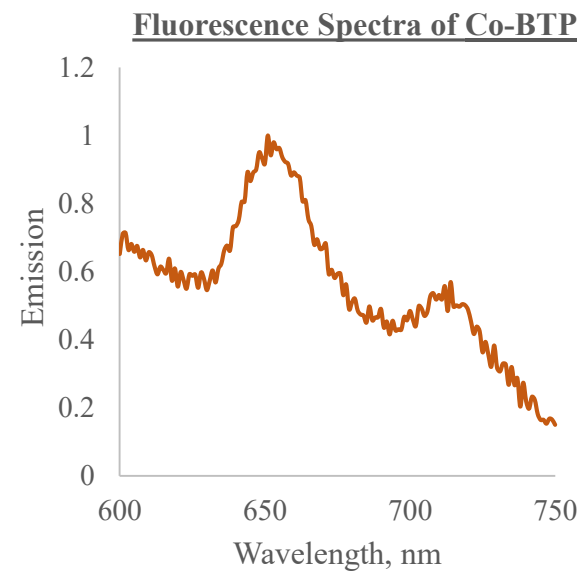
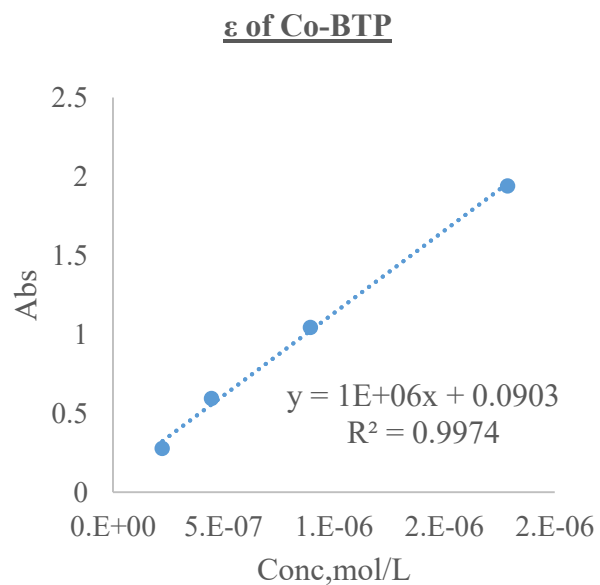
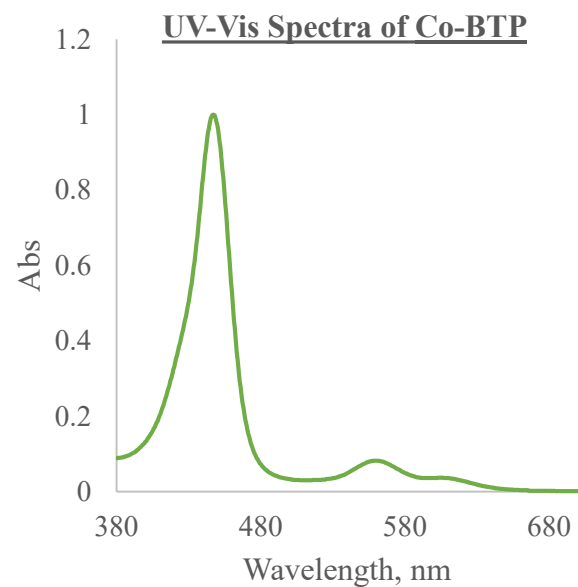
Appendix 3. 5: Empirical Photophysical Properties of *Meso*-tetra(5-bromothiophen-2-yl)porphyrinato Tin(IV)dioxypyridine



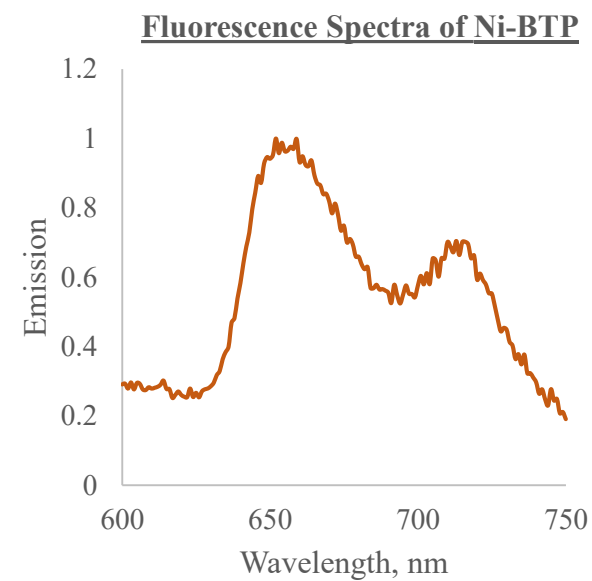
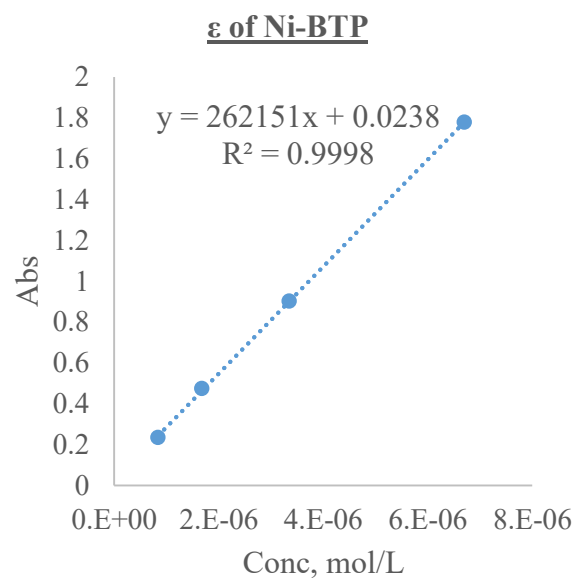
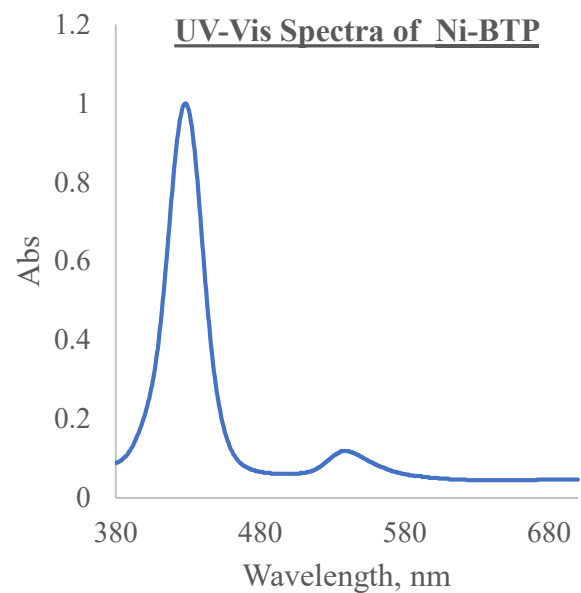
Appendix 3. 6: Empirical Photophysical Properties of *Meso*-tetra(5-bromothiophen-2-yl)porphyrinato Iron(III)chloride



Appendix 3. 7: Empirical Photophysical Properties of *Meso*-tetra(5-bromothiophen-2-yl)porphyrinato Cobalt(II)

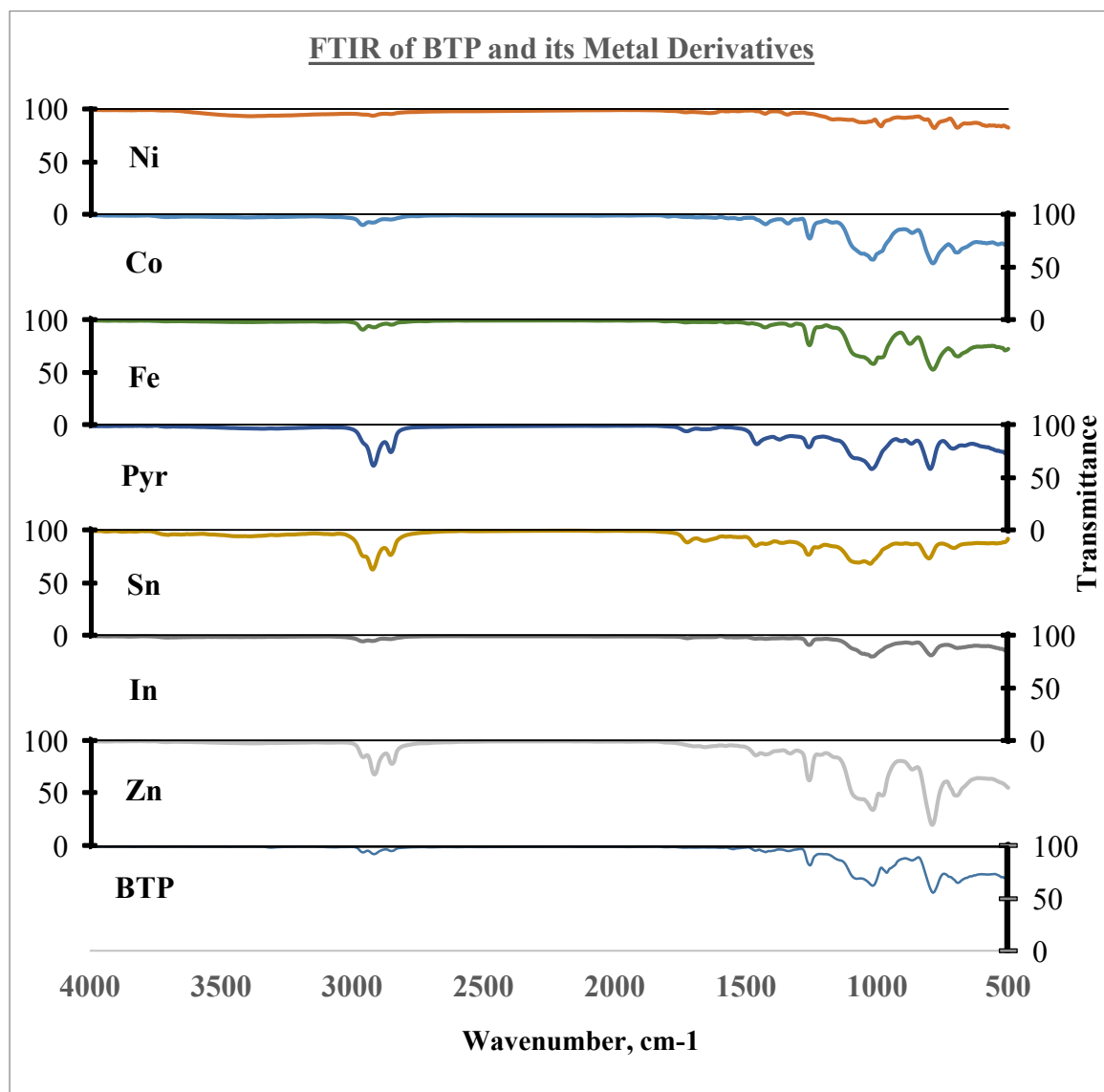


Appendix 3. 8: Empirical Photophysical Properties of *Meso*-tetra(5-bromothiophen-2-yl)porphyrinato Nickel (II)

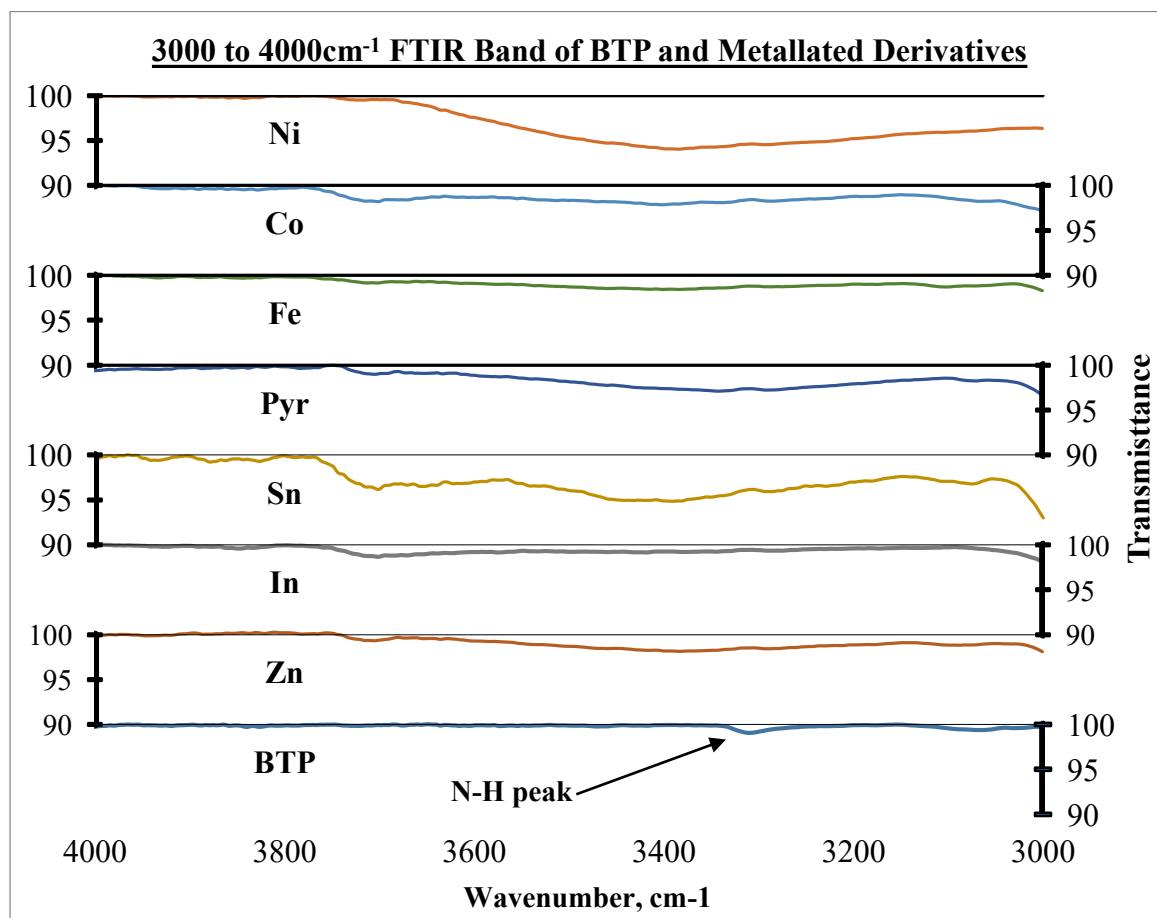


Appendix 4: Infrared Spectra

Appendix 4. 1: FTIR of *Meso*-tetra(5-bromothiophen-2-yl)porphyrin and its Metal Derivatives

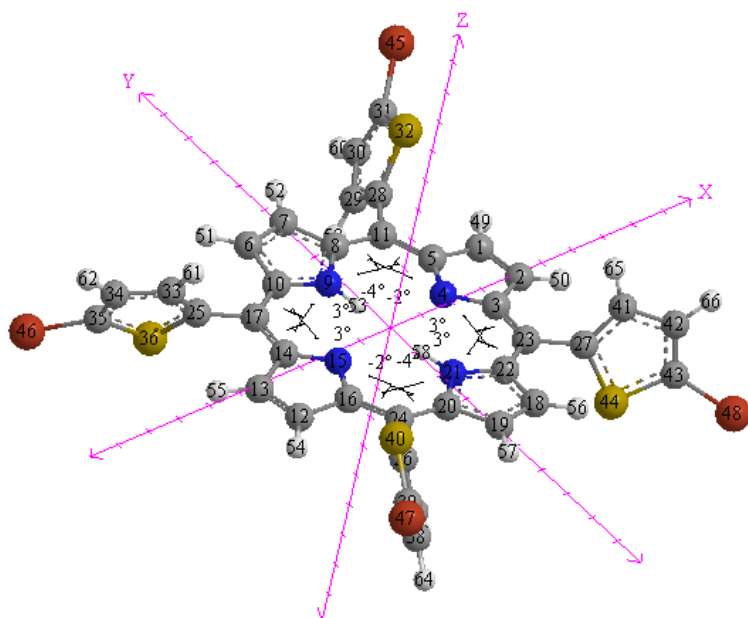


Appendix 4. 2: FTIR Spectra of *Meso*-tetra(5-bromothiophen-2-yl)porphyrin and its Metal Derivatives (3000 to 4000 cm^{-1})

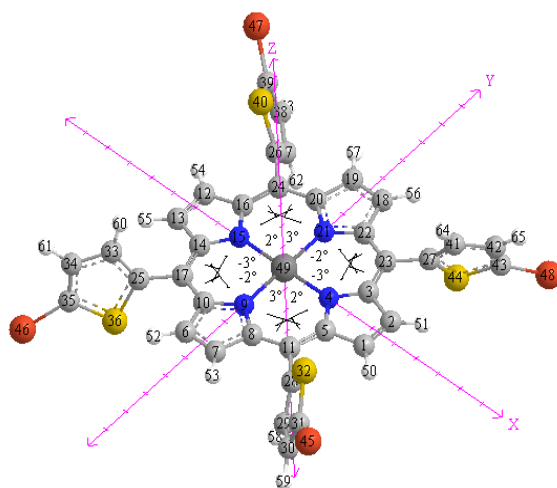


Appendix 5: Optimised Structures

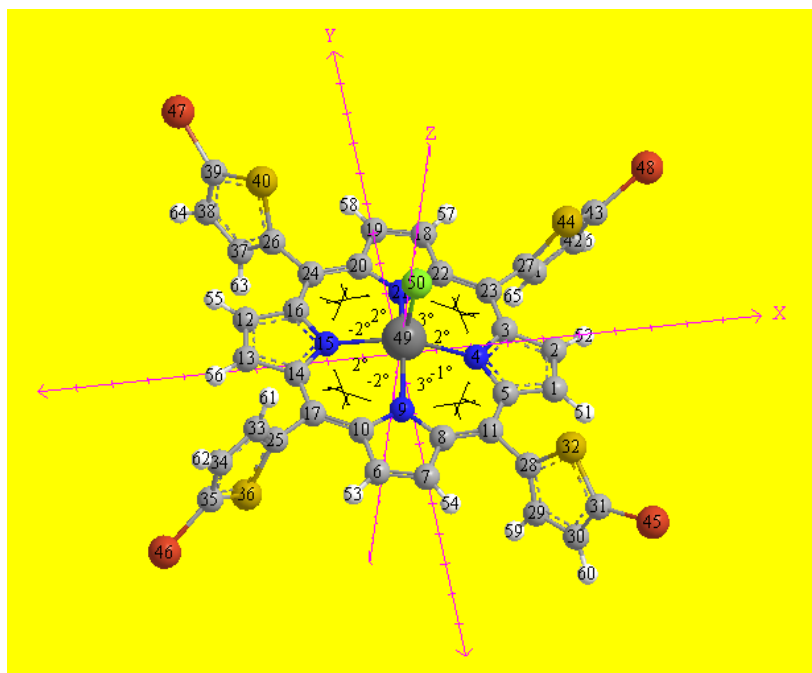
Appendix 5. 1: Optimised Structure of *Meso*-tetra(5-bromothiophen-2-yl)porphyrin



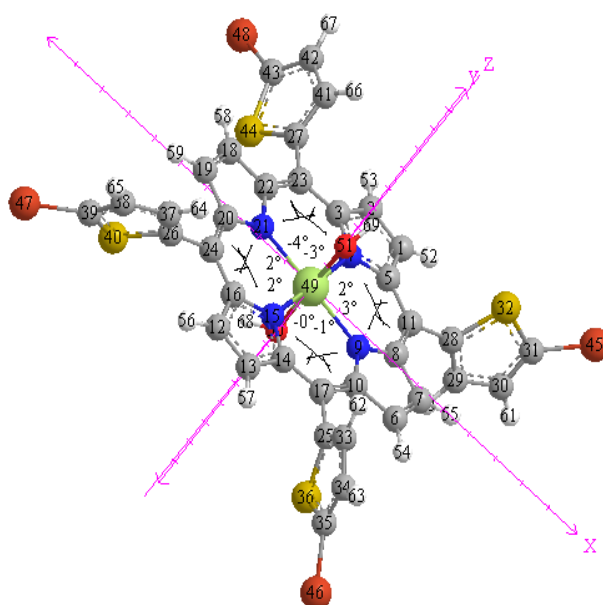
Appendix 5. 2: Optimised Structure of *Meso*-tetra(5-bromothiophen-2-yl)porphyrinato Zinc (II)



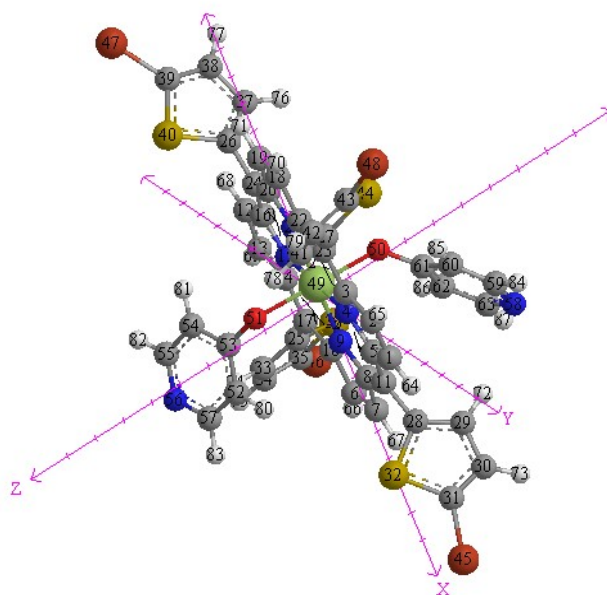
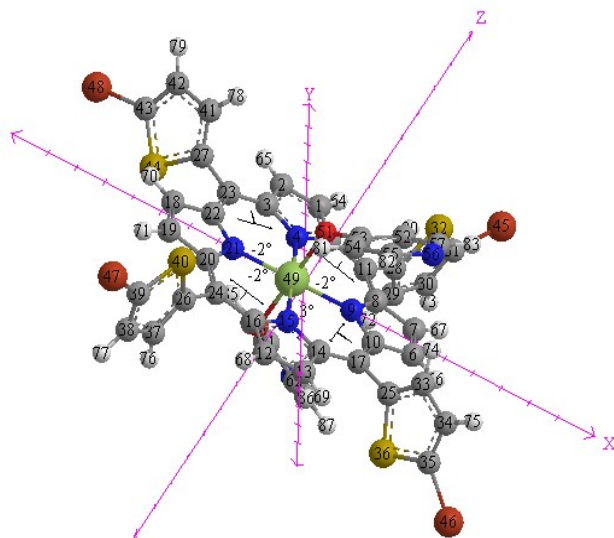
Appendix 5. 3: Optimised Structure of *Meso*-tetra(5-bromothiophen-2-yl)porphyrinato Indium (III) chloride



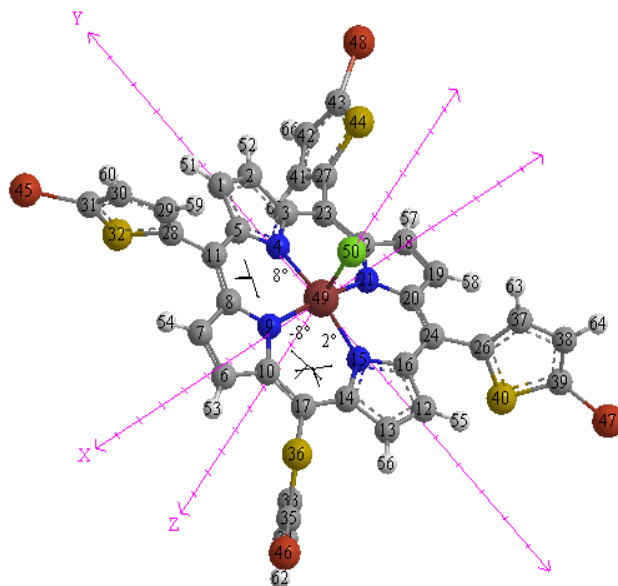
Appendix 5. 4: Optimised Structure of *Meso*-tetra(5-bromothiophen-2-yl)porphyrinato Tin(IV)hydroxide



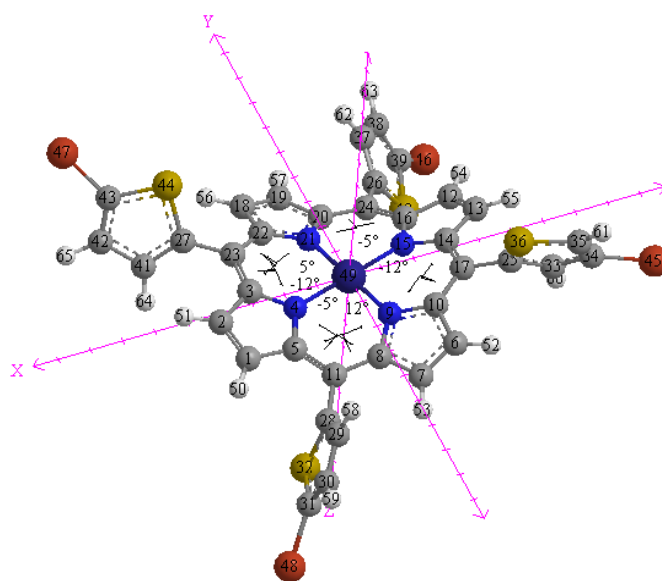
Appendix 5. 5: Optimised Structure of *Meso*-tetra(5-bromothiophen-2-yl)porphyrinato Tin(IV)dioxypyridine



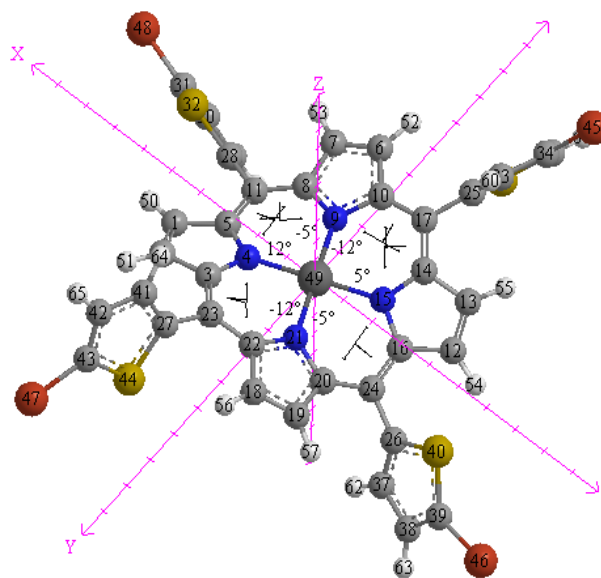
Appendix 5. 6: Optimised Structure of *Meso*-tetra(5-bromothiophen-2-yl)porphyrinato Iron(III)chloride



Appendix 5. 7: Optimised Structure of *Meso*-tetra(5-bromothiophen-2-yl)porphyrinato Cobalt(II)



Appendix 5. 8: Optimised Structure of *Meso*-tetra(5-bromothiophen-2-yl)porphyrinato Nickel
(II)



Appendix 6: Computed HOMO_LUMO Gap

Appendix 6. 1: Gouterman's Four Orbitals' Energies

| Orbitals, eV | BTP | Zn-BTP | In-BTP | Sn-BTP | Pyr-BTP | Fe-BTP | Co-BTP | Ni-BTP |
|---------------------|------------|---------------|---------------|---------------|----------------|---------------|---------------|---------------|
| HOMO_LUMO Gap | 4.6109 | 4.7014 | 4.6034 | 4.5504 | 4.5822 | 4.8521 | 4.6909 | 4.7740 |
| LUMO+1 | -1.8246 | -1.7807 | -2.5081 | -2.4504 | -2.8534 | -1.8893 | -1.7832 | -1.7165 |
| LUMO | -1.9070 | -1.7807 | -2.5163 | -2.4624 | -2.8537 | -1.8915 | -1.7867 | -1.7187 |
| HOMO | -6.4225 | -6.4465 | -7.0816 | -6.9036 | -7.3858 | -6.6457 | -6.4236 | -6.4495 |
| HOMO-1 | -6.5308 | -6.5178 | -7.1496 | -7.1099 | -7.4857 | -6.8394 | -6.5281 | -6.5338 |

Appendix 6. 2: Variations in Orbitals' Averaged Energies

| Property | BTP | Zn-BTP | In-BTP | Sn-BTP | Pyr-BTP | Fe-BTP | Co-BTP | Ni-BTP |
|-----------------------------|------------|---------------|---------------|---------------|----------------|---------------|---------------|---------------|
| Zn-LUMO Variation | 0.085037 | 0 | 0.731453 | 0.675669 | 1.072825 | 0.109664 | 0.004218 | -0.063131 |
| Extra-LUMO Variation | 0 | -0.085037 | 0.646416 | 0.590632 | 0.987788 | 0.024627 | -0.080819 | -0.148168 |
| Average LUMO | -1.865777 | -1.78074 | -2.512193 | -2.456409 | -2.853565 | -1.890404 | -1.784958 | -1.717609 |
| Average HOMO | -6.476681 | -6.482123 | -7.115614 | -7.006766 | -7.43576 | -6.74254 | -6.475864 | -6.491647 |
| Extra-HOMO Variation | 0 | 0.005442 | 0.638933 | 0.530086 | 0.95908 | 0.265859 | -0.000816 | 0.014966 |
| Zn-HOMO Variation | -0.005442 | 0 | 0.633491 | 0.524644 | 0.953638 | 0.260417 | -0.006259 | 0.009524 |

Appendix 7: Computed Photophysical Properties of *Meso*-tetra(5-bromothiophen-2-yl)porphyrin and its Metal Analogues

Appendix 7. 1: Computed photo-physical properties of *Meso*-tetra(5-bromothiophen-2-yl)porphyrin

| Molecule | Band | State | f, oscillator strength | Calculated | | Empirical | | Wavefunction | | Probability (%) |
|------------|------|--------|------------------------------|------------|------------------|-----------|------------------|--------------|----------|-----------------|
| | | | | nm | cm ⁻¹ | nm | cm ⁻¹ | HOMO(□) | -LUMO(□) | |
| BTP | Q | 1 | 0.0018 | 589.1 | 16,975.05 | 660.5 | 15,140.05 | a(-1) | a | 45 |
| | | | | | | 596.5 | 16,764.46 | s | s(+1) | 52 |
| | Q | 2 | 0.0252 | 537.47 | 18,605.69 | 563 | 17,761.99 | a(-1) | s(+1) | 43 |
| | | | | | | 524 | 19,083.97 | s | a | 54 |
| | B | 3 | 1.3746 | 372.86 | 26,819.72 | | | a(-1) | a | 48 |
| | | | | | | | | a(-1) | s(+1) | 2 |
| | | | | | | | | s(-1) | s(+1) | 38 |
| | | | | | | 430.5 | 23,228.80 | a(-1) | a | 2 |
| | | | | | | | | a(-1) | s(+1) | 53 |
| | | | | | | | | s | a | 43 |
| B | 4 | 1.7717 | 362.39 | 27,594.58 | | | s | s(+1) | 2 | |

Appendix 7. 2: Computed photo-physical properties of *Meso*-tetra(5-bromothiophen-2-yl)porphyrinato Zinc(II)

| Molecule | Band | State | f, oscillator strength | Calculated | | Empirical | | Wavefunction | | Probability (%) |
|---------------|------|-------|------------------------------|------------|------------------|-----------|------------------|--------------|----------|-----------------|
| | | | | nm | cm ⁻¹ | nm | cm ⁻¹ | HOMO() | -LUMO() | |
| Zn-BTP | Q | 1 | 0.0008 | 539.32 | 18,541.87 | 611 | 16,366.61 | a | a | 45 |
| | | | | | | | | s(-1) | s(+1) | 52 |
| | Q | 2 | 0.0008 | 539.32 | 18,541.87 | 567 | 17,636.68 | a | s(+1) | 43 |
| | | | | | | | | s(-1) | a | 54 |
| | | | | | | | | s(-1) | s | 38 |
| | | | | | | | | s(-1) | a(+1) | 12 |
| | B | 3 | 1.5778 | 361.88 | 27,633.47 | 437 | 17,636.68 | a | s | 11 |
| | | | | | | | | a | a(+1) | 34 |
| | | | | | | | | s(-1) | s | 12 |
| | | | | | | | | s(-1) | a(+1) | 38 |
| | | | | | | | | a | s | 34 |
| | | | | | | | | a | a(+1) | 11 |

Appendix 7. 3: Computed photo-physical properties of *Meso*-tetra(5-bromothiophen-2-yl)porphyrinato Indium (III) chloride

| Molecule | Band | State | f, oscillator strength | Calculated | | Empirical | | Wavefunction | | Probability (%) |
|---------------|------|-------|------------------------------|------------|------------------|-----------|------------------|--------------|----------|-----------------|
| | | | | nm | cm ⁻¹ | nm | cm ⁻¹ | HOMO() | -LUMO() | |
| In-BTP | Q | 1 | 0.0074 | 556.61 | 17,965.90 | 616 | 16,233.77 | a(-1) | s | 3 |
| | | | | | | | | a(-1) | a(+1) | 44 |
| | | | | | | | | s | s | 50 |
| | | | | | | | | s | a(+1) | 3 |
| | Q | 2 | 0.0064 | 556.23 | 17,978.17 | 570.5 | 17,528.48 | a(-1) | s | 45 |
| | | | | | | | | a(-1) | a(+1) | 2 |
| | | | | | | | | s | s | 3 |
| | | | | | | | | s | a(+1) | 49 |
| | B | 3 | 1.5509 | 369.24 | 27,082.66 | 441.5 | 22,650.06 | a(-1) | s | 12 |
| | | | | | | | | a(-1) | a(+1) | 39 |
| | | | | | | | | s | s | 34 |
| | | | | | | | | s | a(+1) | 11 |
| | B | 4 | 1.5559 | 368.56 | 27,132.62 | | | a(-1) | s | 39 |
| | | | | | | | | a(-1) | a(+1) | 12 |
| | | | | | | | | s | s | 11 |
| | | | | | | | | s | a(+1) | 35 |

Appendix 7. 4: Computed photo-physical properties of *Meso*-tetra(5-bromothiophen-2-yl)porphyrinato Tin(IV)hydroxide

| Molecule | Band | State | f, oscillator strength | Calculated | | Empirical | | Wavefunction | | Probability (%) |
|----------|------|-------|------------------------------|------------|------------------|-----------|------------------|--------------|----------|-----------------|
| | | | | nm | cm ⁻¹ | nm | cm ⁻¹ | HOMO() | -LUMO() | |
| Sn-BTP | Q | 1 | 0.0227 | 565.44 | 17,685.34 | 620 | 16,129.03 | a(-1) | s | 6 |
| | | | | | | | | a(-1) | a(+1) | 35 |
| | | | | | | | | s | s | 49 |
| | | | | | | | | s | a(+1) | 9 |
| | Q | 2 | 0.0203 | 564.4 | 17,717.93 | 572.5 | 17,467.25 | a(-1) | s | 36 |
| | | | | | | | | a(-1) | a(+1) | 6 |
| | | | | | | | | s | a(+1) | 9 |
| | | | | | | | | s | s | 48 |
| | B | 3 | 1.4073 | 377.29 | 26,504.81 | 446 | 22,421.52 | a(-1) | s | 3 |
| | | | | | | | | a(-1) | a(+1) | 52 |
| | | | | | | | | s | s | 36 |
| | | | | | | | | s | a(+1) | 2 |
| | B | 4 | 1.4494 | 376.11 | 26,587.97 | | | a(-1) | s | 52 |
| | | | | | | | | a(-1) | a(+1) | 3 |
| | | | | | | | | s | s | 2 |
| | | | | | | | | s | a(+1) | 37 |

Appendix 7. 5: Computed photo-physical properties of *Meso*-tetra(5-bromothiophen-2-yl)porphyrinato Tin(IV)dioxypyridine

| Molecule | Band | State | f, oscillator strength | Calculated | | Empirical | | Wavefunction | | Probability (%) |
|----------|------|-------|------------------------------|------------|------------------|-----------|------------------|--------------|----------|-----------------|
| | | | | nm | cm ⁻¹ | nm | cm ⁻¹ | HOMO() | -LUMO() | |
| Pyr-BTP | Q | 1 | 0.0089 | 565.44 | 17,685.34 | | | a(-1) | s(+1) | 46 |
| | | | | | | 616 | 16,233.77 | s | a | 53 |
| | Q | 2 | 0.0087 | 564.4 | 17,717.93 | | | a(-1) | a | 46 |
| | | | | | | | | s | s(+1) | 53 |
| | Q | 5 | 0.1518 | 406.85 | 24,579.08 | | | a(-1) | s(+1) | 12 |
| | | | | | | 569 | 17,574.69 | s | a | 16 |
| | Q | 6 | 0.1578 | 406.57 | 24,596.01 | | | a(-1) | a | 12 |
| | | | | | | | | s | s(+1) | 17 |
| | B | 7 | 1.2004 | 367.08 | 27,242.02 | | | a(-1) | a | 40 |
| | | | | | | 442.5 | 22,598.87 | s | s(+1) | 29 |
| | B | 8 | 1.2208 | 366.63 | 27,275.45 | | | a(-1) | s(+1) | 40 |
| | | | | | | | | s | a | 29 |

Appendix 7. 6: Computed photo-physical properties of *Meso*-tetra(5-bromothiophen-2-yl)porphyrinato Iron(III)chloride

| Molecule | Band | State | f, oscillator strength | Calculated | | Empirical | | Wavefunction | | Probability (%) |
|----------|------|-------|------------------------------|------------|------------------|-----------|------------------|--------------|----------|-----------------|
| | | | | nm | cm ⁻¹ | nm | cm ⁻¹ | HOMO() | -LUMO() | |
| Fe-BTP | Q | 16 | 0.0036 | 529.8 | 18,875.05 | 619.5 | 16,142.05 | s(-1) | s(+1) | 24 |
| | | | | | | | | a | s(+1) | 58 |
| | Q | 17 | 0.0014 | 528.81 | 18,910.38 | 576 | 17,361.11 | s(-1) | s(+1) | 50 |
| | | | | | | | | a | s(+1) | 29 |
| | B | 31 | 0.5684 | 382.06 | 26,173.90 | | | s(-1) | s(+1) | 3 |
| | | | | | | | | a | s(+1) | 21 |
| | B | 39 | 0.6773 | 343.25 | 29,133.28 | 417.5 | 23,952.10 | s(-1) | s(+1) | 12 |
| | | | | | | | | a | s(+1) | 9 |
| | B | 40 | 0.5828 | 342.07 | 29,233.78 | | | s(-1) | s(+1) | 15 |
| | | | | | | | | a | s(+1) | 5 |

Appendix 7. 7: Computed photo-physical properties of *Meso*-tetra(5-bromothiophen-2-yl)porphyrinato Cobalt(II)

| Molecule | Band | State | f, oscillator strength | Calculated | | Empirical | | Wavefunction | | Probability (%) |
|----------|------|--------|------------------------|------------|------------------|-----------|------------------|--------------|----------|-----------------|
| | | | | nm | cm ⁻¹ | nm | cm ⁻¹ | HOMO() | -LUMO() | |
| Co-BTP | Q | 12 | 0.0001 | 592.57 | 16,875.64 | 605.5 | 16,515.28 | s(-1) | a | 19 |
| | | | | | | | | s(-1) | s(+1) | 39 |
| | | | | | | | | a | a | 31 |
| | | | | | | | | a | s(+1) | 11 |
| | | | | | | | | s(-1) | a | 39 |
| | | | | | | | | s(-1) | s(+1) | 18 |
| | Q | 13 | 0.0001 | 592.25 | 16,884.76 | 560 | 17,857.14 | a | a | 11 |
| | | | | | | | | a | s(+1) | 31 |
| | | | | | | | | s(-1) | a | 7 |
| | | | | | | | | s(-1) | s(+1) | 35 |
| | | | | | | | | a | a | 41 |
| | | | | | | | | a | s(+1) | 9 |
| | Q | 14 | 0.0062 | 533.34 | 18,749.77 | 560 | 17,857.14 | s(-1) | a | 35 |
| | | | | | | | | s(-1) | s(+1) | 8 |
| | | | | | | | | a | a | 9 |
| | | | | | | | | a | s(+1) | 42 |
| | | | | | | | | s(-1) | a | 32 |
| | | | | | | | | s(-1) | s(+1) | 16 |
| B | 30 | 1.3775 | 369.64 | 27,053.35 | 447 | 22,371.36 | a | a | 11 | |
| | | | | | | | a | s(+1) | 30 | |
| | | | | | | | s(-1) | a | 17 | |
| | | | | | | | s(-1) | s(+1) | 33 | |
| | | | | | | | a | a | 30 | |
| | | | | | | | a | s(+1) | 12 | |
| B | 32 | 1.3945 | 368.93 | 27,105.41 | | | s(-1) | a | 17 | |
| | | | | | | | s(-1) | s(+1) | 33 | |
| | | | | | | | a | a | 30 | |

Appendix 7. 8: Computed photo-physical properties of *Meso*-tetra(5-bromothiophen-2-yl)porphyrinato Nickel (II)

| Molecule | Band | State | f, oscillator strength | Calculated | | Empirical | | Wavefunction | | Probability (%) |
|----------|------|--------|------------------------------|------------|------------------|-----------|------------------|--------------|----------|-----------------|
| | | | | nm | cm ⁻¹ | nm | cm ⁻¹ | HOMO(□) | -LUMO(□) | |
| Ni-BTP | Q | 4 | 0.0005 | 526.37 | 18,998.04 | 539 | 18,552.88 | a(-1) | a | 8 |
| | | | | | | | | a(-1) | s(+1) | 36 |
| | | | | | | | | s | a | 45 |
| | | | | | | | | s | s(+1) | 10 |
| | | | | | | | | a(-1) | a | 36 |
| | | | | | | | | a(-1) | s(+1) | 8 |
| | B | 8 | 1.4171 | 365.99 | 27,323.15 | 428 | 23,364.49 | s | a | 10 |
| | | | | | | | | s | s(+1) | 45 |
| | | | | | | | | a(-1) | a | 41 |
| | | | | | | | | a(-1) | s(+1) | 12 |
| | | | | | | | | s | a | 10 |
| | | | | | | | | s | s(+1) | 34 |
| B | 9 | 1.2266 | 365.25 | 27,378.51 | 428 | 23,364.49 | a(-1) | a | 11 | |
| | | | | | | | a(-1) | s(+1) | 37 | |
| | | | | | | | s | a | 30 | |
| | | | | | | | s | s(+1) | 10 | |

Appendix 8: Antimicrobial Activity

Appendix 8. 1: Methicillin Resistant *Staphylococcus aureus* survival rate

| Bacteria | MRSA Survival Rate (%) | | | | | | | | | |
|---|-------------------------------|-----------|-----------|-----------|------------|--------------|-----------|-----------|-----------|------------|
| Condition | Dark | | | | | Light | | | | |
| Concentration, μM | 20 | 40 | 60 | 80 | 100 | 20 | 40 | 60 | 80 | 100 |
| BTP | 89 | 87 | 83 | 95 | 82 | 81 | 72 | 63 | 46 | 38 |
| Zn-BTP | 99 | 82 | 88 | 72 | 75 | 69 | 46 | 53 | 41 | 40 |
| In-BTP | 93 | 95 | 86 | 91 | 91 | 66 | 58 | 56 | 47 | 24 |
| Fe-BTP | 95 | 97 | 91 | 85 | 81 | 70 | 45 | 50 | 46 | 30 |

Appendix 8. 2: Carbapenem Resistant *Escherichia coli* survival rate

| Bacteria | CRE.coli Survival Rate (%) | | | | | | | | | |
|---|-----------------------------------|-----------|-----------|-----------|------------|--------------|-----------|-----------|-----------|------------|
| Condition | Dark | | | | | Light | | | | |
| Concentration, μM | 20 | 40 | 60 | 80 | 100 | 20 | 40 | 60 | 80 | 100 |
| BTP | 92 | 94 | 96 | 95 | 93 | 82 | 79 | 74 | 69 | 55 |
| Zn-BTP | 88 | 93 | 93 | 91 | 98 | 76 | 73 | 71 | 66 | 57 |
| In-BTP | 96 | 96 | 91 | 88 | 87 | 73 | 66 | 53 | 51 | 49 |
| Fe-BTP | 89 | 88 | 84 | 85 | 86 | 74 | 60 | 55 | 52 | 46 |